A Controllable Synthesis and Catalytic Behavior Study of Micro- and Mesoporous Zeolites Made by Rotational Intergrowths

A Dissertation
SUBMITTED TO THE FACULTY OF
UNIVERSITY OF MINNESOTA
BY

Dandan Xu

IN PARTIAL FULFILLMENT OF THE REQUIREMENTS
FOR THE DEGREE OF
DOCTOR OF PHILOSOPHY

Prof. Michael Tsapatsis, Adviser

July 2018

Acknowledgements

I would like to express my sincere gratitude to my adviser, Professor Michael Tsapatsis, for guiding me through my research, providing both valuable technical advice and showing me exemplary scientific rigor.

I would also like to thank Professors Andreas Stein, Alon McCormick, Paul Dauenhauer, Andre Mkhoyan, and Robert Tranquillo for serving on my Ph.D. defense committee and for providing insightful comments during my preliminary and final exams.

My thanks also go to the current and former members of the Tsapatsis group and all my collaborators for their generous support during my Ph.D. research. Specifically, I would like to acknowledge Dr. Xueyi Zhang and Dr. Dongxia Liu who gave me hands-on help at the beginning of my research as well as great inspirations; Drs. Elizabeth E. Mallon, Kumar Varoon Agrawal, and Ana In´es Torres who kindly and patiently taught me on various instrumentation and modeling software; Dr. Garrett Swindlehurst, Dr. Limin Ren, Dr. Qiang Guo, Dr. Omar Abdelrahman, Prashant Kumar, Matheus Dorneles De Mello and Anatoliy Kuznetsov who worked closely with me on the synthesis and characterization of SPP zeolites; Sang Hyun Ahn and Professor Suk Bong Hong for their generous help with the FTIR measurement; Drs. Nitish Mittal and Joseph DeWilde who helped me with mathematical modeling; Dr. Maryam Khaleel, Dr. Sabrina Conrad, Meera Shete, and Feng Xue for the frequent discussions and support; and Professor Wei

Zhang and other staff members in the characterization facility for their professional support on material characterizations.

I am greatly indebted to my family and friends in China, who provided generous support to many aspects of my life despite my absence during the past years. Lastly, I especially would like to thank my husband, Peng Bai, and our loving daughter, Victoria, born during my Ph.D. training, who have accompanied me throughout this journey.

Abstract

Zeolites are considered as one of the key heterogeneous catalysts in refinery operations and petrochemistry processes. Researchers have been actively exploring new designs or concepts to foster the applications of zeolites in other fields. To improve the accessibility of active sites and reduce the diffusion limitations within micropores, various hierarchically organized pore systems have been architected based on the conventional microporous zeolites. Advances in zeolite synthesis and hierarchical structure design could bring about opportunities for new catalytic applications as well as improvements of current technological processes. However, the multilevel pore architectures complicate the understanding of their catalytic behaviors. Therefore, this dissertation has addressed the attempts on understanding the structure—activity relationship in hierarchical zeolites for maximal catalytic advantages and future rational catalyst design.

Self-pillared pentasil (SPP) zeolite was selected as a prototype of hierarchical zeolites, and its formation mechanism was studied at the beginning of this dissertation. Different strategies were then developed to tailor the SPP zeolite structure and mesoporosity. Catalytic behavior of SPP zeolites was explored through studies of model reactions (i.e., benzyl alcohol self-etherification and alkylation with mesitylene). Key structural attributes to selectivity and catalytic efficiency were determined through kinetic studies. A quantitative analysis towards the catalytic contributions and diffusion resistance could assist the practical applications of SPP zeolites and other similar hierarchical zeolites in the future.

Table of Contents

List of Tables

List of Figures

List of Abbreviations

Al-SPP	Aluminosilicate self-pillared pentasil
DME	Dimethyl ether
dTBP	2,6-di-*tert*-butylpyridine
ICP-OES	Inductively coupled plasma optical emission spectroscopy
IFT	Indirect Fourier transform
MDA	4,4'-methylenedianiline
PDDF	Pair distance distribution functions
RGC	Reactive gas chromatography
SDA	Structure directing agent
SPP	Self-pillared pentasil
SAXS	Small-angle x-ray scattering
TBPOH	Tetrabutyl phosphonium hydroxide
TBAOH	Tetrabutyl ammonium hydroxide
TEAOH	Tetraethyl ammonium hydroxide
TEOS	Tetraethyl orthosilicate
TEM	Transmission electron microscopy
TMAOH	Tetramethyl ammonium hydroxide
TPAOH	Tetrapropyl ammonium hydroxide
MDA	4,4'-methylenedianiline

Chapter 1 Introduction

1.1 Hierarchical zeolites

Zeolites are among the most widely used catalysts in industry. The highly ordered microporous structure with well-defined pore size and properties make them an attractive choice for a variety of reactions and separation processes, such as in oil refining, petrochemistry, fine and speciality chemical productions (Davis, 2002). However, given the restricted size of micropores (ca. 3–12 Å), the catalytic activity becomes significantly hampered when dealing with molecules having kinetic diameters above 10 Å (Corma, 1997). The limited accessibility of active sites in the framework and the diffusion resistance within the microporous domain have motivated the burgeoning interest in synthesizing extra-large pore zeolites (Corma *et al.*, 2006; Sun *et al.*, 2009; Li, Corma and Yu, 2015; Moliner, Martínez and Corma, 2015), nano-sized zeolites (Tosheva and Valtchev, 2005; Valtchev and Tosheva, 2013; Awala *et al.*, 2015; Grand *et al.*, 2017), and micro- and/or mesoporous materials (Corma, 1997; Pérez-Ramírez *et al.*, 2008; Moller and Bein, 2013; Prasomsri *et al.*, 2015; Schwieger *et al.*, 2016).

In consideration of thermal and hydrothermal stability, it is important to preserve the crystalline structure of zeolites when these are used as catalysts. However, most ordered mesoporous materials synthesized do not have crystalline frameworks (Perego and Millini, 2013). Therefore, significant efforts have been put into introducing a secondary porosity into the conventional microporous zeolites, or using microporous zeolites as

building blocks to construct materials with hierarchical pore architecture. The resulting micro- and mesoporous zeolites are commonly referred as “hierarchical zeolites”.

The past decades have seen great advances in the design of hierarchical structures and the discovery of various synthetic routes to achieve them. Different synthetic routes are often classified based on the way mesopores are introduced (Pérez-Ramírez *et al.*, 2008; Chal *et al.*, 2011; Valtchev *et al.*, 2013; Schwieger *et al.*, 2016): 1) post-synthetic modification to create mesoporosity by extracting structural atoms from existing zeolite frameworks is usually known as a “top-down” or “destructive” method; 2) the use of soft or hard templates to control mesopore formation during zeolite crystallization is often known as a “bottom-up” or “constructive” method. Depending on the synthetic route used, hierarchical zeolites may have ordered or random, connected or isolated mesoporosity, as well as different acidities. The desired morphology and catalytic property should be carefully chosen based on the needs of target reactions.

Unlike that in a conventional microporous zeolite, the diffusion lengths of microporous domains in a hierarchical zeolite can be reduced down to a single-unit-cell (i.e., nanometer scale). One specific case of single-unit-cell hierarchical zeolites to be discussed in this dissertation is called “Self-Pillared Pentasil (SPP)” zeolites (X. Zhang *et al.*, 2012). Synthesized through one direct step using a tetrabutyl phosphonium structure directing agent, SPP forms a “house-of-cards” structure based on MFI/MEL intergrowths. No secondary growth or complex organic template molecules are needed during the synthesis, making it more economically attractive compared to other templating methods.

While intergrowth is a phenomenon commonly occurring in zeolitic materials, it is unclear how mesopores are generated or organized during the hydrothermal process of SPP synthesis. The ability to manipulate the intergrowth can be both interesting and useful as it can introduce a great level of structural flexibility and offer the potential of tailoring the structure based on catalytic needs.

1.2 Catalysis applications

The introduction of meso- or macro-porosity in conventional microporous zeolites has broadened their potential applications as catalysts, especially for reactions involving bulky molecules. Improved activity, selectivity or lifetime were frequently reported in different test reactions, from the synthesis of fuels and chemicals to biomass valorization and pollution abatement (Parlett, Wilson and Lee, 2013; Jacobs, Dusselier and Sels, 2014; Hartmann, Machoke and Schwieger, 2016).

Depending on how bulky molecules are involved, potential catalytic applications can be divided into two types: (1) reactions with bulky desired products, such as biomass conversion, alkylation of aromatics, production of 4,4'-methylenedianiline (MDA) and ε-caprolactam, *etc*.; and (2) reactions with bulky side products, such as catalytic cracking, production of aromatics, methanol-to-hydrocarbon (MTH) process, *etc*. When the desired products have relatively large sizes, the improved selectivity and activity is often attributed the reduced diffusion limitation and a larger external surface (Sun and Prins, 2008; Li, Prins and van Bokhoven, 2009; Chu, Wang, *et al.*, 2010; Chu, Yang, *et al.*, 2010; Kim, Park and Ryoo, 2011; Leng *et al.*, 2013; Keller *et al.*, 2015; Ren *et al.*, 2015;

Wang *et al.*, 2015; Yin *et al.*, 2015). When the side products are bulky or coke is concerned, the increasing lifetime in hierarchical zeolites is often attributed to the slower coke formation predominantly on the external surface, as a result of the open and interconnected mesopores (MEI *et al.*, 2008; Choi *et al.*, 2009; Kim, Choi and Ryoo, 2010; Hu *et al.*, 2012; Koekkoek *et al.*, 2013; Milina *et al.*, 2014; Ngoye *et al.*, 2014; Wang *et al.*, 2014; Zhang *et al.*, 2015), while improved activity and selectivity, if observed, are often ascribed to the improved mass transport (Christensen *et al.*, 2003). Emerging (potential) commercialization of hierarchical zeolites includes areas from traditional oil refining to new energy (such as natural gas, biomass, *etc.*) and environmental applications (Martínez and Corma, 2011; Pérez-Ramírez *et al.*, 2011; Li, Valla and Garcia-Martinez, 2014a; Perego *et al.*, 2017).

Despite the promise for advanced catalysis applications, relatively few efforts have been directed to a systematic investigation of the underlying reasons for the observed performance (Christensen *et al.*, 2003; Liu *et al.*, 2011; X. Zhang *et al.*, 2012; Konno *et al.*, 2014; Gamliel *et al.*, 2018). The connectivity of mesopores, which leads to a significantly increased area of accessible mesopore surface, and the reduced size of micropore domains, which reduces the characteristic diffusion path lengths, are considered two key factors for catalytic applications that distinguish them from conventional microporous zeolites. A more detailed understanding and quantification of the structure—activity relationship is pivotal for the rational design of hierarchical structures.

1.3 Scope and organization

This dissertation is divided into six chapters, focusing on two directions: 1) SPP structure formation and control (Chapter 2, 3 and 4) and 2) understanding the structure—activity relationship using SPP as model catalysts (Chapter 5).

Unraveling the growth mechanism responsible for SPP formation is pivotal to enable the precise control of pore structures. In Chapter 2, a complete phase evolution during SPP hydrothermal process was given with a proposed growth mechanism to explain the formation of the “house-of-cards” structure. The understanding from this study serves as the foundation for the following Chapter 3, 4 and directs us to the further morphology control of SPP structure.

Chapter 3 and Chapter 4 describe our efforts in manipulating the SPP structure by controlling MFI/MEL intergrowth. In Chapter 3, different synthetic conditions and compositions in SPP synthesis were explored, and two strategies to change the layer thickness (i.e., the diffusion length of microporous domain) were developed without altering the pore size distribution. The tunable mesoporosity, on the other hand, is achieved in Chapter 4, by controlling the intergrowth frequency using a freeze-drying technique. The underlying reason for the change of intergrowth frequency was also discussed. All strategies on structure control were successfully extended to aluminosilicate SPP synthesis, where aluminum is incorporated in the SPP framework and ion-exchanged to obtain Brønsted acidity. The incorporation efficiency and acidity of Al-SPP synthesized is discussed by the end of Chapter 3 and 4, respectively.

With the Al-SPP synthesized and Brønsted acid site densities determined, Chapter 5 further studies the structure—activity relationship based on SPP zeolites. Frequently reported potential applications of hierarchical zeolites are often related to the reactions that include bulky molecules. In Chapter 5, two parallel liquid-phase reactions, alkylation and self-etherification of benzyl alcohols, were selected as the model reactions. Kinetic models were developed based on the experimental data, including a mass transport analysis. These models allowed us to quantitatively assess the catalytic contributions from mesopore surface and micropores of SPP zeolite in the model reactions, and also to correlate the selectivity with the characteristic length of microporous domains (i.e., half of the layer thickness in SPP zeolites).

When a desired product is produced from a bulky reactant, the reaction may only access to the external surface active sites. To such a kind of surface reaction, the surface topology effect is also discussed. Two 10MR zeolites, SPP and MCM-22, with different surface topology were selected as model catalysts. Their catalytic performances were compared under the same conditions and the significantly different catalytic performances were found and explained based on the corresponding kinetic analysis.

Finally, based on the main conclusions and understandings from Chapter 2 to 5, Chapter 6 proposes some promising directions for future study regarding the practical applications of SPP zeolites, in the hope of fostering the interests from industry.

Chapter 2 Growth mechanism of single-unit-cell hierarchical zeolites made by rotational intergrowths[1]

2.1 Introduction

Hierarchical zeolites are materials with ordered micropores, typical of zeolites (0.5–2 nm), and mesopores that are up to an order of magnitude larger in size (2–50 nm) (Pérez-Ramírez *et al.*, 2008). They can be viewed as a network of zeolitic domains separated by mesopores. This special morphology can give hierarchical zeolites advantages for certain applications in adsorption and catalysis, because the diffusion length in the zeolitic domains becomes smaller and thus diffusion limitations can be eliminated or reduced (Pérez-Ramírez *et al.*, 2008; Liu *et al.*, 2011). Moreover, the domains in hierarchical zeolites (such as lamellar and spherical domains) can be isolated and used for other applications including seed layers for thin zeolite membranes for separations (Corma, Fornes, *et al.*, 1998; Wang *et al.*, 2005; Choi *et al.*, 2009; Lee *et al.*, 2011; Roth and Dorset, 2011). One challenge is to prepare hierarchical zeolites with at least one dimension of the domains as small as the size of a zeolite unit cell (e.g., 1 to 5 nm) to eliminate any micropore diffusion resistance and maximize the fraction of external surface area over micropore surface area. At the single-unit-cell limit, the microporous framework is still preserved and, as a result, three-dimensional confinement of

[1] Results presented in this chapter are published in:

Xu *et al. Adv. Funct. Mater.* **24,** 201 (2014)

adsorbates, reactants and products is still possible as in typical zeolites. However, external surface adsorption is prevalent for bulky molecules that do not fit in the micropores, while configurations with partial confinement, where one part of the molecule resides in the microporous interior and another part resides on the external surface, may be encountered and even dominate catalytic activity and adsorption selectivity.

The preparation of hierarchical zeolites is usually done with two approaches: (1) by the "addition" of framework material, with methods such as crystallization with or without mesopore templates and pillaring (Wang *et al.*, 2007; Na *et al.*, 2011; Serrano *et al.*, 2011; Inayat *et al.*, 2012; X. Zhang *et al.*, 2012; Chaikittisilp *et al.*, 2013), and (2) by the "subtraction" of framework material from a zeolite crystal, with methods such as desilication and dealumination (Ogura *et al.*, 2001; Pérez-Ramírez *et al.*, 2008). However, the preparation of these materials usually requires multiple synthesis steps, and, in many cases, it is challenging to form hierarchical zeolites with ultra‐small features of size close to one unit cell. A new strategy of making hierarchical zeolites with single-unit-cell microporous domains, known as "Self-Pillared Pentasil (SPP)" zeolites, was discovered recently (X. Zhang *et al.*, 2012). In an environment that encourages the epitaxial intergrowth of two structures with different levels of symmetry, the higher-symmetry structure (MEL) acts as a connector to connect the lower-symmetry structures (MFI) to create branching. After this process is repeated, a "house-of-cards" structure is formed where the mesopore dimensions are determined by the frequency of branching.

Although the work described here features the intergrowth of MFI [a zeolite structure that contains sinusoidal 10-member ring (10-MR) channels along the *a*-axis, interconnected with straight 10-MR channels along the *b*-axis] and MEL (a zeolite structure that contains straight 10-MR channels along the *a*-axis, interconnected with straight 10-MR channels along the *b*-axis) to generate a SPP zeolite, the approach could be generalized. Intergrowths between other zeolite structures, such as EMT/FAU (Treacy *et al.*, 1996), ETS-4/ETS-10 (Jeong *et al.*, 2002), CAN/SOD (Okubo *et al.*, 2001), MFI (Karwacki *et al.*, 2009), and CHA (Millward, Ramdas and Thomas, 1985), are common, and could also be used to prepare hierarchical zeolites. Recently, FAU and MFI hierarchical materials have been prepared using this branching approach (Inayat *et al.*, 2012; Chaikittisilp *et al.*, 2013). However, only in the case of MFI as reported in SPP zeolites (X. Zhang *et al.*, 2012), single-unit-cell (2 nm) layers are produced, in all other cases, the layers are much thicker.

In this chapter, we followed the formation process of SPP zeolite by transmission electron microscopy (TEM) and small-angle X-ray scattering (SAXS). Three phases of crystal growth were observed, where amorphous precursor nanoparticles, one-unit-cell MFI nanosheets, and self-pillared particles are formed sequentially. We discuss these findings in the context of previous MFI nucleation and growth models and point to some unique features observed during the SPP growth, which could be critical to the formation of its “house-of-cards” structure.

2.2 Experimental methods

2.2.1 Synthesis of pure silica SPP

The silica sols for SPP synthesis were prepared with the composition 1 SiO_2 : 0.3 SDA : 10 H_2O : 4 EtOH, where SDA (structure-directing agent) was either tetrabutyl-phosphonium hydroxide (TBPOH, 40% by weight, Sigma-Aldrich, TCI America or SACHEM) or tetrabutylammonium hydroxide (TBAOH, 40% by weight, Sigma-Aldrich or SACHEM). The SDA solution was firstly added dropwise into tetraethylorthosilicate (TEOS, 98%, Sigma-Aldrich) with vigorous stirring until the system turns clear. Then distilled water was added into the clear system at room temperature. The clear sol was sealed with Teflon tape and aged at 80 °C in a Teflon bottle with continuous stirring. After 48 h aging, the clear sol was quickly transferred to a Teflon-lined stainless steel autoclave, sealed and heated for 3 - 40 h in a pre-heated oven at 120 °C. The final sols after heating were then collected for further characterizations.

2.2.2 Characterizations

SAXSess (Anton-Parr) was used to obtain small angle X-ray scattering patterns from the sols after hydrothermal treatment. The sols were placed into a vacuum-tight 1 mm quartz capillary. All measurements were carried out at room temperature (25 °C). The scattering vector q was calculated from the scattering angle 2θ through $q = 4\pi\lambda^{-1}\sin\theta$. Scattering from an equivalent water-ethanol mixture was used as a background pattern and subtracted from all sample scattering patterns. Patterns were then de-smeared from the beam profile and fitted using the GIFT program (Bergmann, Fritz and Glatter, 2000). Pair

distance distribution functions (PDDF) were obtained by indirect Fourier transform of the fitted data.

The synthesis sols obtained at different times were diluted 10 times (1:10 by volume) with distilled water, and used for TEM samples. TEM specimens were prepared by placing droplets of the diluted sol onto the copper grid coated with ultra-thin carbon film and holey carbon film (Ted Pella Inc.). The non-diluted TEM specimen was prepared by drawing a thin line onto the same type of grid from the clear sols without any dilution, and then spreading over the copper grid. All images included here, except Figure 2-3 (b), are from diluted sols. Comparative experiments, not shown here, using diluted and non-diluted samples indicate that the morphology of the MFI particles is not altered by the dilution. The specimens were dried at room temperature. TEM imaging was performed on an FEI Tecnai G^2 F30 TEM operating at 300 kV. All TEM images were captured using a CCD camera.

Argon (87.3 K) adsorption was performed using a commercially available automatic manometric sorption analyzer (Quantachrome Instruments Autosorb iQ MP). Prior to adsorption measurements, the samples were outgassed at 300 °C for 16 h under turbomolecular pump vacuum. Full micro- and mesopore size distributions were calculated from the argon isotherms using the argon on zeolites/silica cylindrical pore adsorption branch method (Ravikovitch and Neimark, 2001).

2.3 Results and discussion

2.3.1 SPP synthesis based on tetrabutyl structure-directing agents (SDAs).

In our earlier report on SPP (X. Zhang *et al.*, 2012), the focus was on the use of tetrabutylphosphonium hydroxide (TBPOH) as SDA, however, as mentioned in the supporting information of that report, tetrabutylammonium hydroxide (TBAOH) can also be used to obtain similar orthogonally intergrown 2 nm MFI lamellae. This fact is further elaborated here. Figure 2-1 shows self-pillared MFI prepared using TBPOH and TBAOH from various sources. It appears that the synthesis is robust and insensitive to the source of SDA. As seen in Figure 2-2, the argon adsorption/desorption isotherms of SPP made with these two SDAs show both the micropores of MFI and the characteristic mesopores ranging from 2–7 nm. The adsorption isotherms are identical up to $p/p_0 = 0.6$, indicating that the two materials have the same textural properties in the micropore and mesopore regions. Thus, TBPOH and TBAOH can be used interchangeably for the synthesis to yield the characteristic hierarchical porosity of SPP.

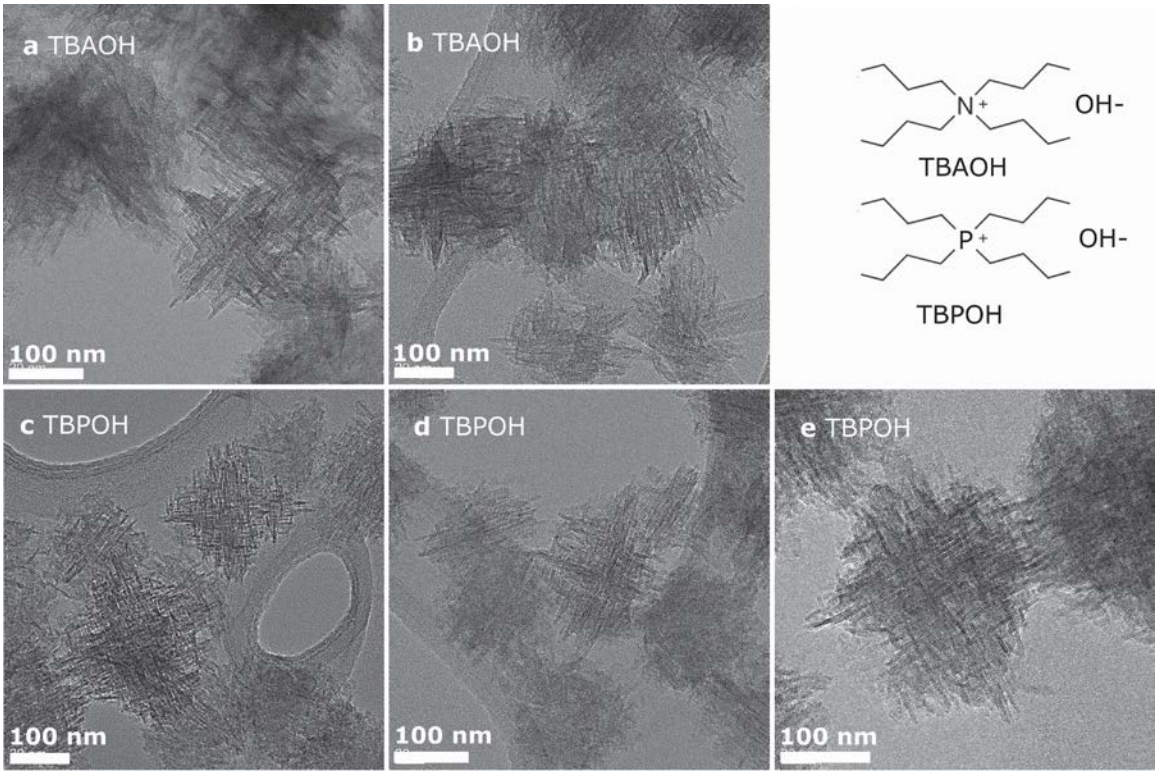

Figure 2-1 SPP synthesized based on tetrabutyl SDAs from different sources. The SDAs are a) TBAOH from SACHEM, b) TBAOH from Sigma-Aldrich, c) TBPOH from SACHEM, d) TBPOH from Sigma-Aldrich, and e) TBPOH from TCI America.

2.3.2 Phase evolution during SPP formation

In order to understand the sequence of events leading to the formation of the SPP zeolite, one composition (1 SiO_2 : 0.3 TBPOH : 10 H_2O : 4 EtOH) was followed over time. A clear sol was obtained after the hydrolysis of tetraethylorthosilicate (TEOS), indicating the absence of large aggregates. A clear synthesis mixture gives the possibility of studying the system evolution with small-angle X-ray scattering (SAXS), which could identify the size and shape of ultra-small particles, especially when the particles are uniform (Davis *et al.*, 2006). This clear system was heated first at 80 °C for 48 h, then at

120 °C for up to 40 h. During the hydrothermal synthesis at 120 °C, samples from the synthesis mixtures were collected and analyzed by SAXS and TEM.

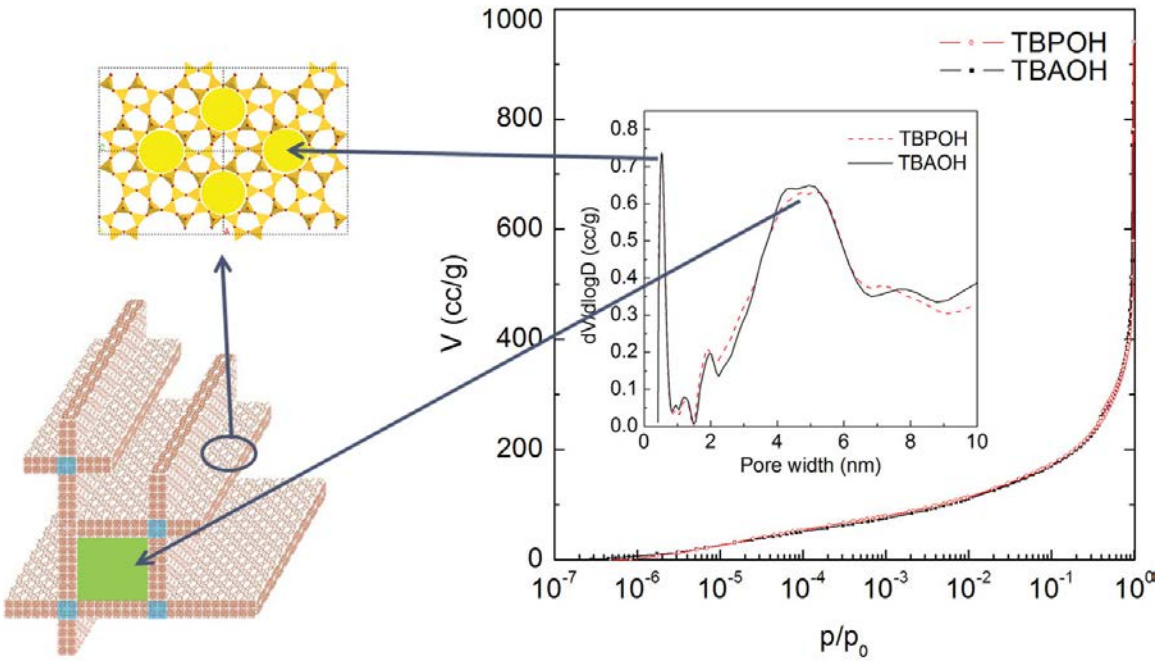

Figure 2-2 The hierarchical porosity of SPP zeolites as determined from argon adsorption. The pore size distribution (inset, fitted from non-local density functional theory (NLDFT) method) shows that SPP has the typical micropores of MFI (0.52 nm) and characteristic mesopores within the 2–7 nm range. Samples made with TBPOH and TBAOH show similar micro- and mesoporosity.

The SAXS and TEM experiments revealed three phases of evolution.

During the first phase, with increasing hydrothermal synthesis time from 0–7 h, the SAXS patterns (Figure 2-4) show the existence of a population of globular nanoparticles, which grows slightly in concentration and/or density. The particle size obtained from an IFT (indirect Fourier transform) analysis of the SAXS patterns is 4 nm (Figure 2-4 (b)). No evidence for crystallinity is observed by TEM for samples collected up to 7 h. The existence of amorphous precursor nanoparticles is expected based on earlier studies of

MFI precursor sols: for example, the synthesis of TPA-silicalite-1 in a TPAOH (tetrapropylammonium hydroxide)-TEOS-water system involved the formation of small precursor nanoparticles (Davis *et al.*, 2006; Kumar *et al.*, 2008). These particles are formed spontaneously upon TEOS hydrolysis and remain nearly constant in size during the initial phases of hydrothermal growth.

After 8.5 h, the growth entered the second phase, where the low-*q* intensity increase indicated the appearance of particles with a larger characteristic dimension. (Figure 2-4) IFT analysis from these patterns showed that in addition to the 4 nm nanoparticles, another length scale (10–50 nm) emerged. Interestingly, the intensity increase in the low-*q* region is not accompanied by intensity loss in the higher-*q* region. Parallel HRTEM studies confirmed the emergence of a new population of crystalline particles. Consistent with SAXS, the lateral size of these crystalline particles ranged from 10–50 nm. They were found to be highly crystalline MFI. (Figure 2-4 (c), (d)) The low contrast as well as the uniform orientation of the particles suggested that these particles are nanosheets, thin along the *b*-direction and wide along the *a*- and *c*-directions. Previously reported AFM images confirmed that the thickness of these particles is around 2 nm (X. Zhang *et al.*, 2012). In the formation of TPA-silicalite-1, a closely related system, Davis et al. and Kumar et al. found that amorphous precursor nanoparticles increased in size, then aggregated to form 100 nm-sized aggregates, which, subsequently, transformed to MFI (Davis *et al.*, 2006; Kumar *et al.*, 2008). Examples of intermediate amorphous aggregates also exist in the formation of other zeolites, where at a certain stage amorphous particles

transform to crystals by parts (Mintova *et al.*, 1999). Unlike these previous observations in zeolite systems, where zeolite crystals nucleate within amorphous aggregates, the formation of SPP either does not involve amorphous-to-crystal evolution (i.e., crystals directly form from the clear synthesis sols), or this transformation is much faster than the formation rate of the amorphous aggregates.

To our knowledge, the coexistence of precursor nanoparticles and MFI nanosheets is a unique characteristic of the SPP system. The absence of any amorphous aggregates (detectable by TEM) at this MFI nucleation phase is also a unique feature of this system among reported MFI syntheses.

During the second phase and as early as 8.5 h, crystalline nanoparticles clearly started to exhibit lamellar breakouts on the MFI nanosheets (Figure 2-3). This is the point where the rotational intergrowth starts. TBAOH and TBPOH are structure directing agents that are known to direct the intergrowth of MFI and MEL (Olson and Bisio, 1984; Li *et al.*, 2005), i.e., both MFI and MEL can coexist in one crystal with fully connected SiO_4 tetrahedra or with the presence of Si-OH defects (Ohsuna *et al.*, 1997). In the synthesis of SPP, it seems that these SDAs create an environment that encourages the intergrowth of MFI and MEL. Thus, MEL can be formed onto the MFI nanosheets, and new MFI layers can emerge out of MEL. If the structures of MFI and MEL are compared, one notices that although they have the same building units (the pentasil unit), they differ in symmetry. On MFI nanosheets, MEL can only be incorporated along its *a*-direction, which could lead to branching in 2 opposite directions; however, on MEL, MFI can be formed along

both (equivalent) *a*- and *b*- directions, which could lead to branching in 4 directions. When MEL is formed, it can act as connector to connect new features that lead to branching (one-unit-cell nanosheets, in this case). If these newly formed features also contain MEL, another generation of branching could happen. The above-mentioned intergrowth of MFI and MEL is discussed in more detail in our previous report, where the possible structures are enumerated (X. Zhang *et al.*, 2012). This repetitive rotational intergrowth led to anisotropic particle shapes, and also wider particle size distributions.

In the third phase, as seen in the SAXS patterns at low-*q* range, much larger particles were observed: the crystalline particles after 19 h hydrothermal synthesis (Figure 2-4 (e)) are much larger comparing to the particles after 10 h synthesis (Figure 2-4 (d)). Finally, with complete hydrothermal synthesis after 40 h, the crystals are fully developed with the typical self-pillared morphology (Figure 2-1) and their long dimensions are beyond the low angle resolution limit of SAXS.

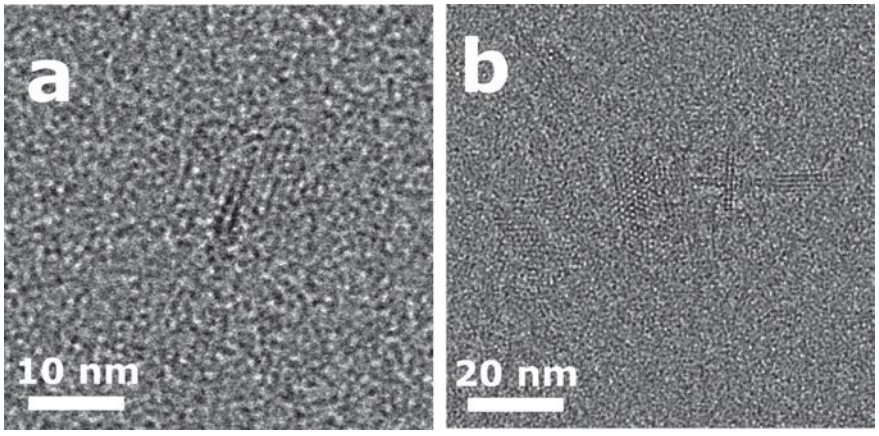

Figure 2-3 High-resolution transmission electron microscopy (HRTEM) images showing rotational intergrowths observed after 8.5 (a) and 10 (b) h hydrothermal synthesis.

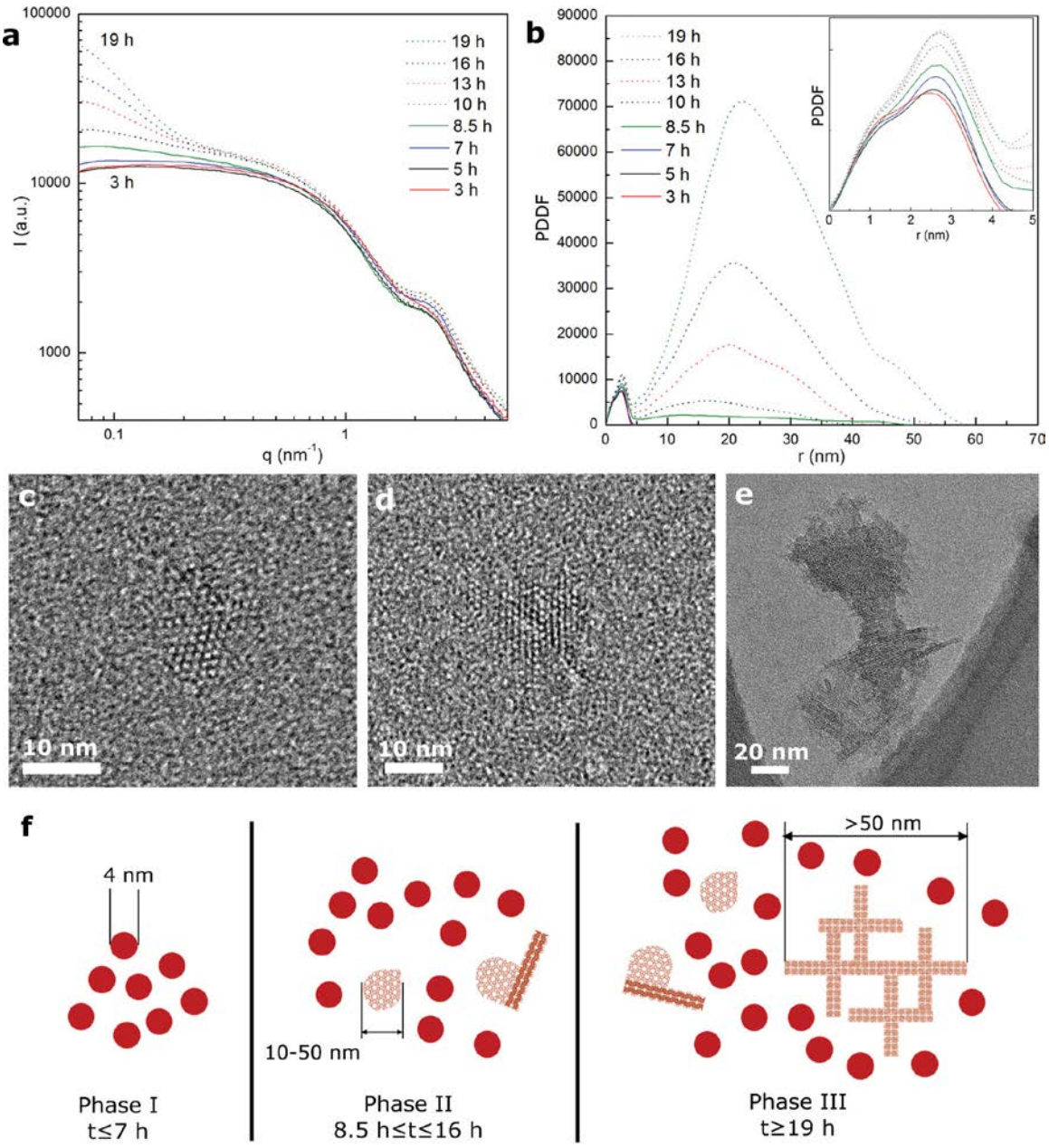

Figure 2-4 Small-angle X-ray scattering (SAXS) data (a) and corresponding pair distance distribution functions (PDDF) (b) from sols (with composition 1 SiO_2 : 0.3 SDA : 10 H_2O : 4 EtOH) heated at 80 °C for 48 h and then at 120 °C for 3, 5, 7, 8.5, 10, 13, 16, and 19 h. Representative TEM images from the solids contained in the sols after c) 8.5 h, d) 10 h, and e) 19 h at 120 °C. A schematic of the three phases identified is shown in (f).

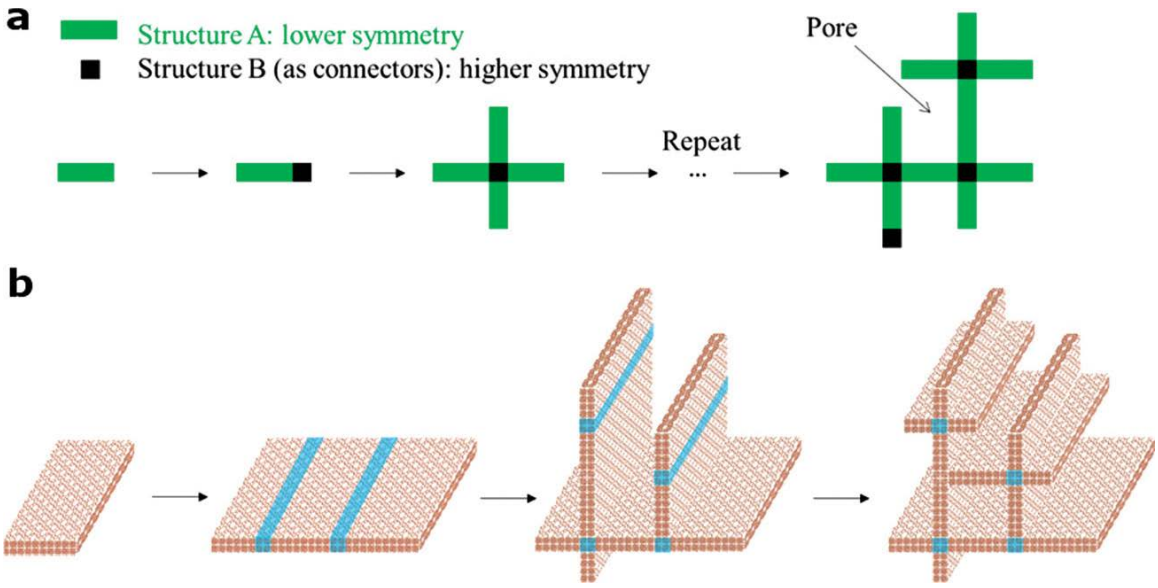

Figure 2-5 Proposed growth mechanism of SPP zeolites. a) When two structures with two different levels of symmetry can intergrow, the higher-symmetry structure may serve as a connector to connect the lower-symmetry structure. If this process is repeated, hierarchical materials can be formed. b) A hierarchical zeolite, SPP, formed by the intergrowth of MEL and MFI is shown. Here, MFI (red) has the lower symmetry (*Pnma*) and MEL (blue) has the higher symmetry ($I\bar{4}m2$)

The presence of MFI nanosheets at early phases of growth taken together with the presence of orthogonally arranged lamellae in SPP particles after 40 h heating suggested that these nanosheets are responsible for the formation of the lamellae, since they have the same thickness and crystallographic orientation. Two possible mechanisms exist for the formation of the intergrown crystals: oriented aggregation, and direct growth of nanosheets by addition of silicate species. Oriented aggregation is a non-classical crystal growth mechanism, according to which crystalline particles aggregate in a crystallographically aligned manner (Davis *et al.*, 2006; Liang *et al.*, 2007; Kumar *et al.*, 2008; Revealed *et al.*, 2010). If oriented aggregation of the nanosheets was the formation mechanisms of SPP, one would expect that the SPP particles would have a more open

structure. Instead of the 2–7 nm mesopores, the mesopore dimensions would have been similar to the dimension of the nanosheets, i.e., 10–50 nm. Therefore, direct growth by addition of molecular silicate species or by aggregation with precursor nanoparticles seems to be more likely mechanisms for the formation of SPP. Based on the observation above, the scheme of SPP growth mechanism is further summarized below, as shown in Figure 2-5.

2.4 Conclusions

In this chapter, tetrabutyl SDAs from different sources have been successfully applied in SPP zeolite synthesis, showing the same pillared structures and pore size distributions.

The growth process of SPP was followed over time using TEM and SAXS to reveal three phases of crystal growth. The repetitive branching mechanism based on the rotational intergrowth of MFI and MEL structures is confirmed through the TEM observations.

The formation of MFI nanosheets did not go through the aggregation of amorphous precursors, and the single-unit-cell thickness of MFI lamella have been directly formed from clear solution and well preserved during the crystallization under reported hydrothermal reaction condition. The initial branching was observed during the SPP phase evolution and the repetitive branching based on the frequent fault growths of MEL structure was then considered to lead to the formation of the “house-of-cards” structure.

Chapter 3 Synthesis of self-pillared pentasil zeolites with various layer thicknesses

3.1 Introduction

In conventional microporous zeolites, the utilization of active sites is often found to be inefficient as the so-called “dead zone”—defined as a region where the active sites are inaccessible to the reactants—exists in the center of the catalyst particle (Pérez-Ramírez *et al.*, 2008; York *et al.*, 2011; Schwieger *et al.*, 2016). The catalytic contribution from external acid sites is often neglected due to the low surface to volume ratio. Such a low utilization degree of zeolite crystals is mainly attributed to the limited transportation inside the micropores. Additionally, the slow mass transport in microporous zeolites may also lead to an accumulation of coke or coke precursors, causing the catalyst deactivation or a reduced catalyst lifetime.

To improve the mass transport in the conventional microporous zeolites, efforts can be made on (1) increasing the molecular diffusivity inside the micropores, such as synthesizing extra-large pore zeolites (Corma *et al.*, 2006; Sun *et al.*, 2009; Li, Corma and Yu, 2015; Moliner, Martínez and Corma, 2015); and (2) reducing the diffusion path lengths, such as synthesizing nano-sized zeolites (Tosheva and Valtchev, 2005; Valtchev and Tosheva, 2013; Awala *et al.*, 2015; Grand *et al.*, 2017) or introducing hierarchical porosity into the microporous zeolites (i.e., hierarchical zeolites) (Corma, 1997; Pérez-Ramírez *et al.*, 2008; Moller and Bein, 2013; Prasomsri *et al.*, 2015; Schwieger *et al.*, 2016). For bulky microporous zeolites with irregular shapes, the diffusion path length (or

so-called correlation length) can be defined as the ratio of particle volume over the external surface area (Hartmann, Machoke and Schwieger, 2016). While for the hierarchical zeolites with layer structures, the diffusion path length for microporous domains can be approximated as one half of the layer thickness.

In the case of SPP zeolites, the layer thickness could be reduced to a single-unit-cell with up to 40% external acid sties accessible through its mesopore (X. Zhang *et al.*, 2012). The significantly reduced diffusion path length and improved accessible active sites could be beneficial to the reactions that included bulky reactants or products. Yet when a large side-product or coke is concerned, the effect of the diffusion path length on selectivity becomes unclear, considering the resultant large external surface exposed. The improving lifetime of the hierarchical zeolites with open and interconnected mesoporosity is often accompanied by the increase of coke formation (Choi *et al.*, 2009; Kim, Choi and Ryoo, 2010; Hu *et al.*, 2012; Ramasamy *et al.*, 2014; Sun *et al.*, 2014; Zhang *et al.*, 2015). The ability to manipulate the characteristic lengths of microporous domains is therefore important and could provide opportunities to further study the structure—activity relationship. Additionally, a more flexible structure of the SPP zeolite also allows the future rational design aimed at the selective production of desired chemicals.

In a single-unit-cell SPP structure, the diffusion path length of a microporous domain approximates to one-half of the layer thickness along *b*-axis (i.e., 1 nm). As discussed in Chapter 2, the nanosheets of SPP are directly formed from nanoparticle precursors and

branchings start at the MEL fault growth in phase II. Tetrabutyl SDA plays a critical role in forming the pillared structure by encouraging the MFI/MEL intergrowths. Therefore, the formation of thicker layers in SPP zeolites is likely related to an accelerated or preferential growth of MFI phase along *b*-axis.

To synthesize SPP zeolites with various layer thicknesses, different strategies are explored in this Chapter. The effect of synthetic conditions (such as temperature, hydrothermal reaction time) and chemical sources (such as SDAs, silica/SDA ratios) on the SPP morphology are studied and discussed respectively. Aluminosilicate SPP zeolites are also synthesized with different layer thicknesses, and their acidities are further evaluated and compared accordingly.

3.2 Experimental methods

3.2.1 Synthesis of purer silica SPP at different hydrothermal conditions

7.464 g tetrabutyl phosphonium hydroxide solution (TBPOH, 40% by weight, Sigma-Aldrich) was added dropwise into 7.500 g tetraethyl orthosilicate (TEOS, Sigma-Aldrich) while stirring. A clear solution was obtained, and 3.305 g water was added into the solution. The hydrolysis was carried out at room temperature and kept for 24 h with stirring. A clear sol was obtained with the composition of 10 SiO_2 : 3 TBPOH : 100 H_2O : 40 EtOH. The sol was then transferred to a Teflon-lined stainless steel autoclave. The hydrothermal treatments for SPP were performed in a rotation oven at different temperatures or using different reaction time.

The product was washed with distilled water by repeated centrifugation and decanting of the supernatant, until the pH of the final supernatant was lower than 9. The final precipitate was dried at 343 K for 12 h, followed by calcination at 823 K for 12 h in air.

3.2.2 Synthesis of purer silica SPP with different Si/SDA ratios

The silica sols for SPP synthesis were prepared with different chemical compositions 10 SiO_2 : 4/3/2/1 TBPOH : 100 H_2O : 40 EtOH and 20/15/10 SiO_2 : 3 TBPOH : 100 H_2O : 40 EtOH following the same procedure as described in section 3.2.1. The hydrothermal treatments for SPP with different Si/SDA ratios were all performed in a rotation oven at 388K for 72 h. The separation and calcination procedure are also the same as described above.

3.2.3 Synthesis of purer silica SPP using dual-SDAs

A desired percentage of TBPOH was replace with tetrapropyl ammonium hydroxide (TPAOH, Sigma-Aldrich) or tetraethyl ammonium hydroxide (TEAOH, Sigma-Aldrich) or tetramethyl ammonium hydroxide (TMAOH, Sigma-Aldrich) to obtain a mixed SDA solution. The mixed SDA solution was then added dropwise into 7.500 g TEOS while stirring. A clear solution was obtained and 3.305 g water was added into the solution. The final molar chemical composition is kept at 10 SiO_2 : 3 SDAs : 100 H_2O : 40 EtOH. The rest procedures and hydrothermal conditions are the same as described in section 3.2.2.

3.2.4 Synthesis of Al-SPP at different hydrothermal temperatures

Solution A was prepared by dissolving 0.100 g aluminum isopropoxide (Sigma-Aldrich) in 3.662 g tetra (n-butyl) phosphonium hydroxide solution (TBPOH, 40% by weight,

Sigma-Aldrich). Solution B was prepared by adding 6.500 g TBPOH solution dropwise into 10.211 g tetraethyl orthosilicate (TEOS, Sigma-Aldrich) while stirring. Sodium hydroxide solution was prepared by dissolving 0.162 g sodium hydroxide in 4.485 g water. A clear solution was obtained by adding B to A, followed by the addition of the sodium hydroxide solution. The hydrolysis was carried out for 24 h at room temperature with stirring. A clear sol was obtained with the composition of 10 SiO_2 : 0.05 Al_2O_3 : 3 TBPOH : 0.125 NaOH : 100 H_2O : 40 EtOH. The sol was then transferred to a Teflon-lined stainless steel autoclave.

To prepare SPP with different layer thicknesses, we varied the hydrothermal synthesis temperature and time. The hydrothermal treatments for SPP-2, SPP-4 and SPP-8 were performed in a rotation oven at 388K for 7 days (SPP-2); 393K for 7 days (SPP-4); and at 423K for 2 days (SPP-8), respectively.

The product was washed with distilled water by repeated centrifugation and decanting of the supernatant, until the pH of the final supernatant was lower than 9. The final precipitate was dried at 343 K for 12 h, followed by calcination in air at 823 K for 12 h in a static furnace.

For ion exchange (to allow Na^+ in the framework to be exchanged by NH_4^+), the calcined zeolite was first mixed with distilled water to yield a 5% (by weight) suspension. The suspension was then heated at 343 K for 12 h and washed with distilled water by centrifugation and decanting of the supernatant, so that the pH of the supernatant was 6-7. The precipitate was then mixed with 1.0 mol L^{-1} ammonium nitrate solution to yield a 5%

(by weight) suspension. The suspension was then heated at 353 K for 5 h and the solid was recovered with centrifugation. The treatment in ammonium nitrate solution was repeated three times, and the final product was washed with water, dried at 343 K and calcined in air at 823 K for 4 h in a static furnace.

3.2.5 Characterizations

The morphology of SPP zeolites was determined by transmission electron microscopy (TEM). Typically, a specimen was prepared by applying a few droplets of an aqueous suspension of the washed zeolite product onto an ultra-thin carbon coated 400 mesh copper grid on lacey carbon support film (Ted Pella Inc.). In order to study the morphology of smaller particles obtained at early stages, the final suspension after synthesis was diluted 10 times (volume) with H_2O, and deposited on the same type of grid. All TEM images were obtained under an FEI Tecnai G^2 F30 TEM operating at 300 kV using a CCD camera.

Argon (87.3K) adsorption was performed using a commercially available automatic manometric sorption analyzer (Quantachrome Instruments AutosorbiQ MP). Prior to adsorption measurements, the samples were outgassed at 573 K for 16 h under turbomolecular pump vacuum. The micro- and mesopore size distributions were simulated based on zeolites/silica (cylindrical, pores, NLDFT ads.) model.

Si/Al ratios of all zeolites samples were obtained through inductively coupled plasma optical emission spectroscopy (ICP-OES) analysis carried out by Galbraith Laboratories.

The IR spectra of pyridine and collidine on zeolites employed here were measured on a Nicolet 6700 FT-IR spectrometer using self-supporting zeolite wafers of ca. 13 mg cm^{-2}. Prior to IR measurements, each zeolite wafer was activated under vacuum (10^{-4} Pa) at 450 °C for 2 h inside a home-built IR cell with CaF_2 windows, contacted with containing pyridine and collidine of 1.3×10^3 Pa at 150 and 200 °C for 0.5 h, respectively, and evacuated (10^{-4} Pa) at 150 °C for 0.5 h to remove physisorbed molecules. Then, the IR spectra were recorded at temperatures up to 350 °C. The concentrations of Brønsted and Lewis acid sites in zeolites were determined from the intensities of the IR bands by using integrated area of a given band with the molar extinction coefficient given in the literature (Emeis, 1993; Nesterenko *et al.*, 2006).

Brønsted acid site density was determined by Hoffman elimination of isopropylamine based on a reactive gas chromatography (RGC) technique as reported in (Abdelrahman *et al.*, 2017) or dimethyl ether (DME) titration as reported in (X. Zhang *et al.*, 2012).

3.3 Results and discussion

3.3.1 Hydrothermal temperature and time effect

To understand the temperature effect on MFI/MEL intergrowth, the hydrothermal reaction of SPP zeolites was carried out at different temperatures. The morphologies of SPP zeolites were examined under TEM, as shown in Figure 3-1. The thickness of SPP layers can be measured based on those SPP particles that were imaged along *c*-axis. According to Figure 3-1, the layer thickness of SPP zeolites was found to increase with elevated hydrothermal temperatures, from 2 nm (1 unit cell) at 120 ℃ (Figure 3-1, a) to 3 nm (1.5 unit cell) at 135

℃ (Figure 3-1, b) or 150 ℃ (with a reduced hydrothermal reaction time to 36 h in Figure 3-1, c). A complete destroy of the pillared structure in SPP zeolite was found at 150 ℃ as the hydrothermal reaction time increased to 72 h, and a morphology that was more close to the conventional microporous MFI was observed (Figure 3-1, d). One may speculate that a high temperature during hydrothermal synthesis could facilitate the growth of SPP, especially along *b*-axis, so that the thickening of layers was observed and a further increased hydrothermal reaction time at a high temperature would eventually lead to the formation of a conventional microporous MFI zeolite.

Given that the SPP pillared structure could be destroyed at 150 ℃ after 72 h hydrothermal reaction time, it is unclear that whether the SPP zeolite could maintain its "house-of-cards" structure at a low temperature (T < 135 ℃) over a long hydrothermal reaction time (t > 72 h). Therefore, we further studied the morphology change of SPP zeolites under different hydrothermal reaction times at 115 ℃ using the same chemical composition (10 SiO_2 : 3 TBPOH : 100 H_2O : 40 EtOH) before the hydrothermal step.

As shown in Figure 3-2, a rapid growth in particle size was observed in the first two days during the hydrothermal synthesis of SPP zeolites at 115 ºC. The increase of particle size was not significant from 2.25 days to 8 days, and no morphology change or layer thickening was detected from the TEM images. Therefore, the single-unit-cell pillared structure of SPP zeolite could be well preserved at 115 ºC for up to 8 days.

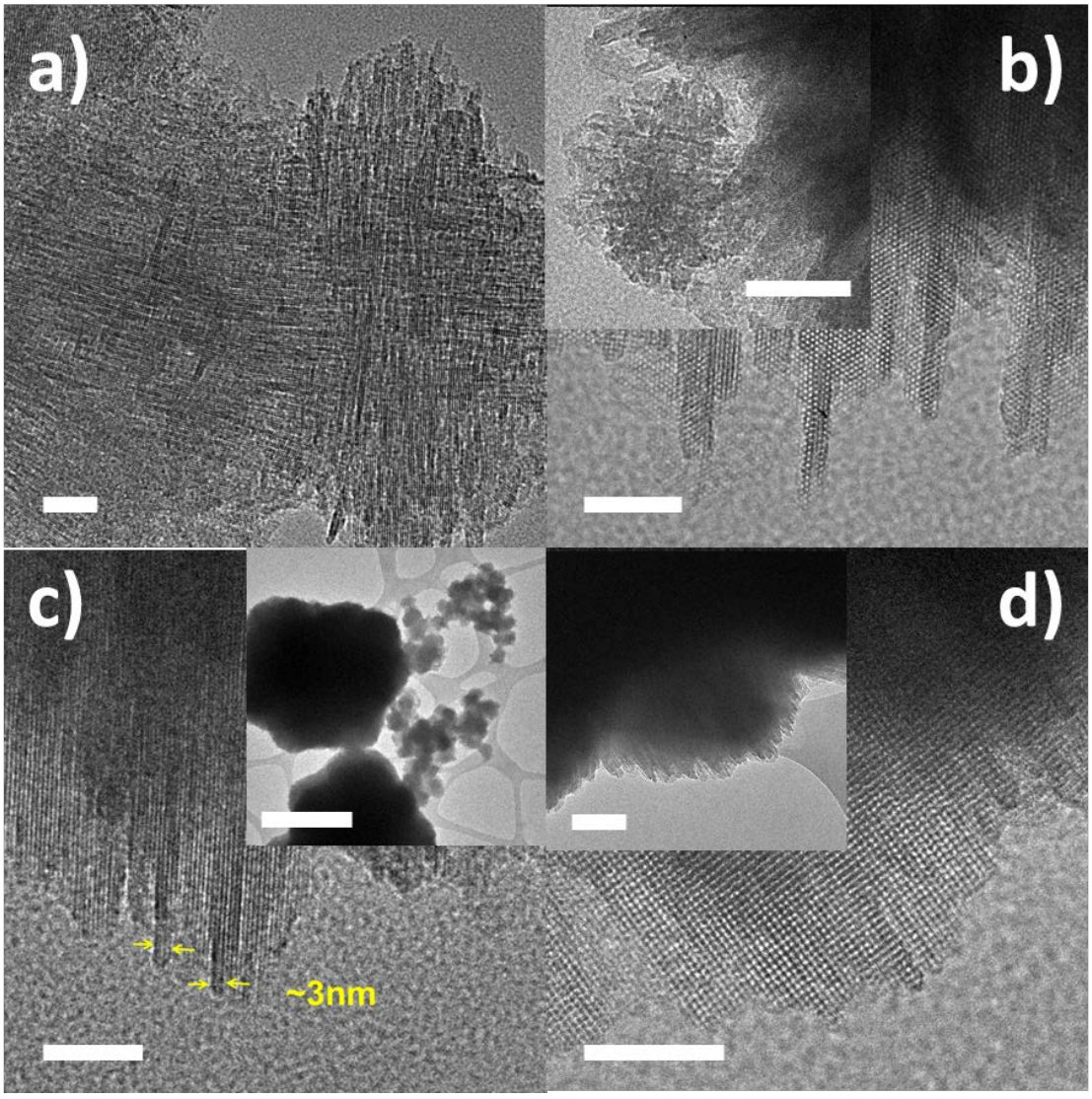

Figure 3-1 TEM images of SPP zeolite particles synthesized at different temperatures and different hydrothermal reaction times. a) 120 ℃ with 72 h; b) 135 ℃ with 72 h; c) 150 ℃ with 36 h; d) 150 ℃ with 72 h. (Scale bar: 20 nm in a–d); 50 nm in the insert of b); 1 μm in the insert of c); and 100 nm in the insert of d).)

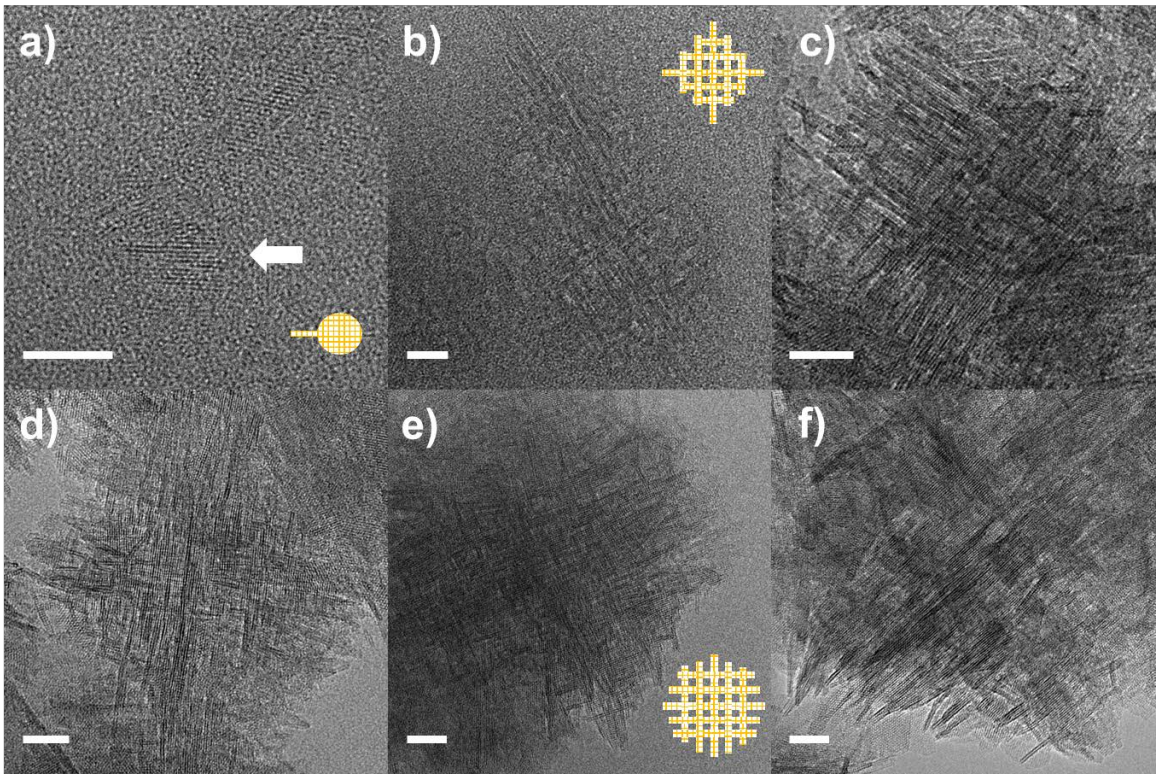

Figure 3-2 The morphology change of SPP zeolites under TEM, synthesized with different hydrothermal reaction times at 115 ºC. a) 1 d; b) 1.5 d; c) 2 d; d) 2.25 d; e) 3 d; f) 8 d. (Scale bar: 20 nm)

The argon adsorption isotherms were also measured and compared among the SPP zeolites synthesized with different hydrothermal reaction times. As shown in Figure 3-3, when the relative pressure is below 0.8, no significant difference was found among all the adsorption isotherms, indicating all SPP samples have the same intra-particle porosity. Similar mesopore size distributions were observed based on the simulation of the adsorption branches from all SPP samples with a slight increase of the mesopore volume for SPP synthesized from 1.5 days to 2 days (see Figure 3-3 right). The increasing adsorption volume at high relative pressure ($0.8 < p/p_0 < 1$) usually represents the inter-particle meso-/macro-pores. In this case, the high adsorption volume at high relative

pressure ($0.8 < p/p_0 < 1$) observed in the SPP zeolite with 1.5 d hydrothermal reaction time could be attributed to the irregular shape of the SPP particle before ripening (as shown in the inserted schemes in Figure 3-3). In a conclusion, the argon adsorption behaviors of SPP zeolites confirm the preservation of SPP mesoporosity from 2 d to 8 d at 115 ℃, which is consistent with the observation under TEM.

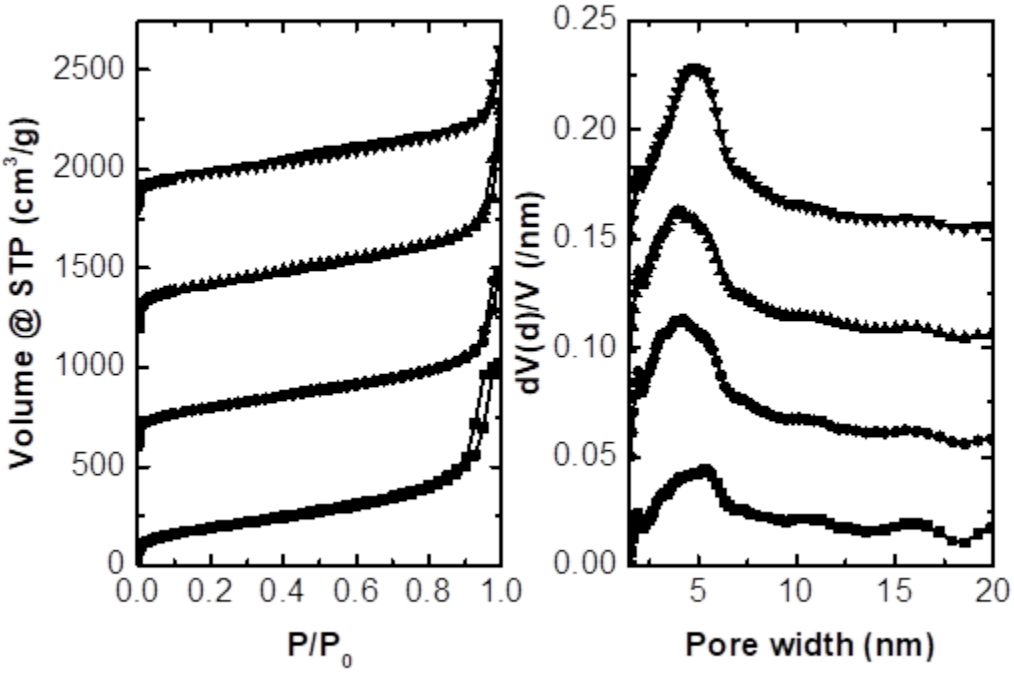

Figure 3-3 (a) Argon (87.3 K) adsorption isotherms of SPP prepared with different hydrothermal reaction times. The isotherms for samples 2, 2.25, 8 d were vertically offset by 600, 1200, 1800 cm^3/g respectively. (b) The corresponding normalized mesopore size distribution (NLDFT/GCMC, cylindrical pore model). The distribution of mesoporous diameters for samples 2, 2.25, 8 d were vertically offset by 0.05, 0.10, 0.15 /nm, respectively. The SPP synthesis mixture composition before hydrothermal treatment was 10 SiO_2 : 3 TBPOH : 100 H_2O : 40 EtOH.

In summary, a low hydrothermal temperature (T ~ 115 ℃) is necessary to ensure the formation of the single-unit-cell pillared structure in SPP synthesis, and such a structure

can hold up to 8 days at 115 ℃. However, as a high hydrothermal temperature is used (T > 115 ℃), the layer thickening of SPP zeolites can be observed and a longer hydrothermal reaction time may destroy the pillared morphology, forming a microporous zeolite that is close to the conventional MFI structure.

3.3.2 Silica/SDA ratios

The effect of silica/SDA ratio on the MFI/MEL intergrowth in SPP zeolites synthesis was studied by varying silica and TBPOH content respectively. Specifically, the chemical compositions of 10 SiO_2 : 4/3/2/1 TBPOH : 100 H_2O : 40 EtOH and 20/15/10 SiO_2 : 3 TBPOH : 100 H_2O : 40 EtOH were investigated in this section.

When SiO_2/TBPOH ratio was high (SiO_2/TBPOH = 10.0 or 6.66), the silica cannot be well dissolved and the gels were not clear after 24 h hydrolysis at room temperature. As the SiO_2/TBPOH ratio was reduced to 5.0, the synthesis with high silica content in the composition (15 SiO_2 : 3 TBPOH : 100 H_2O : 40 EtOH) led to a deteriorated pillared structure (Figure 3-4, g and h), while the synthesis with low silica content (10 SiO_2 : 2 TBPOH : 100H_2O : 40EtOH) led to a layered structure with less pillars observed under TEM (Figure 3-4, e and f). When SiO_2/TBPOH ratio further decreased to 3.3 and 2.5 (10 SiO_2 : 3/4 TBPOH : 100 H_2O : 40 EtOH), typical “house-of-cards” structures with single-unit-cell layers were observed (a–d in Figure 3-4), indicating that a certain range of SiO_2/TBPOH ratio is essential to ensure the formation of pillars, and thus the MFI/MEL intergrowths. Without a clear indication, all SPP zeolites were synthesized with Silica/SDA ratio around 3.3 in the rest of this dissertation.

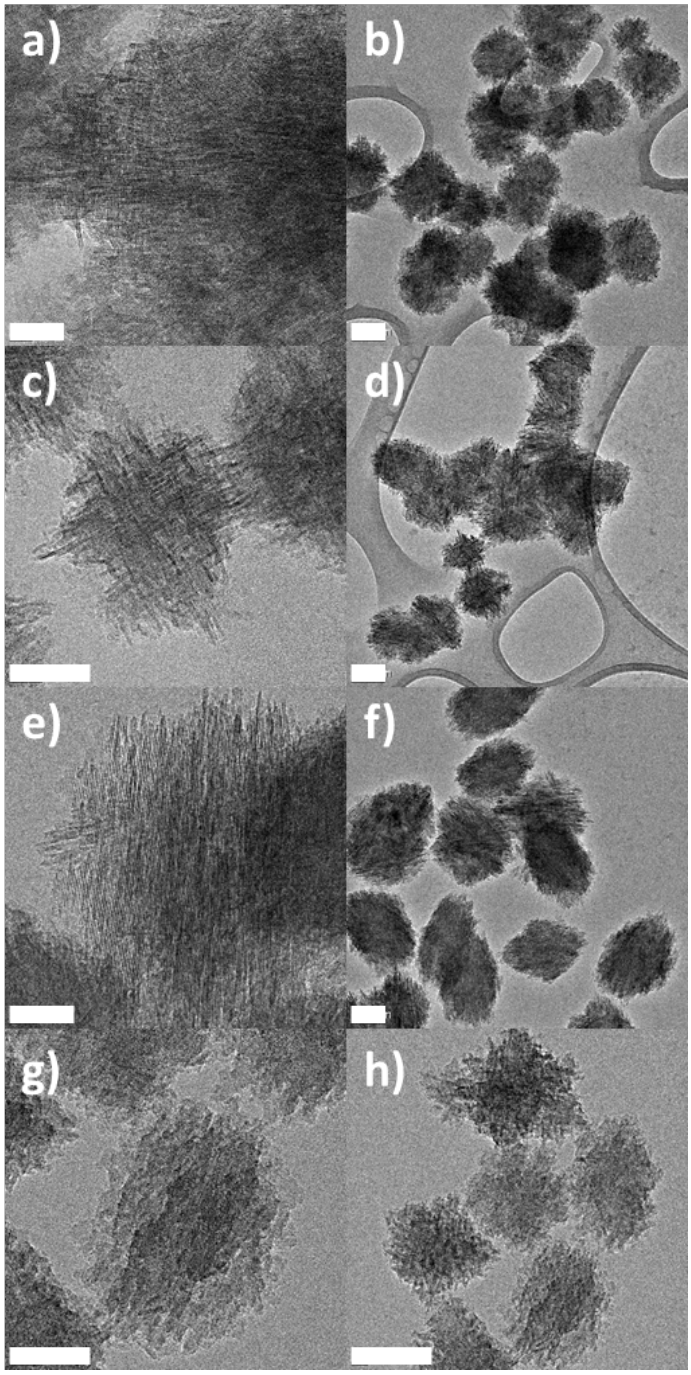

Figure 3-4 TEM characterization of SPP zeolite with different silica/SDA ratios. a) and b) $10SiO_2$:4TBPOH:$100H_2O$:40EtOH. c) and d) $10SiO_2$:3TBPOH:$100H_2O$:40EtOH. e) and f) $10SiO_2$:2TBPOH:$100H_2O$:40EtOH. g) and h) $15SiO_2$:3TBPOH:$100H_2O$:40EtOH (Scale bar: 50 nm in a, c, e, g); 100 nm in b, d. f, h).)

An alternative silica source, fumed silica, can also be used to synthesize SPP zeolites using the same initial composition of 10 SiO_2 : 3 TBPOH : 100 H_2O : 40 EtOH. Severe aggregations with significantly increased particle sizes were observed under TEM. However, the pillared structure can still be detected at the edge of the particles, as shown in Figure 3-5.

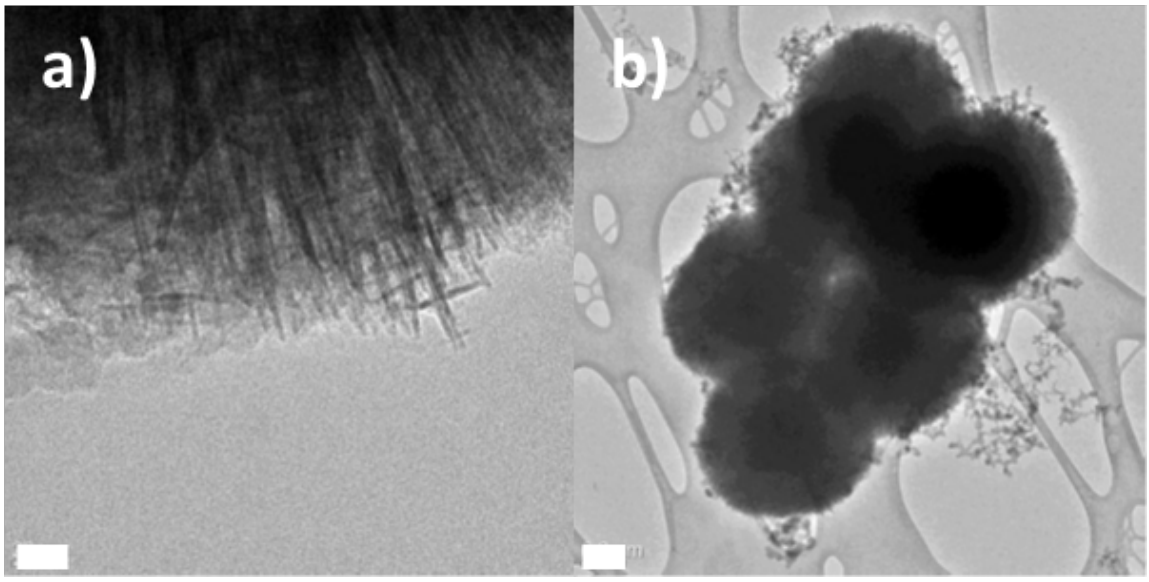

Figure 3-5 TEM characterization of SPP zeolite with fumed silica as silica source at composition of $10SiO_2$:3TBPOH:$100H_2O$:40EtOH (Scale bar: 20 nm in a); 200 nm in b).)

3.3.3 Dual-SDAs

As discussed in section 2.3.1, both tetrabutyl ammonium (TBA^+) and tetrabutyl phosphonium cations (TBP^+) could be used to synthesize SPP zeolites (Xu *et al.*, 2014). While tetrabutyl SDAs might favor the MFI/MEL intergrowth, tetrapropyl SDA (e.g. TPA^+) is commonly used to direct the formation of MFI phase (Davis and Lobo, 1992). Considering that the ethyl chain of tetraethyl ammonium cation (TEA^+) could be complementary to the butyl chain of TBP^+ in terms of the length of alky chain, and

perhaps be better accommodated in the MFI channel with TBP^+, the use of two SDAs might favor the growth of MFI phase. Therefore, as an attempt to alter the MFI/MEL intergrowth in SPP structure, TEA^+ was introduced during the SPP synthesis as a secondary SDA. Specifically, different percentages of TBP^+ were replaced with TEA^+ and the corresponding morphologies were examined under TEM.

As shown in Figure 3-6, the "house-of-cards" structure in SPP eventually disappeared with the increased molar percentages of TEA^+ and a bulk microporous MFI was formed at the composition with 7% of TEA^+. The morphology change suggests that the introduction of TEA^+ could destroy the pillared structure, leaving less or no mesopore in the structure. Argon adsorption isotherms were measured to further examine the change of mesoporosity.

As shown in Figure 3-7, the two adsorption branches of SPP synthesized with and without TEA^+ overlap at low relative pressure ($p/p_0 < 0.1$), indicating no significant layer thickening was observed in the samples that synthesized with 1% TEA^+. However, the hysteresis loop ($0.2 < p/p_0 < 0.8$) is not clear in the 1% TEA^+ sample. A significantly reduced mesopore volume was observed in the pore size distribution simulated based on the adsorption branch (see the insert in Figure 3-7), confirming the observation of more layer structures with less pillars under TEM. Although the mesopore volume decreased, the mesopore size did not change, indicating that TEA^+ did not alter the MFI/MEL intergrowth frequency.

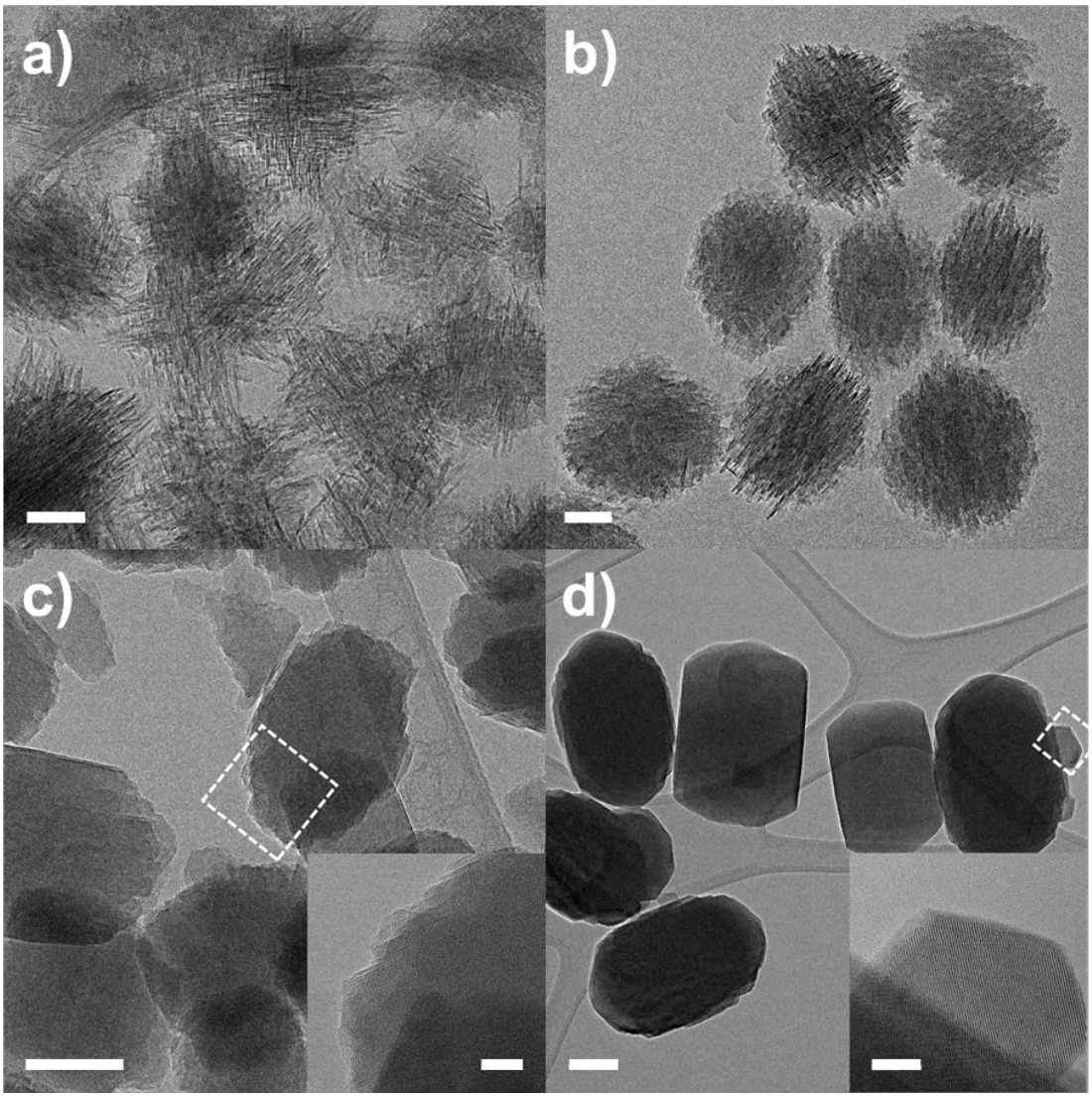

Figure 3-6 TEM images of SPP synthesized with dual-SDAs. The molar percentage of the secondary SDA are: a) 0% TEAOH; b) 1.3% TEAOH; c) 3.7% TEAOH; d) 7.0% TEAOH. The chemical composition of clear sols is 10 SiO_2 : 3 SDAs : 100 H_2O : 40 EtOH in all samples. (Scale bar: 50 nm in a, b); 20 nm in insert in c, d); and 100 nm in c, d).)

As shown in Figure 3-7, the two adsorption branches of SPP synthesized with and without TEA^+ overlap at low relative pressure ($p/p_0 < 0.1$), indicating no significant layer thickening was observed in the samples that synthesized with 1% TEA^+. However, the

hysteresis loop ($0.2 < p/p_0 < 0.8$) is not clear in the 1% TEA^+ sample. A significantly reduced mesopore volume was observed in the pore size distribution simulated based on the adsorption branch (see the insert in Figure 3-7), confirming the observation of more layer structures with less pillars under TEM. Although the mesopore volume decreased, the mesopore size did not change, indicating that TEA^+ did not alter the MFI/MEL intergrowth frequency.

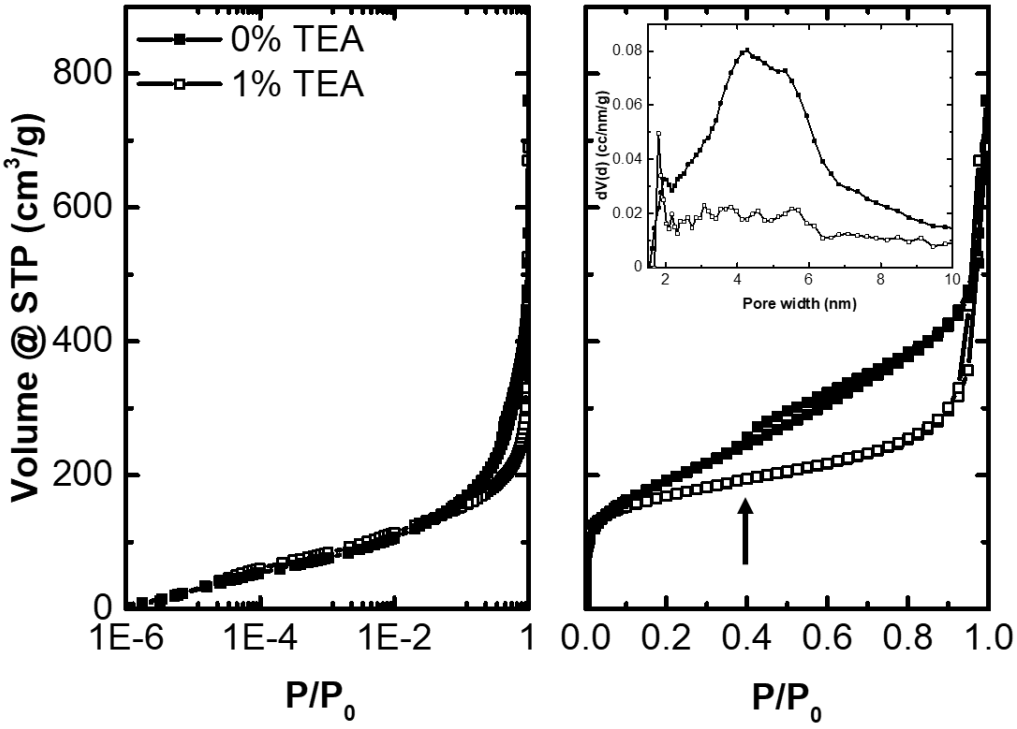

Figure 3-7 Argon (87.3 K) adsorption isotherms of SPP synthesized with dual-SDAs. Left: on a log scale. Right: on a linear scale (arrow pointed to the start of hysteresis loop), and the insert is the mesopore size distribution using NLDFT/GCMC simulation based on cylindrical pore model.

Additional experiments that partially replace TBP^+ with TPA^+ or tetramethyl ammonium cation (TMA^+) as a secondary SDA were also attempted here. Unlike the case of TEA^+,

when 1% TBP^+ was replaced with TPA^+ or TMA^+, no significant change in morphology was observed under TEM (see a) and c) in Figure 3-8). An obvious layer thickening was only observed when the secondary SDA content was increased to 2% (see b) and d) in Figure 3-8). The pillared structures were well-preserved in all cases shown in Figure 3-8.

The change of mesoporosity was further examined through the measurement of argon absorption isotherm. At low relative pressure ($p/p_0 < 0.1$), increased adsorption volumes of argon were found per gram of SPP with 2% TPA^+ and TMA^+ (see Figure 3-9, left), confirming the layer thickening observed in both samples under TEM. The pore size distributions simulated based on the adsorption branches further show the change of mesopore volume. A significantly reduced mesopore volume was found in the sample of SPP synthesized with 2% TPA^+, which is similar as observed in the SPP sample with 1% TEA^+. However, the mesopore volume was less affected in the SPP synthesized with 2% TMA^+, where only a slight decrease was detected compared to the control group (SPP synthesized without a secondary SDA), suggesting a better preservation of the pillared structure. Therefore, TMA^+ could be a good candidate as the secondary SDA to obtain thicker layers of SPP zeolites while with little effect on their pillared structures under the investigated synthesis condition.

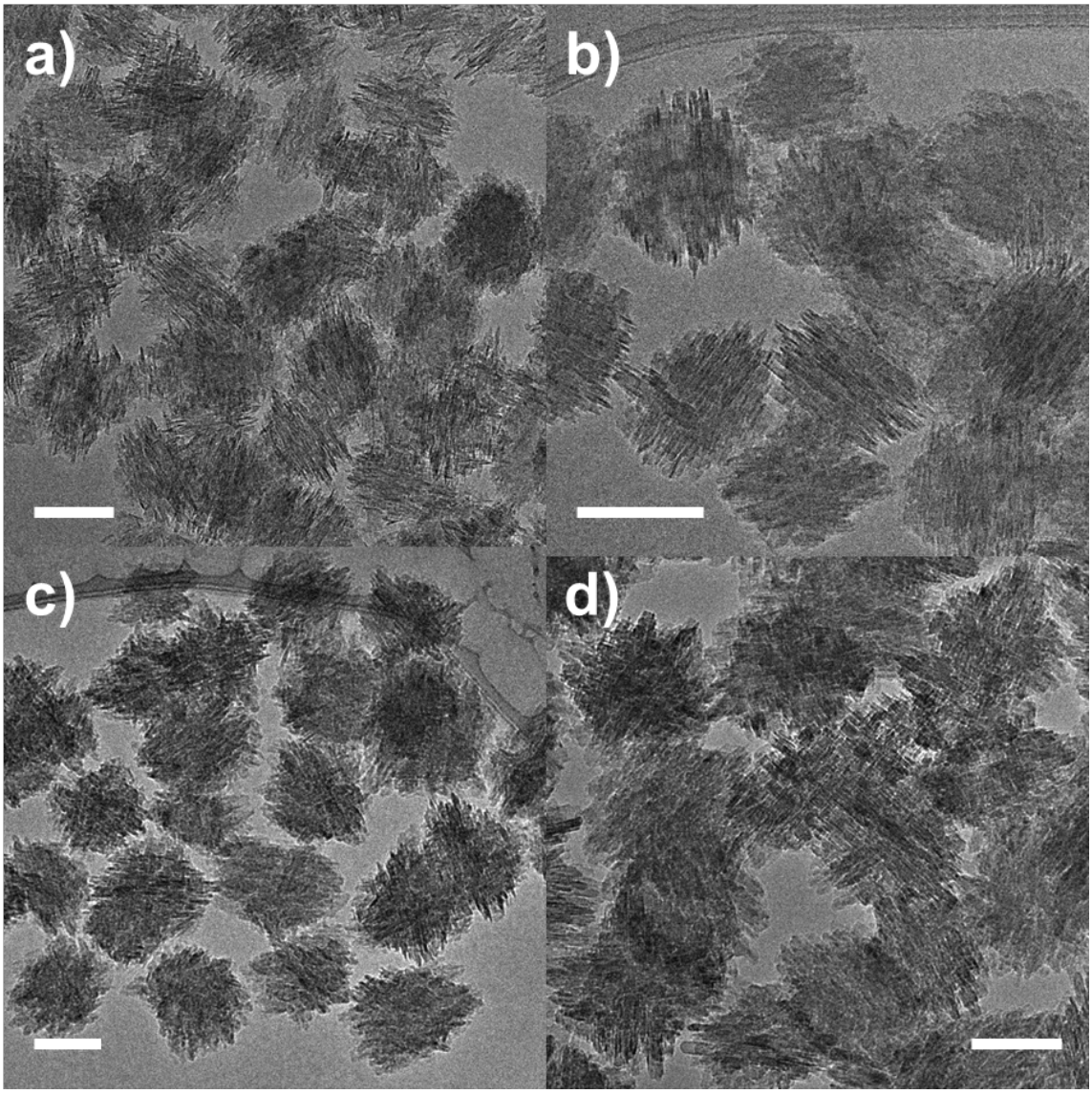

Figure 3-8 TEM images of SPP synthesized with dual-SDAs. The molar percentage of the secondary SDA are: a) 1% TPAOH; b) 2% TPAOH; c) 1% TMAOH; d) 2% TMAOH. The chemical composition of clear sols is 10 SiO_2 : 3 SDAs : 100 H_2O : 40 EtOH in all samples. (Scale bar: 100 nm.)

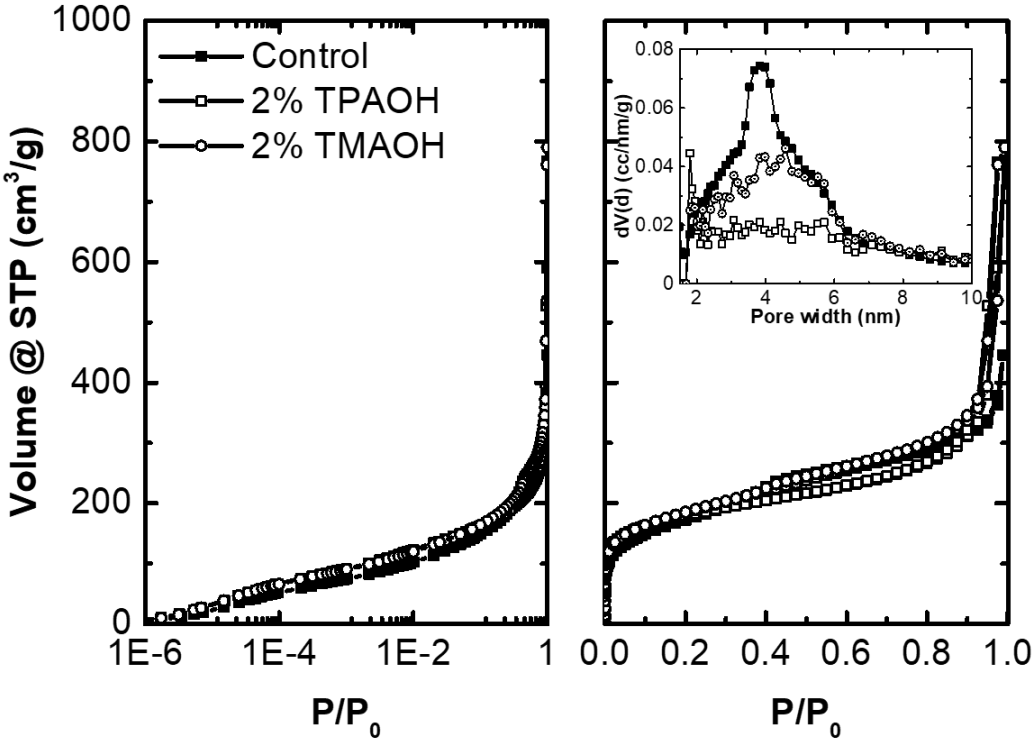

Figure 3-9 Argon (87.3 K) adsorption isotherms of SPP synthesized with dual-SDAs. Left: on a log scale. Right: on a linear scale and the insert is the pore size distribution based on NLDFT/GCMC simulation based on cylindrical pore model.

3.3.4 Al-SPP with different layer thicknesses

As discussed in the pure silica SPP synthesis, two strategies can be used to prepare SPP with thicker layers: using a higher hydrothermal temperature or introducing a secondary SDA. When aluminum was incorporated, however, the thickening of layers was also observed when using a longer hydrothermal reaction time at low hydrothermal temperature (i.e., T = 115 ℃). In Al-SPP synthesis, different aluminum sources can be used, such as aluminum sulfate octadecahydrate, aluminum isopropoxide or gibbsite, and sodium cation is necessary to balance the negative charge caused by framework aluminum. Considering that the metal cations can direct the formation of aluminosilicate

MFI zeolites without any organic template (L. Zhang *et al.*, 2012), the presence of sodium cation may also direct the growth in Al-SPP, causing the layer thickening after a long hydrothermal reaction time.

In the current study, Al-SPP zeolites with various layer thicknesses were synthesized by increasing the hydrothermal temperature, as described in section 3.2.4. A detailed discussion regarding the morphology and acidity of these Al-SPP zeolites were included in section 5.3.1.

3.4 Conclusions

In this chapter, synthesis condition and composition effect on SPP zeolite morphology were studied systematically.

A well-defined single-unit-cell hierarchical structure of SPP zeolite favors low hydrothermal temperature, specifically temperature below 135 ℃. For pure silica SPP, the single-unit-cell layers and the hierarchical structure could be well-preserved up to 8 days at 115 ℃. A higher hydrothermal temperature (T > 135 ℃) or an introduction of a secondary SDA (e.g. TMA^+) will lead to the thickening of layers. Additionally, a certain percentage of tetrabutyl SDA is critical to ensure the MFI/MEL intergrowths, and therefore, the pillared structure. A high silica/SDA ratio or an excess of the secondary SDA will both lead to the formation of conventional microporous MFI zeolites.

Aluminum could be successfully incorporated in the framework without affecting the formation of pillared structure in SPP zeolite synthesis. Different layer thicknesses of Al-SPP can be easily obtained by varying the hydrothermal temperatures. The maximum

Brønsted acid density of Al-SPP can be achieved under the investigated synthesis conditions is around 190 μmol/g (equivalent Si/Al ratio is around 75). For Al-SPP with Si/Al ratio higher than 75, the excess of aluminum, which is not incorporated in the framework, shows Lewis acidity as a result. The Al-SPP zeolites with different layer thicknesses synthesized in this Chapter were further applied in Chapter 5 as the model catalysts to study the structure—activity relationship of hierarchical zeolites.

Chapter 4 Synthesis of self-pillared pentasil zeolites with tunable mesoporosity

4.1 Introduction

Mesoporosity plays an important role in heterogeneous catalysis by reducing the diffusion path length of microporous domains and providing more accessible active sites on the surface (Stöcker, 2008; Ennaert *et al.*, 2016). Considering the hydrothermal stability and acidity (Corma, 1997; Wang, Yu and Xu, 2012), the crystalline zeolites with tunable mesoporosity could be potentially important from a technological point of view to the catalytic reactions involving bulky molecules. The control of mesopore size in hierarchical zeolites can be achieved using special synthetic routes (Wang *et al.*, 2007, 2009), post-treatments (Perez-Ramirez *et al.*, 2009; Guo *et al.*, 2015) or additional templates: (1) "soft templates" such as surfactants (Feng *et al.*, 2010; García-Martínez *et al.*, 2012; Garcia-Martinez *et al.*, 2014; Prasomsri *et al.*, 2015), polymers (Yao, Huang and Wang, 2010), organosilanes (Choi *et al.*, 2006), aerogels (Tao *et al.*, 2005); and (2) "hard templates" such as carbon (Fan *et al.*, 2008; Chen *et al.*, 2011).

In the case of SPP zeolites, the pillared structure of SPP zeolite is formed based on a crystal growth phenomenon known as twinning, where a higher-symmetry structure (MEL) acts as a connector to allow the orthogonal growth of lower-symmetry structure (MFI) nanosheets, as discussed in Chapter 2. The mesoporosity is thus formed between the MFI nanosheets (X. Zhang *et al.*, 2012; Xu *et al.*, 2014; Swindlehurst *et al.*, 2015). In

principle, the control of mesopore size in SPP zeolites could be achieved by changing the intergrowth frequency.

MFI/MEL intergrowth is commonly seen in zeolites (Hay, Jaeger and Wilshier, 1990; Okubo *et al.*, 2001; Willhammar *et al.*, 2012; Thomas *et al.*, 2013; Sławiński *et al.*, 2014; Smeets *et al.*, 2014; Sholl and Lively, 2015). The formation of such a intergrowth is often related to SDAs (Francesconi *et al.*, 2005; González *et al.*, 2007; Burton *et al.*, 2010; Zhao *et al.*, 2017a, 2017b), starting compositions (Lillerud and Raeder, 1986; L. Zhang *et al.*, 2012; Ban, Oishi and Ohya, 2014; Awala *et al.*, 2015; Smith *et al.*, 2015; Khaleel *et al.*, 2016; Wang *et al.*, 2017), or synthesis conditions (Jablonski, Sand and Gard, 1986; Awala *et al.*, 2015). However, how to control the intergrowths in zeolites remains unclear. In Chapter 3, we have discussed the effects of synthetic conditions, SDAs and silica/SDA ratios on SPP zeolites morphologies. While the layer thickness of SPP zeolites could be increased under a high hydrothermal temperature or using a secondary SDA, the mesopore size distribution remained unchanged in all the cases. To make a further attempt on changing the MFI/MEL intergrowth frequency, solvent effect was studied in this Chapter.

In SPP synthesis, the synthetic mixture composition was controlled by mixing a desired amount of silica source with tetrabutyl SDA solution and water (as a solvent). Ethanol was generated as a co-solvent after tetraethyl orthosilicate (TEOS) hydrolysis. However, the water and ethanol fraction could only be adjusted within a limited range through mixing (see the cross points above the red dot line in the composition space as shown in

Figure 4-1). Evaporation of water and ethanol after hydrolysis introduced the risk of aging by using an elevated temperature. To avoid any phase evolution before the hydrothermal step, a freeze-drying technique (Awala *et al.*, 2015; Khaleel *et al.*, 2016) was applied to remove all the remaining water and ethanol in the system. An accurate solvent fraction could then be obtained by adding back the desired amount of water (and ethanol) into the dry gel before the hydrothermal process begins.

Using the freeze-drying technique, attempts have been made to control the MFI/MEL intergrowth frequencies in SPP synthesis by changing the water and ethanol fraction. A wide range of adjustment and an accurate control of the solvent fraction could be achieved. The mesoporosity change was discussed by comparing the argon adsorption isotherms. The effect of freeze-drying technique and the phase to introduce freeze-drying were also studied. This synthesis strategy was further extended to aluminosicate SPP zeolites synthesis.

4.2 Experimental methods

4.2.1 Synthesis of pure-silica SPP zeolites with tunable mesoporosity

In a typical synthesis, 7.464 g tetrabutyl phosphonium hydroxide solution (TBPOH, 40% by weight, Sigma-Aldrich) was added dropwise into 7.500 g tetraethyl orthosilicate (TEOS, Sigma-Aldrich) while stirring, followed by 3.305 g water. The hydrolysis was carried out at room temperature and kept for 24 h with stirring. A clear sol was obtained with the composition of 10 SiO_2 : 3 TBPOH : 100 H_2O : 40 EtOH.

The clear sol was frozen at -80 ℃ overnight before transferring to Lacbonco FreeeZone 4.5 liter Benchtop Freeze-drying system to remove the remaining water and ethanol after hydrolysis. Desired amount of water (and ethanol) was added back to the dry gel before transferring to a Teflon-lined stainless steel autoclave. Hydrothermal treatment was performed in a rotation oven at 388K.

The product was washed with distilled water by repeated centrifugation and decanting of the supernatant, until the pH of the final supernatant was lower than 9. The final precipitate was dried at 343 K for 12 h. Some of the dried product was calcined at 823 K for 12 h in air for further characterizations.

4.2.2 Synthesis of Al-SPP with tunable mesoporosity

Solution A was prepared by dissolving 0.100 g aluminum isopropoxide (Sigma-Aldrich) in 3.662 g TBPOH. Solution B was prepared by adding the rest 6.500 g TBPOH dropwise into 10.211g TEOS while stirring. Sodium hydroxide solution was prepared by dissolving 0.162 g sodium hydroxide in 4.485 g water. A clear solution was obtained by mixing solution A and B, followed by sodium hydroxide solution. The hydrolysis was carried out at room temperature and kept for 24 h with stirring. A clear sol was obtained with the composition of 10 SiO_2 : 0.05 Al_2O_3 : 3 TBPOH : 0.125 NaOH : 100 H_2O : 40 EtOH.

The clear sol was frozen at -80 ℃ overnight before transferring to Lacbonco FreeeZone 4.5 liter Benchtop Freeze-drying system to remove the remaining water and ethanol after hydrolysis. The desired amount of water (and ethanol) was added back to the dry gel

before transferring the gel to a Teflon-lined stainless steel autoclave. Hydrothermal treatment was performed in a rotation oven at 388K.

The product was washed with distilled water by repeated centrifugation and decanting of the supernatant, until the pH of the final supernatant was lower than 9. The final precipitate was dried at 343 K for 12 h, followed by calcination at 823 K for 12 h in air.

The calcined zeolite was mixed with distilled water to yield a 5% (by weight) suspension. The suspension was heated at 343 K for 12 h, and washed once with distilled water by centrifugation and decanting of the supernatant, such that the pH of the supernatant was 6-7. The precipitate was mixed with 1.0 mol L^{-1} ammonium nitrate solution to yield a 5% (by weight) suspension. The suspension was then heated at 353 K for 5 h to allow Na^{+} in the framework to be exchanged with NH^{4+}. The solid was recovered by centrifugation. The process was repeated three times, and the final product was washed with water, dried at 343 K and calcined in air at 823 K for 4 h.

4.2.3 Transmission electron microscopy (TEM)

The morphology of SPP zeolites was determined by transmission electron microscopy. Typically, a specimen was prepared by applying a few droplets of an aqueous suspension of the washed zeolite product onto an ultra-thin carbon coated 400 mesh copper grid on lacey carbon support film (Ted Pella Inc.). In order to study the morphology of smaller particles obtained at early stages, the final suspension after synthesis was diluted 10 times (volume) with H_2O, and deposited on the same type of grid. All TEM images were obtained under an FEI Tecnai G^2 F30 TEM operating at 300 kV using a CCD camera.

4.2.4 Argon adsorption

Argon (87.3K) adsorption was performed using a commercially available automatic manometric sorption analyzer (Quantachrome Instruments AutosorbiQ MP). Prior to adsorption measurements, the samples were outgassed at 573 K for 16 h under turbomolecular pump vacuum. The micro- and mesopore size distributions were simulated based on zeolites/silica (cylindrical, pores, NLDFT ads.) model (Ravikovitch and Neimark, 2001).

4.3 Results and discussion

4.3.1 Water and ethanol effect

The chemical molar composition of pure-silica SPP zeolites is 10 SiO_2 : 3 TBPOH : x H_2O : y EtOH., where x = 100 and y = 40 in the clear sols before hydrothermal step as reported in the earlier study (X. Zhang *et al.*, 2012). To change the amount of water and ethanol of the clear sols, i.e., x and y, freezing-drying technique can be applied as described in section 4.2.1. Different molar compositions of SPP zeolites that were achieved through the freeze-drying route are marked as in the composition space below (see Figure 4-1).

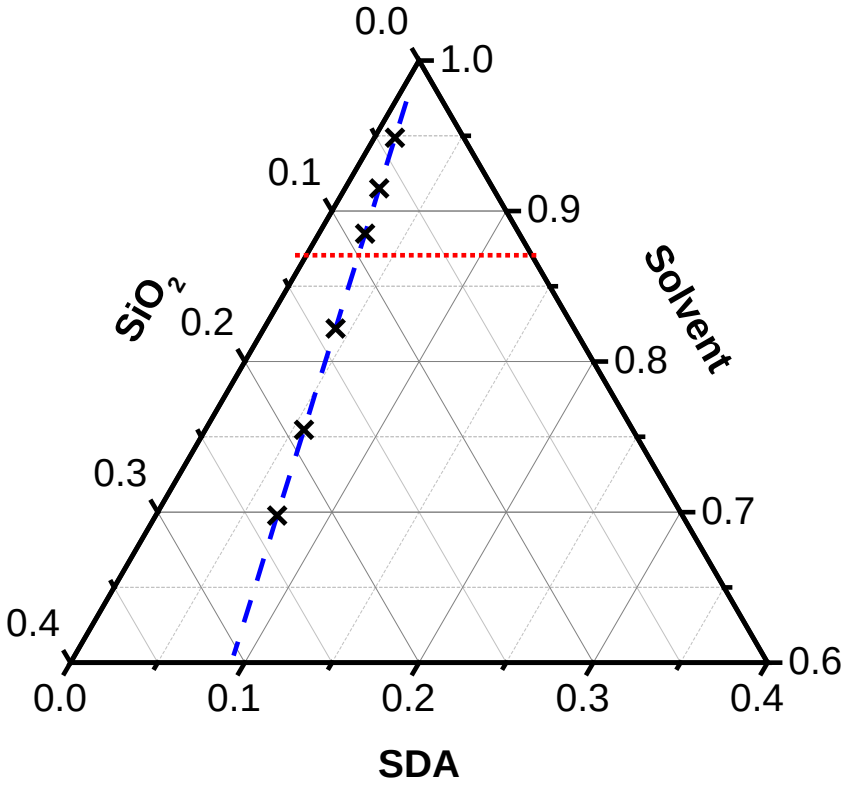

Figure 4-1 Composition space of SPP system. Red dot line indicates the lowest solvent fraction that could be reached from direct mixing. Black cross points are the synthesis mixture compositions from experiments before hydrothermal treatment: 10 SiO_2 : 3 TBPOH : x H_2O : y EtOH from top to bottom in sequence x = 200, 100, 100, 60, 40, 30; y = 40, 40, 0, 0, 0, 0.

According to the TEM in Figure 4-2, SPP zeolites with high water and ethanol contents ($x + y > 100$) showed structures with dense pillars and particle sizes larger than 150 nm. Lower water and ethanol contents ($x + y < 100$) led to the formation of loose pillared SPP structures with particle sizes less than 100 nm. When water and ethanol content was reduced down to 30, the particle size decreased to 60 nm. Meanwhile, a large amount of particles smaller than 50 nm were also observed, which were at the early stage of branching with insufficient pillars to form the intraparticle mesopore (see Figure 4-3). A

further increase of the hydrothermal reaction time from 5 days to 14 days at this water and ethanol content (x + y ~ 30) did not lead to any change of the particle size (see Figure 4-4).

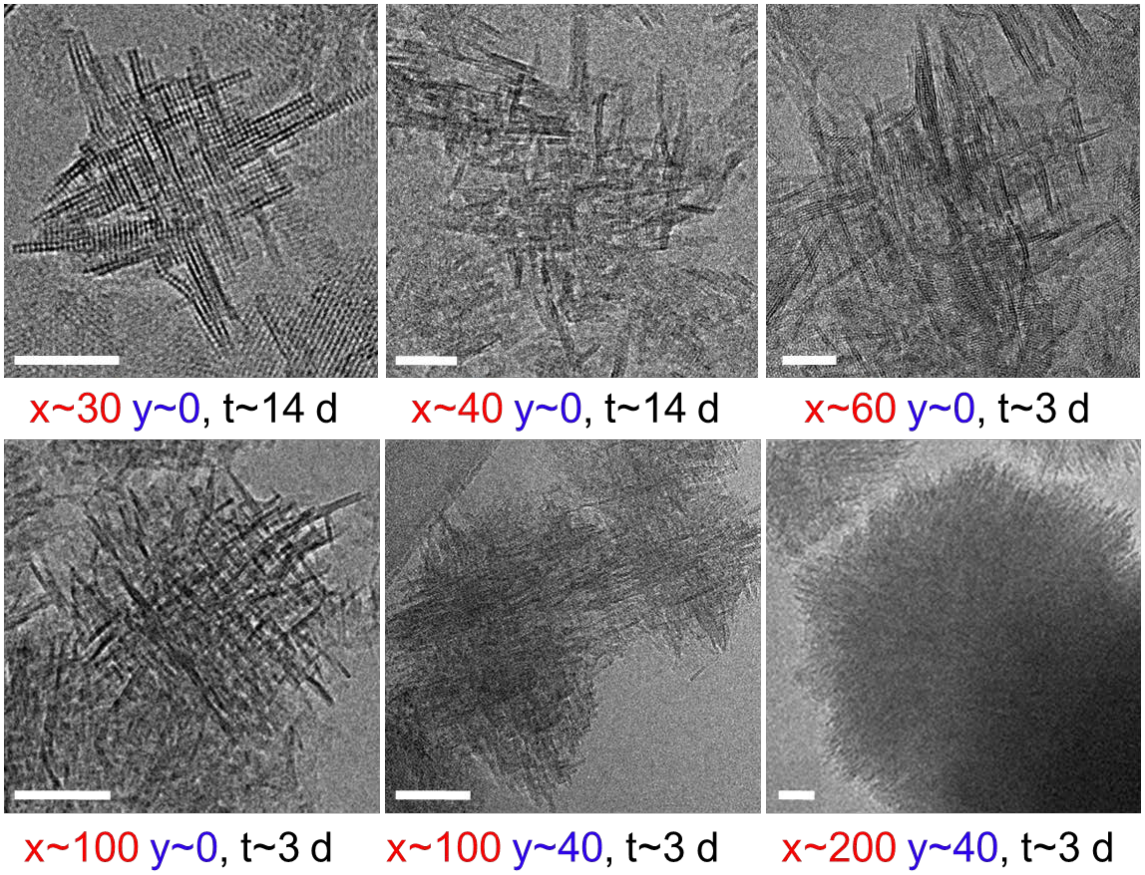

Figure 4-2 TEM images of SPP synthesized with different solvent contents (x + y). SPP composition: 10 SiO_2 : 3 TBPOH : x H_2O : y EtOH, at 115 ℃ in rotational oven for t days. x, y and t values are listed below each figures. (Scale bars: 20 nm in top and 50 nm in bottom.)

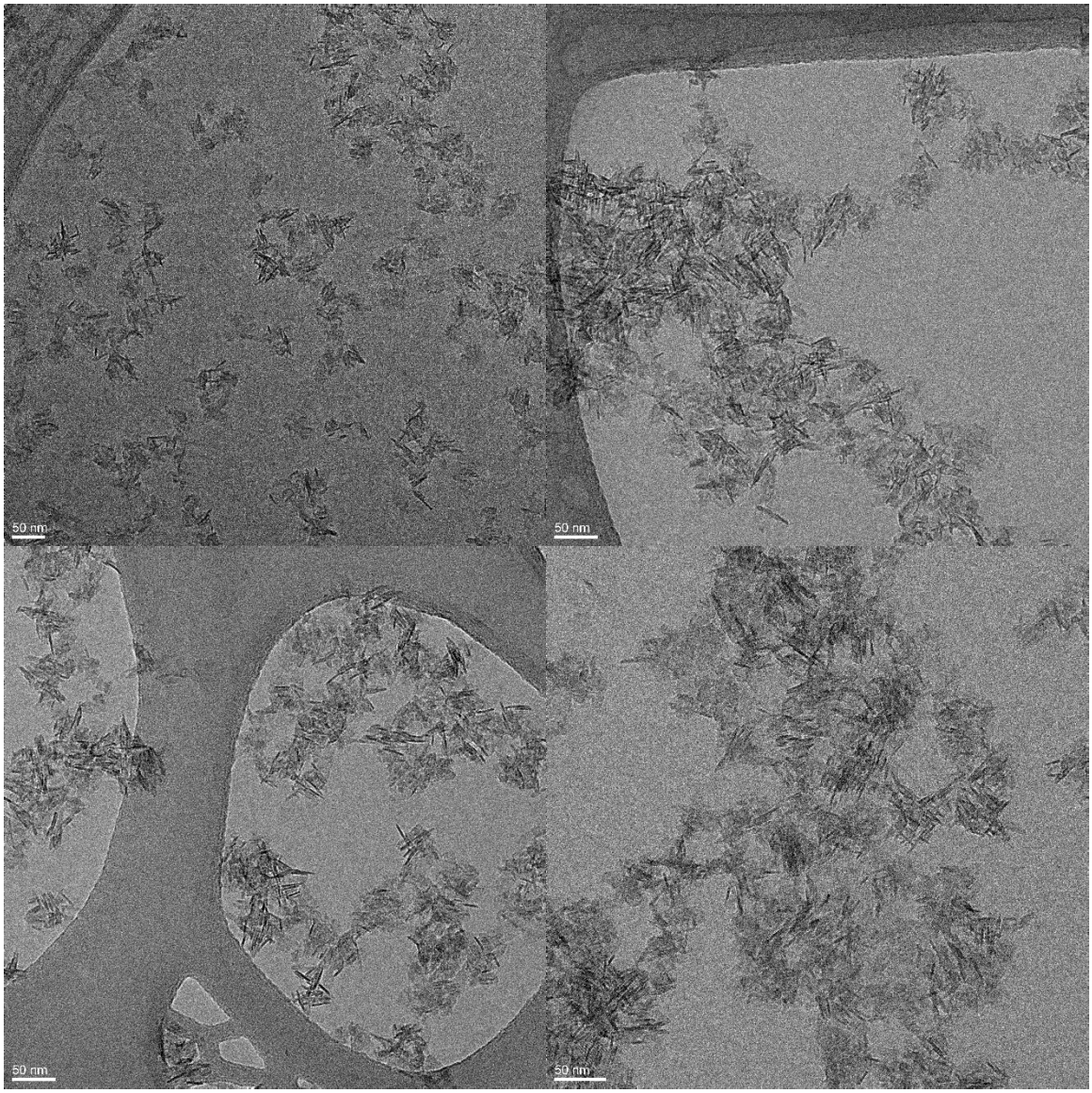

Figure 4-3 Low magnification TEM images of SPP synthesized with the chemical composition of 10 SiO_2 : 3 TBPOH : 30 H_2O (Scale bar: 50 nm)

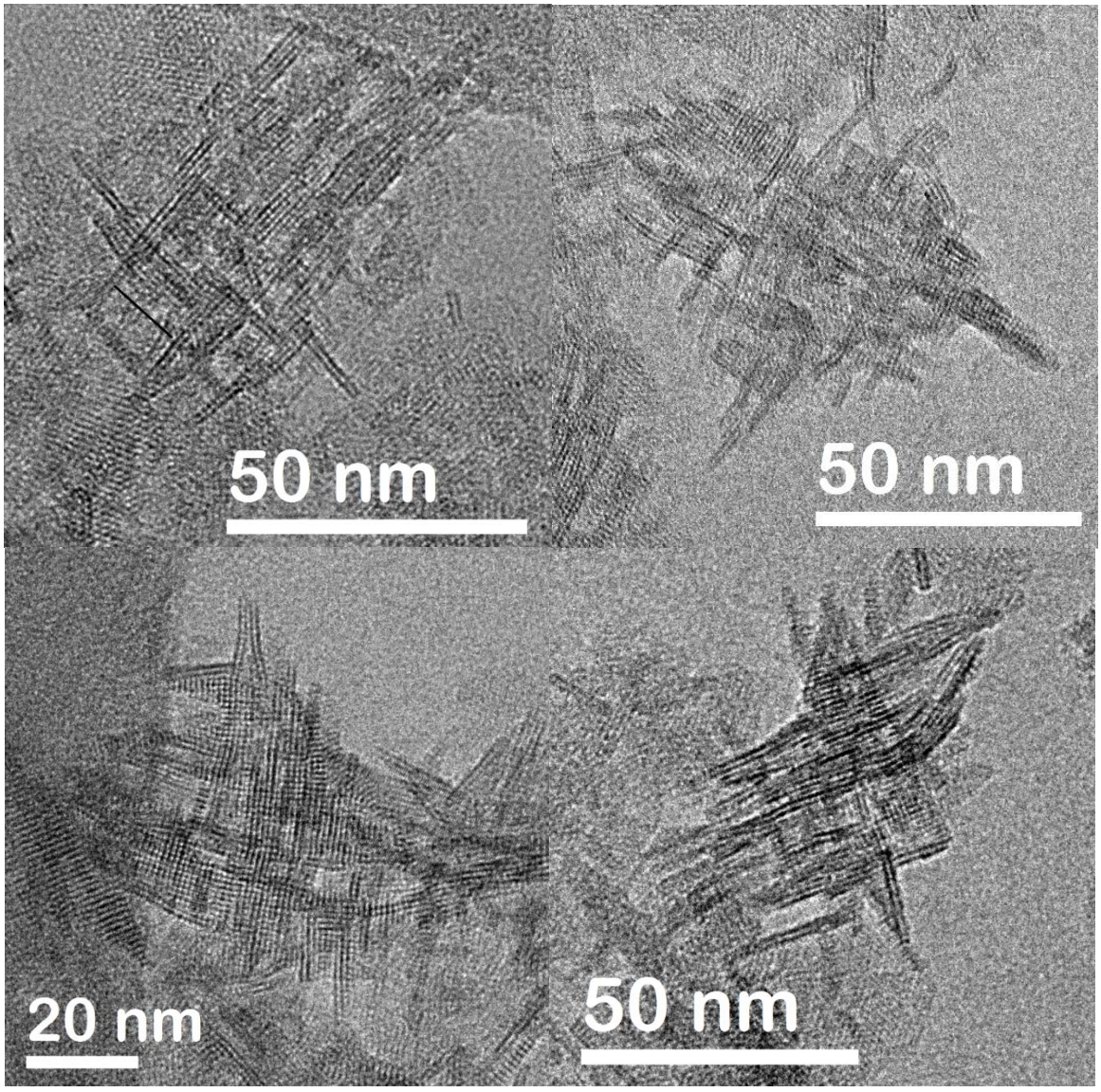

Figure 4-4 TEM images of SPP with the chemical composition of 10 SiO_2 : 3 TBPOH : 30 H_2O using different hydrothermal reaction times: a) 5 days; b) 7 days; c) 12 days; d) 14 days.

According to the argon adsorption isotherms in Figure 4-5, the start of hysteresis loop shifted to high relative pressure (p/p_0 ~ 0.5) when the water and ethanol content was low. An increased adsorption volume was also observed at high relative pressure ($0.6 < p/p_0 < 0.8$). This change of the adsorption isotherms indicated the formation of a larger

mesopore population at low water and ethanol content. When the water and ethanol content (x + y) was down to 30, the adsorption isotherm was close to H2 hysteresis based on the IUPAC classification, suggesting the mesoporosity was more disordered. This is consistent with the observation in TEM where the particles were less uniformed, forming a significant number of interparticle mesopores between particles.

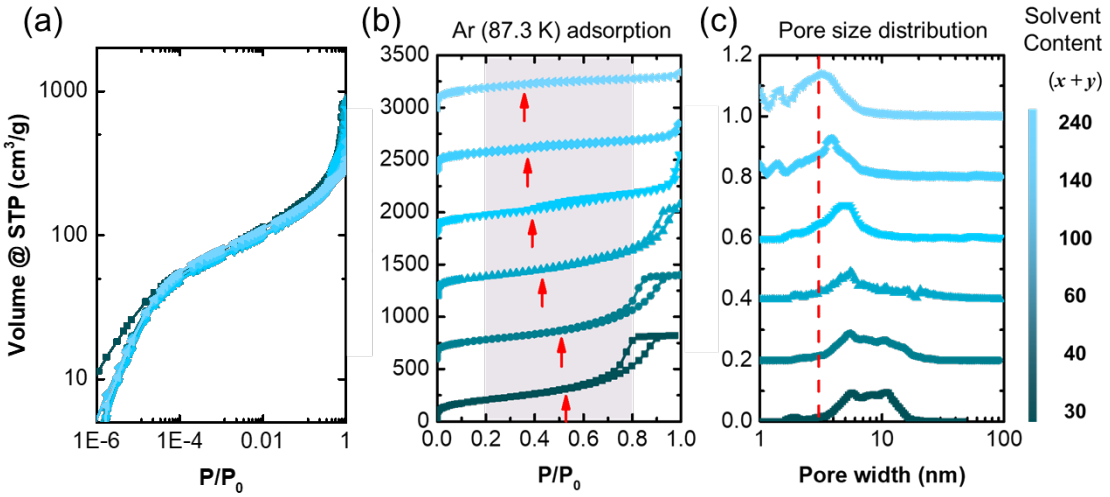

Figure 4-5 Argon (87.3 K) adsorption isotherms of SPP with different solvent contents (x + y). (a) on a log scale (b) on a linear scale. The isotherms were vertically offset by 0, 600, 1200, 1800, 2400, 3000 cm^3/g respectively. The red arrows point to the start of hysteresis loop. (c) The corresponding normalized mesopore size distribution (NLDFT/GCMC, cylindrical pore model). The distribution of mesoporous diameters were vertically offset by 0, 0.2, 0.4, 0.6, 0.8, 1.0 /nm, respectively. The SPP synthesis mixture composition before hydrothermal treatment was 10 SiO_2 : 3 TBPOH : x H_2O : y EtOH, x = 30, 40, 60, 100, 100, 200 and y = 0, 0, 0, 0, 40, 40 for samples from bottom to top. The synthesis of samples with solvent content of 140 and 240 did not use the freeze-drying technique. Samples with solvent content of 30 and 40 used 14 days and the rest samples used 3 days for hydrothermal growth.

4.3.2 Freeze-drying effect

To check the freeze-drying influence on the intergrowth frequency, SPP zeolites were synthesized with and without freeze-drying step using the same chemical composition of 10 SiO_2 : 3 TBPOH : 100 H_2O : 40 EtOH and the same hydrothermal conditions.

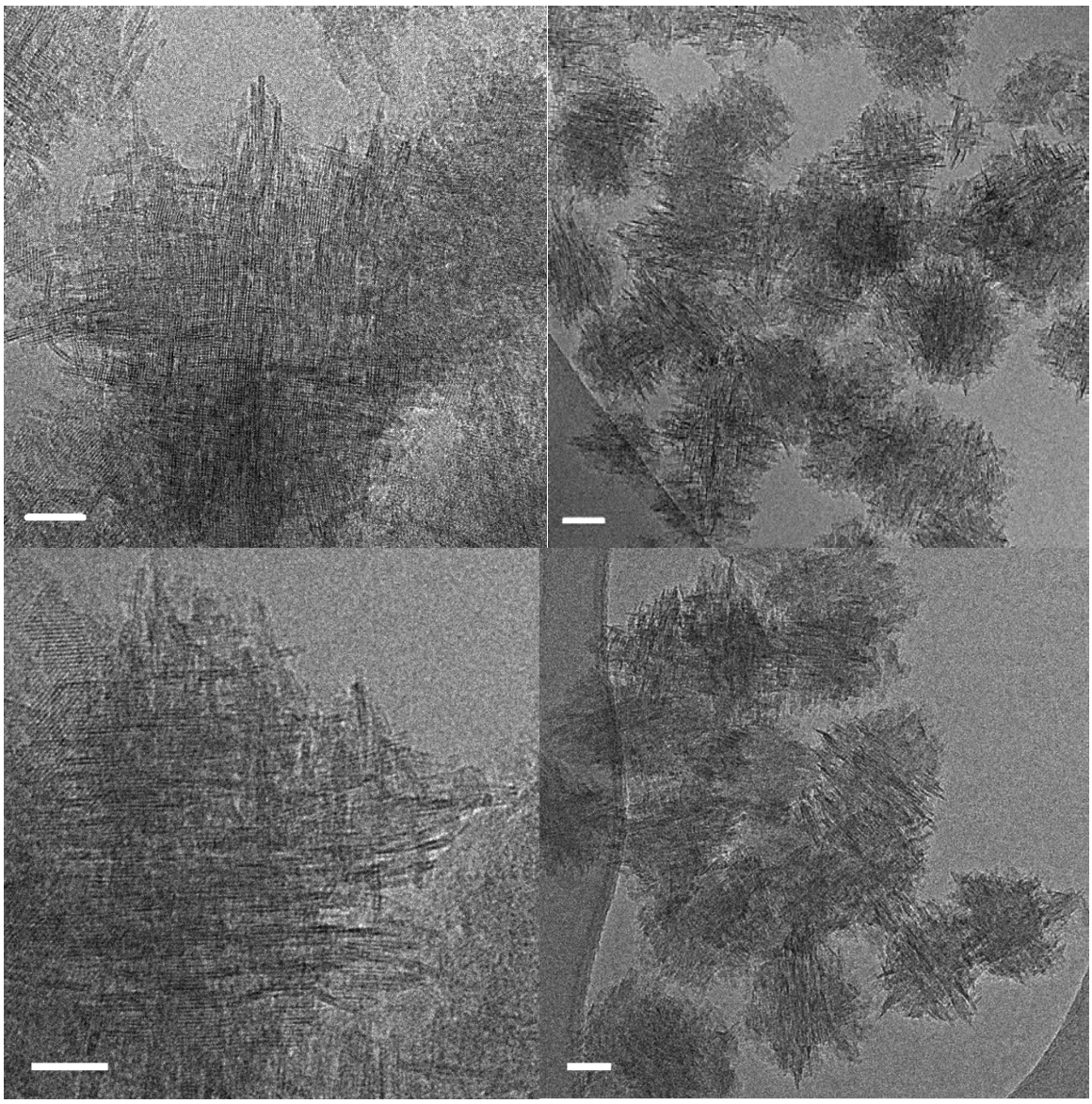

Figure 4-6 TEM images of SPP zeolites with chemical composition of 10 SiO_2 : 3 TBPOH : 100 H_2O : 40 EtOH synthesized without the freeze-drying step (top) and with the freeze-drying step (down). (Scale bar: 20 nm in the left; 50 nm in the right)

According to the TEM images (see Figure 4-6), no significant difference in morphology was detected between samples synthesized with or without the freeze-drying step. The argon adsorption isotherms at low relative pressure (p/p_0 < 0.1) showed the same

adsorption volume uptake (see Figure 4-7, left), confirming the same single-unit-cell layer thickness of microporous domains in both samples. The same starting pressure of the hysteresis loops in both samples indicates no detectable change of mesopore size. Only a slightly lower mesopore volume was found in the freeze-drying sample according to the mesopore size distributions simulated based on the adsorption branches. As a conclusion, the freeze-drying technique did not affect the intergrowth frequency during SPP synthesis.

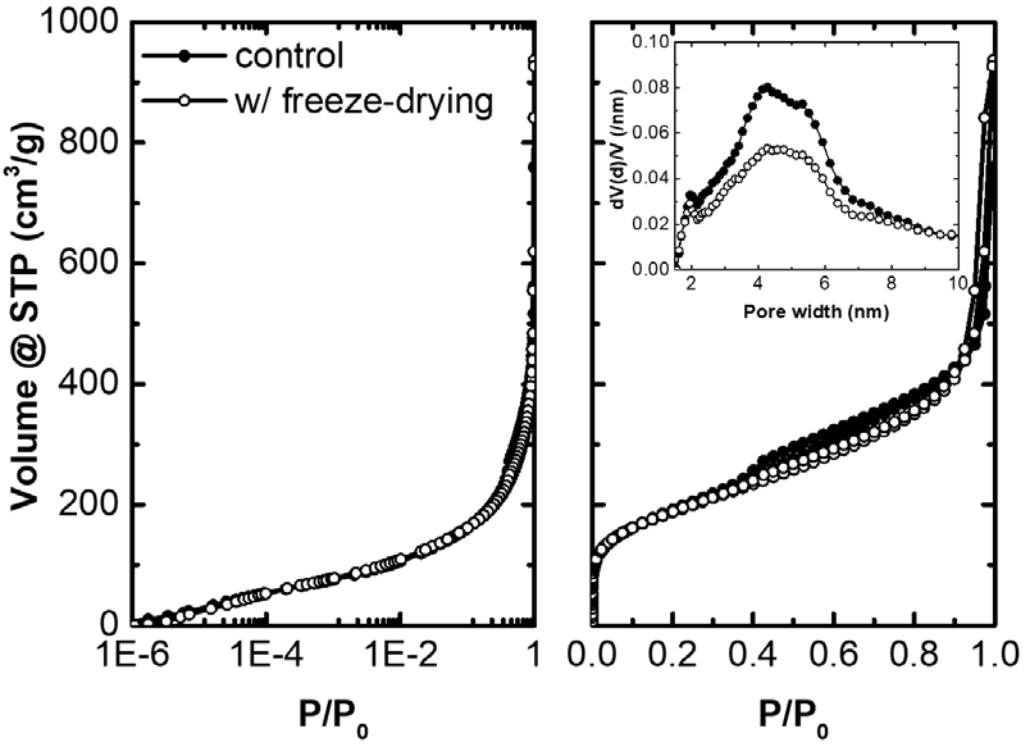

Figure 4-7 The comparison of argon (87.3 K) adsorption isotherms between SPP synthesized with and without freeze-drying step using the same composition 10 SiO_2 : 3 TBPOH : 100 H_2O : 40 EtOH. Left: on a log scale. Right: on a linear scale (the corresponding normalized mesopore size distribution (NLDFT/GCMC, cylindrical pore model) in the insert).

4.3.3 The timing of the freeze-drying step

Previous studies on the FAU/EMT system suggested that the amorphous aggregates before nucleation could significantly affect the intergrowth during crystallization (Khaleel *et al.*, 2016). Therefore, the phase (or time) to start the freeze-drying may directly affect the intergrowths in the final products. In this section, the timing of the freeze-drying step was further studied to examine the effect on the MFI/MEL intergrowths in SPP zeolites.

As discussed in Chapter 2, the SPP phase evolution can be divided into three parts: the formation of 1) nanoparticle precursor; 2) nanosheet; and 3) repetitive-branching structure (Xu *et al.*, 2014). During the phase 1, 2 nm precursor nanoparticles formed from hydrolysis and a larger precursor nanoparticle population formed after aging under heating condition (Swindlehurst *et al.*, 2015). Freeze-drying was then applied before and after the presence of large precursor nanoparticle by using different aging conditions. According to the TEM images in Figure 4-8 and argon adsorption isotherms in Figure 4-9, no significant difference was detected among the samples frozen at different precursor status. Therefore, for the MFI/MEL system, the precursor status (i.e., the timing of the freeze-drying step) does not have any effect on the SPP morphologies.

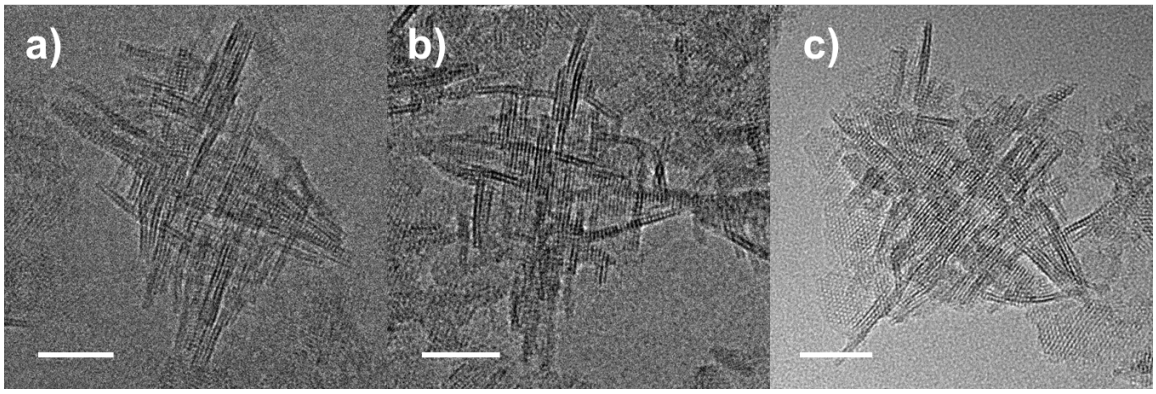

Figure 4-8 TEM images of SPP synthesized with freeze-drying at different aging conditions. a) room temperature for 1 day; b) 80 ºC for 2 days; c) 80 ºC for 2 days and 115 ºC for 5 hours, using the same composition 10 SiO_2 : 3 TBPOH : 30 H_2O : 0 EtOH. (Scale bar: 20 nm)

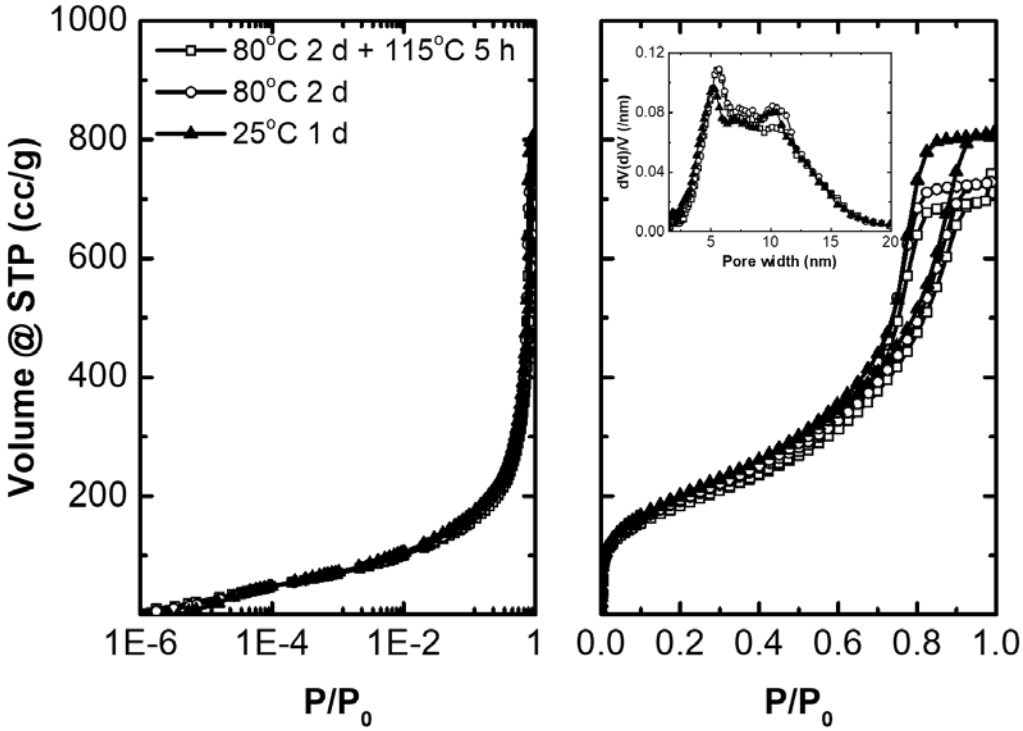

Figure 4-9 The comparison of argon (87.3 K) adsorption isotherms between SPP synthesized with freeze-drying at different aging conditions, using the same composition 10 SiO_2 : 3 TBPOH : 30 H_2O : 0 EtOH. Left: on a log scale. Right: on a linear scale (the corresponding normalized mesopore size distribution (NLDFT/GCMC, cylindrical pore model) in the insert).

4.3.4 Particle size effect

Apart from the change in mesoporosity, SPP zeolites synthesized with lower water and ethanol contents showed smaller particle sizes even with significantly longer hydrothermal reaction times, as discussed in 4.3.1. It is possible that the open structure (large mesopore size) of SPP zeolite is associated with the small particle size, which may eventually form to large SPP zeolites with dense pillars (small mesopore size). However, this possibility can be easily ruled out based on the study in section 3.3.1.

Considering that the prolonged hydrothermal reaction time up to 14 days did not lead to a significant increase in particle size when the water and ethanol content (x + y) was around 30, a higher water and ethanol content (x + y) of 140 can be used instead, and the small particle size can be obtained using a short hydrothermal reaction time, as shown in Figure 3-2.The argon adsorption isotherms suggest no detectable change of the start of hysteresis loop between the SPP zeolites with small and large particle size, as shown in Figure 3-3. Therefore, a wider mesopore distribution with the presence of larger mesopore population is not relevant to the small particle size.

In conclusion, by ruling out the freeze-drying, freeze-drying timing and particle size effect, we conclude that the increase of mesopore size in SPP structure is a result of the reduced water and ethanol content before the hydrothermal treatment.

4.3.5 Open structure aluminosilicate SPP (Al-SPP)

This freeze-drying strategy was further applied in Al-SPP synthesis. As shown in the TEM images (see Figure 4-10), the same solvent effect was also observed in Al-SPP

synthesis. A small particle size with less pillar frequency was observed when the water and ethanol content was low. The adsorption isotherms (see Figure 4-11) further confirmed the increased mesopore size in Al-SPP zeolites using low water and ethanol contents.

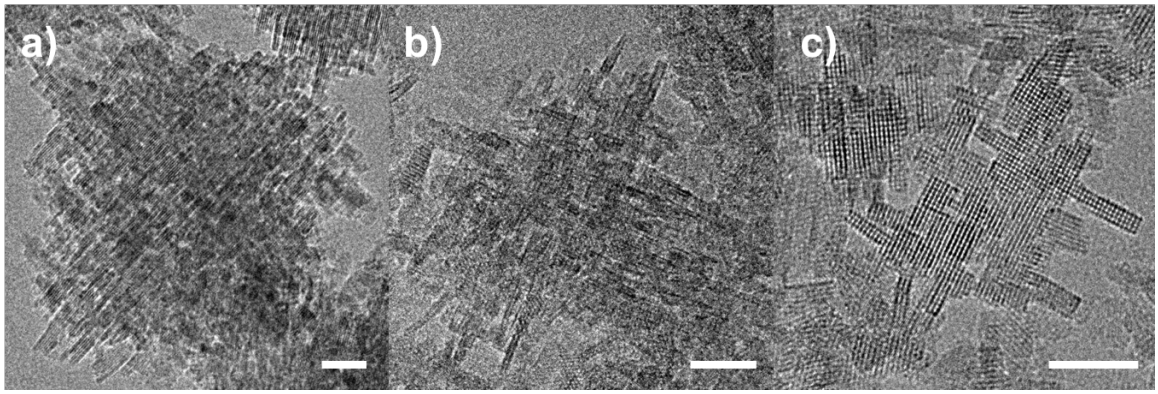

Figure 4-10 TEM images of Al-SPP synthesized with different solvent contents (x + y). a) x = 100, y = 40; b) x = 90, y = 0; c) x = 50, y = 0. (Scale bars: 20 nm.)

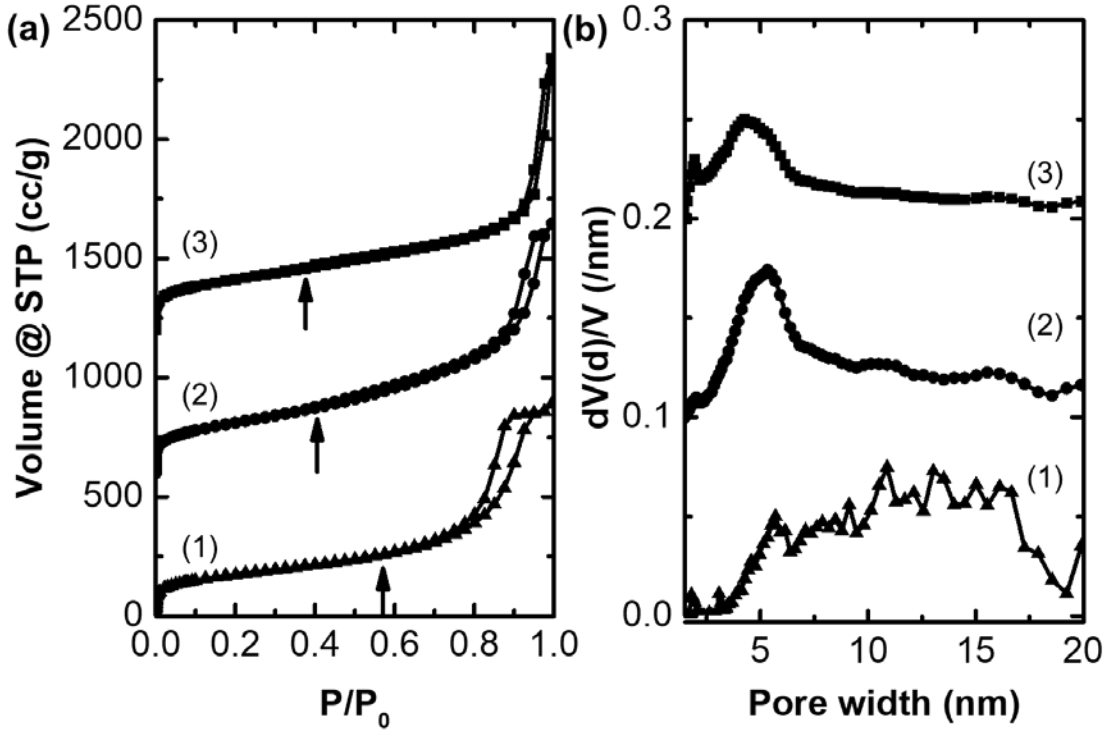

Figure 4-11 (a) Argon (87.3 K) adsorption isotherms of Al-SPP with different solvent contents (x+y). The isotherms for samples (2, 3) were vertically offset by 600, 1200 cm^3/g respectively. Arrows point to the start of hysteresis loop. (b) The corresponding normalized mesopore size distribution (NLDFT/GCMC, cylindrical pore model). The distribution of mesoporous diameters for samples (2, 3) were vertically offset by 0.1, 0.2 /nm, respectively. The Al-SPP synthesis mixture composition before hydrothermal treatment was 10 SiO_2 : 0.05 Al_2O_3 : 3 TBPOH : 0.125 NaOH : x H_2O : y EtOH, x = 50, 90, 100 and y = 0, 0, 40 for sample (1-3) respectively. The synthesis of sample (3) did not include the freeze-drying step.

The Si/Al ratio of Al-SPP was determined by ICP-OES, and the incorporation of aluminum (framework aluminum) was checked by measuring the Brønsted acid sites density through Hoffman elimination of isopropylamine using the reactive gas chromatography (RGC) technique (Abdelrahman *et al.*, 2017). As shown in Table 4-1, no significant difference was detected in terms of the Si/Al ratio between the Al-SPP

synthesized with high (without freeze-drying step) and low solvent contents (with freeze-drying step), and the Brønsted acid sites densities were also similar. Therefore, the freeze-drying route, where low water and ethanol content was applied before the hydrothermal step, did not affect the aluminum incorporation efficiency.

Table 4-1 Summary of acid site information in Al-SPP with composition 10 SiO_2 : 0.05 Al_2O_3 : 3 TBPOH : 0.125 NaOH : x H_2O : y EtOH

	Freeze-drying	Si/Al	Brønsted acid sites density (μmol/g)
x = 100, y = 40	N	60	174
x = 50, y = 0	Y	56	194

In conclusion, this freeze-drying synthetic approach can be extended to the Al-SPP system to manipulate the solvent content before the hydrothermal reaction. Similar to the mesoporosity change in pure-silica SPP, a larger mesopore population with wide pore size distribution was also found in Al-SPP when the solvent content was low. The resulting Al-SPP zeolite with a small particle size and more open mesopore structure could minimize the diffusion resistance within the particle (inside the mesopore) and serves as an ideal catalyst candidate for the catalytic reactions involving bulky molecules.

4.4 Conclusions

The adjustment of solvent content could cause a change in MFI/MEL intergrowth frequency, and lead to a tunable mesoporosity in SPP zeolites. Different water and ethanol contents (x + y) can be achieved and accurately controlled through the freeze-drying technique. No additional effect on SPP structure was detected due to the use of freeze-drying or the time to introduce the freeze-drying. The formation of large mesopore is directly related to the reduced water and ethanol content (x + y) regardless of the

change in particle size. This freeze-drying strategy can also be applied to aluminosilicate SPP synthesis to obtain acid catalysts with larger mesopore sizes to accommodate bulky reactants or transition states.

Chapter 5 Quantitative study of catalytic behavior of hierarchical zeolites formed by repetitive intergrowth

5.1 Introduction

The improved catalytic performance exhibited by hierarchical zeolites compared to that of their microporous-only counterparts has stimulated renewed efforts for the development of novel hierarchical structures as well as interest for industrial implementation (Holm *et al.*, 2011; Pérez-Ramírez *et al.*, 2011; Parlett, Wilson and Lee, 2013; Perego and Millini, 2013; Li, Valla and Garcia-Martinez, 2014b; Abate *et al.*, 2016; Hartmann, Machoke and Schwieger, 2016; Schwieger *et al.*, 2016). The enhanced activity, selectivity, and stability of hierarchical zeolites has often been attributed to reduced transport limitations and increased accessibility to active sites as a result of added meso- and macropores. However, despite the significant effort devoted to the design of new hierarchical zeolites (Pérez-Ramírez *et al.*, 2008; Lopez-Orozco *et al.*, 2011; Vernimmen, Meynen and Cool, 2011; Čejka *et al.*, 2012; Chen *et al.*, 2012; Moller and Bein, 2013; Valtchev *et al.*, 2013; Tsapatsis, 2014; Schwieger *et al.*, 2016), limited progress has been achieved for quantitatively establishing the link between the observed performance and the hierarchical structure (Christensen *et al.*, 2003; Liu *et al.*, 2011; X. Zhang *et al.*, 2012; Konno *et al.*, 2014; Gamliel *et al.*, 2018). Such quantitative connection between the structural characteristics and the catalytic behavior could lead to the rational design of improved catalysts.

Self-pillared pentasil (SPP) zeolite is a hierarchical zeolite formed by the repetitive rotational intergrowth of MFI nanosheets (X. Zhang *et al.*, 2012; Xu *et al.*, 2014; Swindlehurst *et al.*, 2015). It is possible to manipulate the nanosheet thickness, the mesopore size distribution and the particle size by variation of synthesis conditions. When the layer thickness of SPP is reduced down to a single-unit-cell (2 nm), up to 40% of the active sites is found to be on the external surface (X. Zhang *et al.*, 2012). Although a finer control of mesopore size and layer thickness uniformity can be achieved when rotational intergrowths occur in the presence of a designed surfactant (Shen *et al.*, 2018), here we use SPP due to its simpler synthesis, which (as we will demonstrate) allows facile manipulation of layer thickness in the 2-10 nm range.

Among the test reactions used to evaluate hierarchical zeolites (reviewed by Christensen *et al.* (Holm *et al.*, 2011) and Hartmann and Schwieger *et al.* (Hartmann, Machoke and Schwieger, 2016)), we chose benzyl alcohol self-etherification and alkylation with mesitylene. The alkylation reaction only occurs on the SPP external surface due to size exclusion of mesitylene (8.6 Å) from the MFI framework pores, while the etherification reaction can take place on both external surface and micropores. Therefore, the alkylation and etherification rates can provide a quantitative assessment of internal (within the micropores) and external (on the outside surface of the zeolite layers) catalytic activity (X. Zhang *et al.*, 2012; Liu *et al.*, 2014).

First, the kinetics of the two model reactions over SPP zeolites were investigated. The alkylation rate expression derived from the current study is different from the 1st order

one we have used in our earlier work (X. Zhang *et al.*, 2012; Liu *et al.*, 2014). The contributions to the observed etherification rate by the external surface and micropores were quantified. The effect of diffusion on the observed reaction rates (i.e., the presence of diffusion limitations) of the model reactions were determined to be insignificant at meso- and micro-pore levels in SPP zeolites under the investigated conditions. The key structural attribute, i.e., layer thickness of SPP, was correlated to the selectivity of etherification over alkylation. As a comparison, MCM-22 — a 10MR zeolite with MWW framework — was also used in the same analysis of model reactions to obtain the corresponding kinetic parameters. Significant differences in selectivity and external surface catalytic activity were found between MCM-22 and SPP zeolites.

5.2 Experimental methods

5.2.1 Synthesis of H-SPP zeolites with different layer thicknesses

Solution A was prepared by dissolving 0.100 g aluminum isopropoxide (Sigma-Aldrich) in 3.662 g tetra (n-butyl) phosphonium hydroxide solution (TBPOH, 40% by weight, Sigma-Aldrich). Solution B was prepared by adding 6.500 g TBPOH solution dropwise into 10.211 g tetraethyl orthosilicate (TEOS, Sigma-Aldrich) while stirring. Sodium hydroxide solution was prepared by dissolving 0.162 g sodium hydroxide in 4.485 g water. A clear solution was obtained by adding B to A, followed by the addition of the sodium hydroxide solution. The hydrolysis was carried out for 24 h at room temperature with stirring. A clear sol was obtained with the composition of 10 SiO_2 : 0.05 Al_2O_3 : 3

TBPOH : 0.125 NaOH : 100 H_2O : 40 EtOH. The sol was then transferred to a Teflon-lined stainless steel autoclave.

To prepare SPP with different layer thicknesses, we varied the hydrothermal synthesis temperature and time. The hydrothermal treatments for SPP-2, SPP-4 and SPP-8 were performed in a rotation oven at 388K for 7 days (SPP-2); 393K for 7 days (SPP-4); and at 423K for 2 days (SPP-8), respectively.

The product was washed with distilled water by repeated centrifugation and decanting of the supernatant, until the pH of the final supernatant was lower than 9. The final precipitate was dried at 343 K for 12 h, followed by calcination in air at 823 K for 12 h in a static furnace.

For ion exchange (to allow Na^+ in the framework to be exchanged by NH_4^+), the calcined zeolite was first mixed with distilled water to yield a 5% (by weight) suspension. The suspension was then heated at 343 K for 12 h and washed with distilled water by centrifugation and decanting of the supernatant, so that the pH of the supernatant was 6-7. The precipitate was then mixed with 1.0 mol L^{-1} ammonium nitrate solution to yield a 5% (by weight) suspension. The suspension was then heated at 353 K for 5 h and the solid was recovered with centrifugation. The treatment in ammonium nitrate solution was repeated three times, and the final product was washed with water, dried at 343 K and calcined in air at 823 K for 4 h in a static furnace.

5.2.2 Synthesis of H-MWW

H-MWW were synthesized as described earlier (Corma, Fornes, *et al.*, 1998; Maheshwari *et al.*, 2008).

5.2.3 Structure characterization

The morphology of SPP zeolites was determined by transmission electron microscopy (TEM). Typically, a TEM specimen was prepared by applying a few droplets of an aqueous suspension of the ion-exchanged zeolite product onto an ultra-thin carbon coated 400 mesh copper grid on lacey carbon support film (Ted Pella Inc.). All TEM images were obtained with a FEI Tecnai G^2 F30 TEM operating at 300 kV using a CCD camera.

5.2.4 Acid site characterization

Si/Al ratios of all zeolites used here were obtained through inductively coupled plasma optical emission spectroscopy (ICP-OES) analysis carried out by Galbraith Laboratories.

Brønsted acid site density was determined by Hoffman elimination of isopropylamine based on a reactive gas chromatography (RGC) technique as reported in (Abdelrahman *et al.*, 2017). The external Brønsted acid site density was measured by 2,6-di-tert-butylpyridine (dTBP) titration over ethanol dehydration following the procedure reported in (X. Zhang *et al.*, 2012).

The IR spectra of pyridine from self-supporting zeolite wafers of ca. 13 mg cm^{-2} were obtained using a Nicolet 6700 FTIR spectrometer. Prior to IR measurements, each zeolite wafer was activated under vacuum (10^{-4} Pa) at 450 °C for 2 h inside a home-built IR cell with CaF_2 windows. The wafer was then exposed to pyridine vapor of 1.3×10^3 Pa at 150

°C for 0.5 h, and evacuated (10^{-4} Pa) at 150 °C for 0.5 h to remove physisorbed molecules. Then, the IR spectra were recorded at temperatures up to 350 °C.

5.2.5 Liquid-phase reactions

Etherification and alkylation of benzyl alcohol were performed using the same set-up and procedures as described in (X. Zhang *et al.*, 2012). Specifically, 15 mL mesitylene were added into a three-necked round bottom flask (100 mL) with a desired amount of zeolite. The reactor was connected to a reflux condenser and heated in oil bath (343 K) under atmospheric pressure and stirring for 0.5 h (1″ stirring bar, 500 rpm stirring speed setting in Corning PC 620D hot plate stirrer). A desired amount of benzyl alcohol was injected using a steel needle through one side-neck to start the reaction. Around 0.1 mL of the reaction mixture was withdrawn at regular intervals using a steel needle through the side-neck and injected through a 0.2 μm filter into a 2 mL glass vial. The samples were periodically injected through an autosampler and analyzed in a gas chromatograph (Agilent HP-7890B GC) equipped with a methylsiloxane capillary column (HP-5, 30.0 m x 320 μm x 0.25 μm) connected to a flame ionization detector.

The initial rates were determined under different initial benzyl alcohol concentrations with conversion less than 10%. No side products were detected.

5.2.6 Experiment design and parameter estimation

Observed concentrations of benzyl alcohol, benzyl ether, 1,3,5-trimethyl-2-benzylbenze at different reaction time were collected under different experimental settings (e.g., different initial benzyl alcohol concentrations or zeolites with different characteristic

diffusion lengths) and were entered as multi-response data input. A set of nonlinear ordinary differential equations (ODEs) (i.e., the rate expressions of alkylation and etherification) were entered as the model equations. Parameters (kinetic parameters and diffusivity) were then optimized by integrating the ODEs using Athena Visual Studio v14.2 with Bayesian estimation solver.

5.3 Results and discussion

5.3.1 Active sites in SPP and MCM-22

Alkylation and etherification reactions of benzyl alcohol are Brønsted acid-catalyzed under liquid-phase reaction conditions, forming two products: 1,3,5-trimethyl-2-benzylbenzene and benzyl ether. No catalytic activity was detected when pure-silicate SPP, Sn-SPP or beta-alumina were used under the same reaction conditions. The formation of the alkylation product, 1,3,5-trimethyl-2-benzylbenzene, was found to be inhibited and eventually completely suppressed when an excess amount of 2,6-di-tert-butylpyridine (dTBP) was added in the reaction mixture (X. Zhang *et al.*, 2012). Since dTBP only deactivates Brønsted acid sites on the external surface of MFI (Corma, Fornés, *et al.*, 1998; Góra-Marek, Tarach and Choi, 2014; Wu *et al.*, 2016), it can be concluded that only the external Brønsted acid sites of SPP are accessible to catalyze the alkylation reaction.

SPP with different layer thicknesses (denoted as SPP-2, -4, and -8) and MCM-22 (a microporous zeolite with MWW framework and a thin plate-like crystal morphology)

were synthesized following the procedures described in section 5.2. The corresponding Si/Al ratios and total Brønsted acid site densities (BAS) are summarized in Table 5-1.

Table 5-1 Acidic properties and characteristic diffusion lengths of all catalysts

	Si/Al ratio[a]	Brønsted acid site density (BAS)[b], μmol/g	f_{ext} [c] (%)	x_p [d] (nm)
SPP-2	62	190	38 – 40	2 ± 1
SPP-4	60	190	25	3 ± 1
SPP-8	97	160	14	4.5 ± 1
0.2 μm MFI	32[e]	489[e]	2.8[e]	45 ± 6
1.4 μm MFI	30[e]	497[e]	2.3[e]	210 ± 60
17 μm MFI	28[e]	563[e]	0.09[e]	2,400 ± 500
MCM-22	22	520	8	-

[a]Determined by ICP-OES.
[b]Determined by Hoffman elimination of isopropylamine using reactive gas chromatography (RGC) technique (Abdelrahman *et al.*, 2017).
[c]f_{ext} = 1 – [(*rate of ethanol dehydration with excess dTBP*) / (*rate of ethanol dehydration without* dTBP)]
[d]The characteristic diffusion lengths (x_p) of (1) SPP zeolites and 1.4 μm MFI are defined as half-width of the layer thickness along *b*-axis, measured based on TEM images (see Figure 5-2 and Figure 5-4a); (2) 0.2 and 17 μm MFI are defined as the ratio of particle volume over external surface area, measured from SEM images in (Liu *et al.*, 2014).
[e]Results adapted from the supporting information in (X. Zhang *et al.*, 2012).

For SPP-8, which has a Si/Al ratio 97, the Brønsted acid density is ~160 μmol/g, suggesting that aluminum is mostly incorporated in the framework (the framework Si/Al ratio corresponding to the above Brønsted acid density is 103) with predominantly Brønsted acidity. However, for both SPP-2 and SPP-4, which have Si/Al ratios reduced to ~60, their Brønsted acid densities are around 190 μmol/g (with an equivalent Si/Al framework ratio of 86). If all aluminum was in the framework, the Brønsted acid density should have been 270 μmol/g, indicating that part of the aluminum in these samples is extraframework and does not contribute to the creation of Brønsted acid sites. Similar

discrepancy between the overall Si/Al ratio and Brønsted acid density is also found in MCM-22 (i.e., for the measured Si/Al ratio of 22, the Brønsted acid site density was found to be ~520 μmol/g, while it should have been ~725 μmol/g if all aluminum was in the framework). The presence of both Brønsted and Lewis acid sites in SPP-2 and MCM-22 were further confirmed through FTIR spectra using pyridine as a probe molecule (see Figure 5-1). When FTIR and the extinction coefficients cited in the literature (Emeis, 1993) were used to determine the Brønsted and Lewis acid concentrations of SPP-2 and MCM-22, much lower concentrations were obtained than those determined by Hoffman elimination of isopropylamine using RGC technique. Other studies have shown similar discrepancies and questioned the used extinction coefficients (Selli and Forni, 1999; Morterra, Magnacca and Bolis, 2001; Hemmann *et al.*, 2015; Harris *et al.*, 2016). For this reason, we only use the FTIR data in a qualitative manner to confirm that a significant fraction of acid sites in SPP-2 (Si/Al ratio ~ 60) are Lewis acid sites, and that the concentration of Brønsted acid sites is higher than that of Lewis acid sites. In the rest of this study, the Brønsted acid site density determined by Hoffman elimination of isopropylamine (or the equivalent Si/Al ratio) was used for the quantitative analysis.

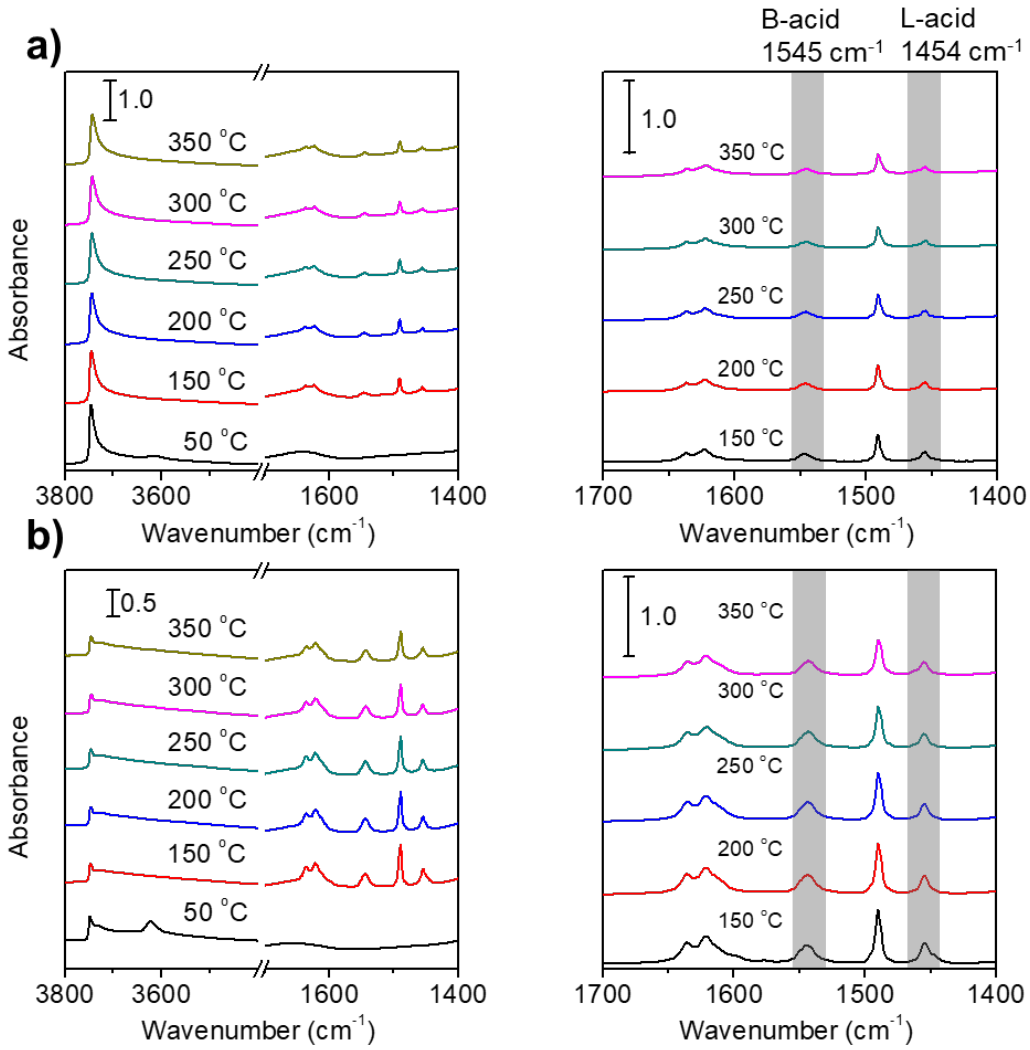

Figure 5-1 FTIR spectra of adsorbed pyridine on a) SPP-2 and b) MCM-22 after desorption at different temperatures. The bands at 1545 cm^{-1} and 1454 cm^{-1} (shaded areas) are assigned to pyridine interacting with Brønsted acid sites (PyH^+) and Py-Lewis species (PyL), respectively. Pyridine remained adsorbed on both acid sites up to 350 °C, and a decrease in the intensity of both bands is observed with the increasing desorption temperature.

The external acid site fraction (f_{ext}) is defined as the ratio of external Brønsted acid sites over total Brønsted acid sites, and is determined by measuring the ethanol dehydration

rate change when an excess of dTBP is introduced (X. Zhang *et al.*, 2012). In SPP zeolites, the layer thickness L_p can be measured from TEM images (see Figure 5-2).

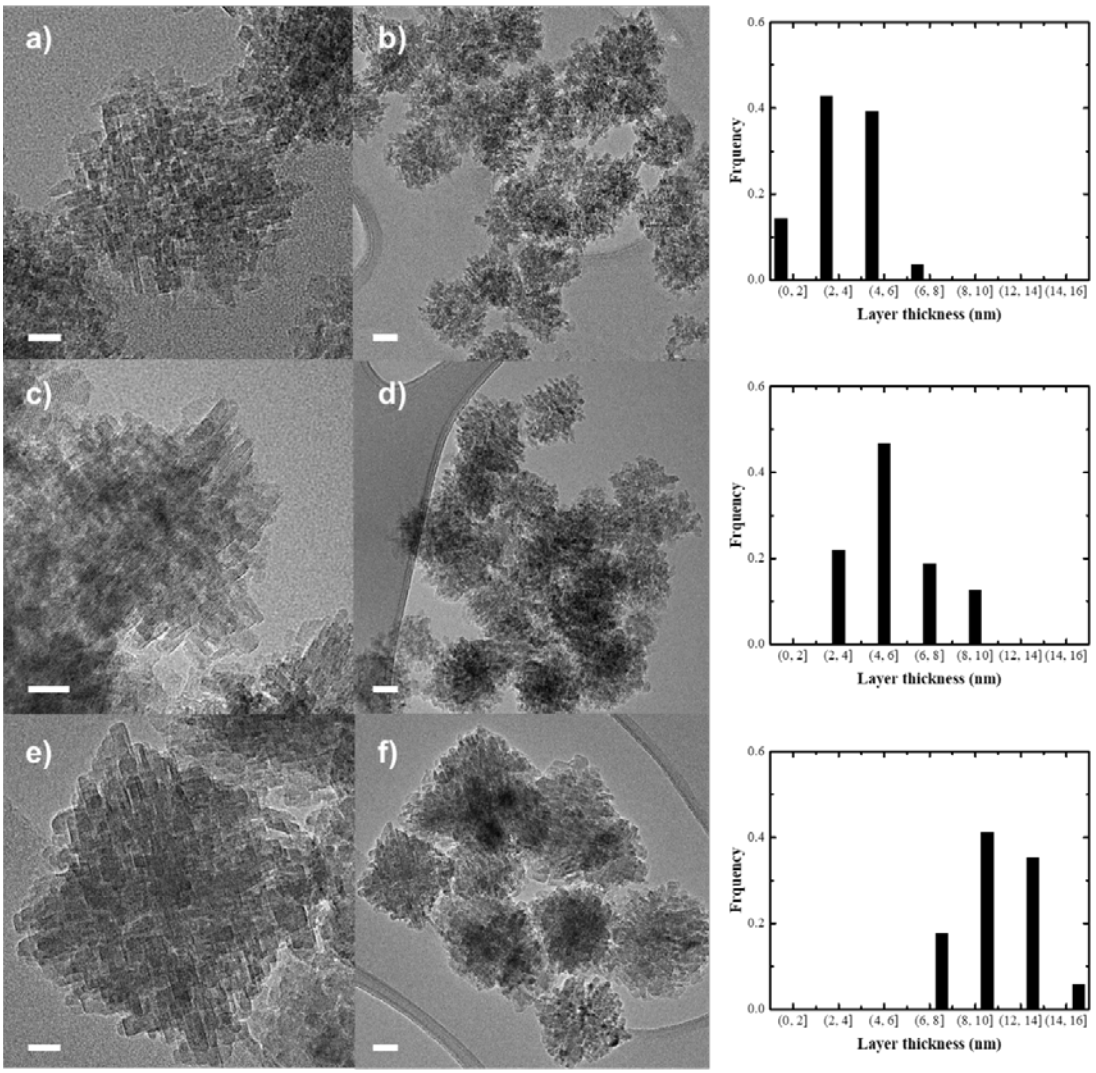

Figure 5-2 TEM images of SPP zeolites with different layer thicknesses and the corresponding layer thickness distribution: a, b) SPP-2; c, d) SPP-4; e, f) SPP-8. Scale bars for a, c, and e are 20 nm; for b, d, and f are 50 nm. Particles shown in a, c, and e are oriented down the *c*-axis of MFI.

Using the infinite slab model approximation, the characteristic diffusion length x_p can be defined as $L_p/2$, see Table 5-1. Figure 5-3 shows that the external acid site fraction of SPP

zeolites (determined by ethanol dehydration with and without dTBP) decreases with increasing characteristic diffusion length (determined by TEM). The variation of the measured external acid site fraction of SPP versus the different layer thicknesses can be described by the equation $f_{ext} = d/x_p$, where $d = 0.8 \pm 0.4$ nm. By assuming that the Brønsted acid sites are randomly distributed, d can be interpreted as the accessible depth from the outer surface of the nanosheet by dTBP (i.e., between a quarter and a half unit cell thick) based on the infinite slab approximation. Such a relationship will not hold as the particles get larger and acquire shapes for which the infinite slab model approximation is not valid; in this case the ratio of external Brønsted acid sites over total Brønsted acid sites cannot be inferred by SEM or TEM images but requires titration by ethanol dehydration with and without dTBP.

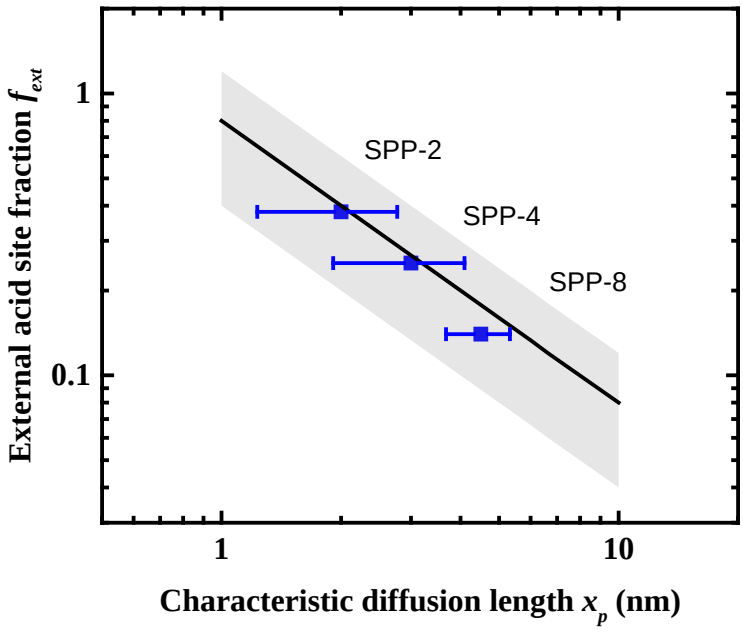

Figure 5-3 External acid site fractions of SPP zeolites determined by dTBP titration (square) as a function of the characteristic diffusion lengths. Characteristic diffusion length of SPP zeolites is defined as half-width of the layer thickness determined by TEM images. Error bars represent the standard deviation from the mean layer thickness measured from TEM images in Figure 5-2. The experimental data can be fitted by the equation $f_{ext} = d/x_p$ (solid line), where d = 0.8 ± 0.4 nm, i.e., the accessible thickness by dTBP (distance from the surface to the interior of the nanosheet for which sites located therein are accessible to dTBP) if Brønsted acid sites are randomly distributed.

In the current study, conventional MFI zeolites with nominal particle sizes of 0.2, 1.4 and 17 μm, i.e., the same microporous-only MFI zeolites used in our previous studies (X. Zhang *et al.*, 2012; Liu *et al.*, 2014), are also discussed. Considering the slab morphology of the 1.4 μm MFI zeolite (see SEM images in (Liu *et al.*, 2014) and TEM image in Figure 5-4a), its characteristic diffusion length can be approximated as half-width of the layer thickness along the *b*-axis. For the 0.2 and 17 μm MFI zeolites, which exhibit sphere-like and cubic morphologies (see SEM images in (Liu *et al.*, 2014) and TEM

image in Figure 5-4b), the characteristic diffusion lengths are defined as the ratio of particle volume over its external surface area. The characteristic diffusion lengths (x_p) of all conventional MFI zeolites calculated based on the above definitions are summarized in Table 5-1. The corresponding total Brønsted acid site density and external acid site fraction (determined by ethanol dehydration with and without dTBP) are the same as reported in (X. Zhang *et al.*, 2012; Liu *et al.*, 2014).

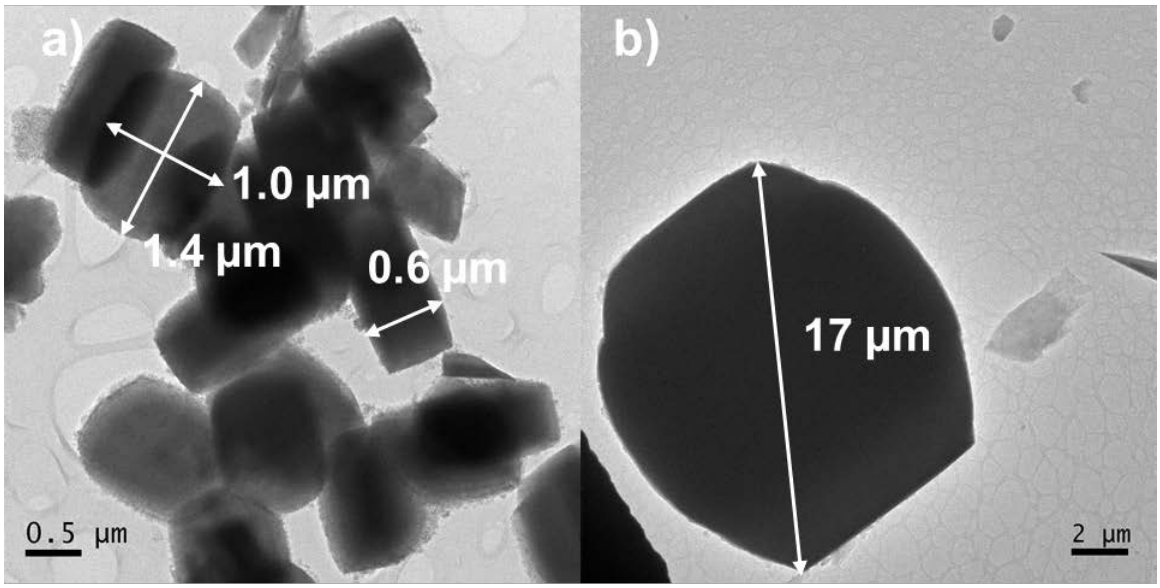

Figure 5-4 TEM images of conventional MFI zeolites: a) 1.4 µm; b) 17 µm.

5.3.2 Kinetics and mechanism of reactions

As reported earlier (X. Zhang *et al.*, 2012), the absence of external mass transfer effects on the measured reaction rate was accomplished by use of a high enough stirring rate. Moreover, as we have done earlier, we assume that the effect of microporous diffusion on the measured rate can be ignored in single unit cell SPP zeolites; and here we show that

this holds (for the reaction conditions studied) even up to 20 nm thick layers (i.e., x_p = $L_p/2$ = 10 nm, see Figure 5-5).

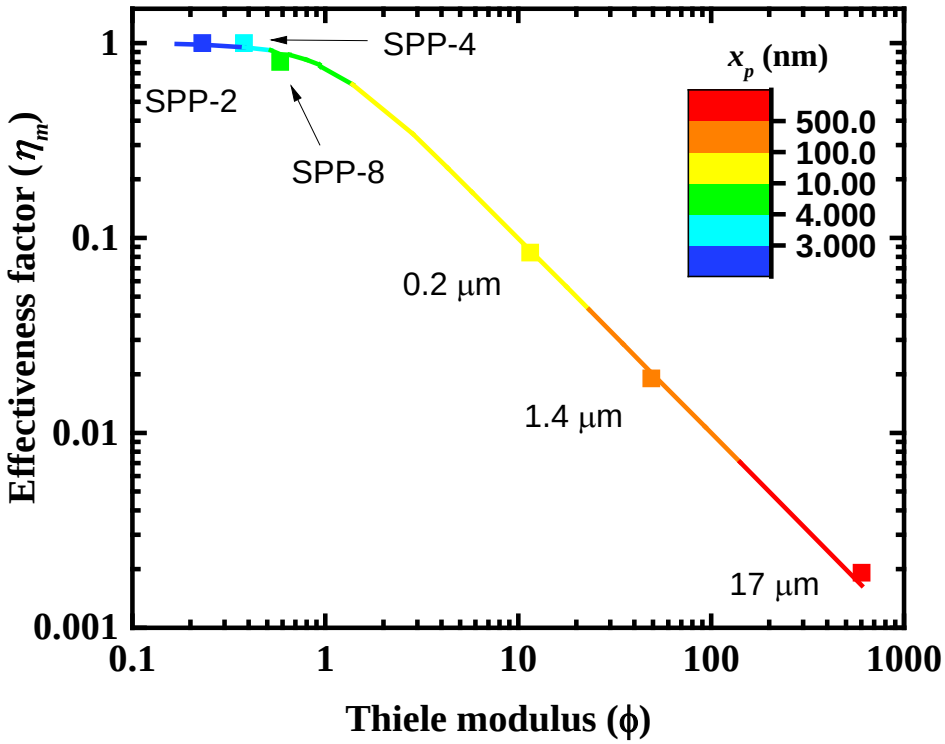

Figure 5-5 Effectiveness factor versus Thiele modulus plot. Experimental data: squares. Model prediction: solid line. The predicted effectiveness factor is calculated based on eq. 5-4, and Thiele modulus is determined by the Brønsted acid site density (BAS), external acid site fraction (f_{ext}) and characteristic diffusion lengths (x_p), shown in Table 5-1, and the effective etherification rate constant in micropores (k_{2int}) and diffusivity (D_{mA}), shown in Table 5-3. The characteristic diffusion lengths are indicated by the color map; the characteristic diffusion lengths of SPP-2, -4, -8 and 1.4 μm MFI zeolites are defined as half-width of the layer thickness along *b*-axis, while for the 0.2 and 17 μm MFI zeolites are defined as the ratio of particle volume over external surface area, based on the microcopy data in Figure 5-2, Figure 5-4 and ref. (Liu *et al.*, 2014).

We further assume and later validate (see the detailed discussion in 5.5.2) that the effect of mesopore transport on the measured rates can also be neglected. Therefore, under the

reaction conditions studied here, in SPP zeolites, the measured rates of alkylation and etherification are assumed to be intrinsic reaction rates. We use this assumption to develop rate expressions and then verify its validity in section 5.3.3.

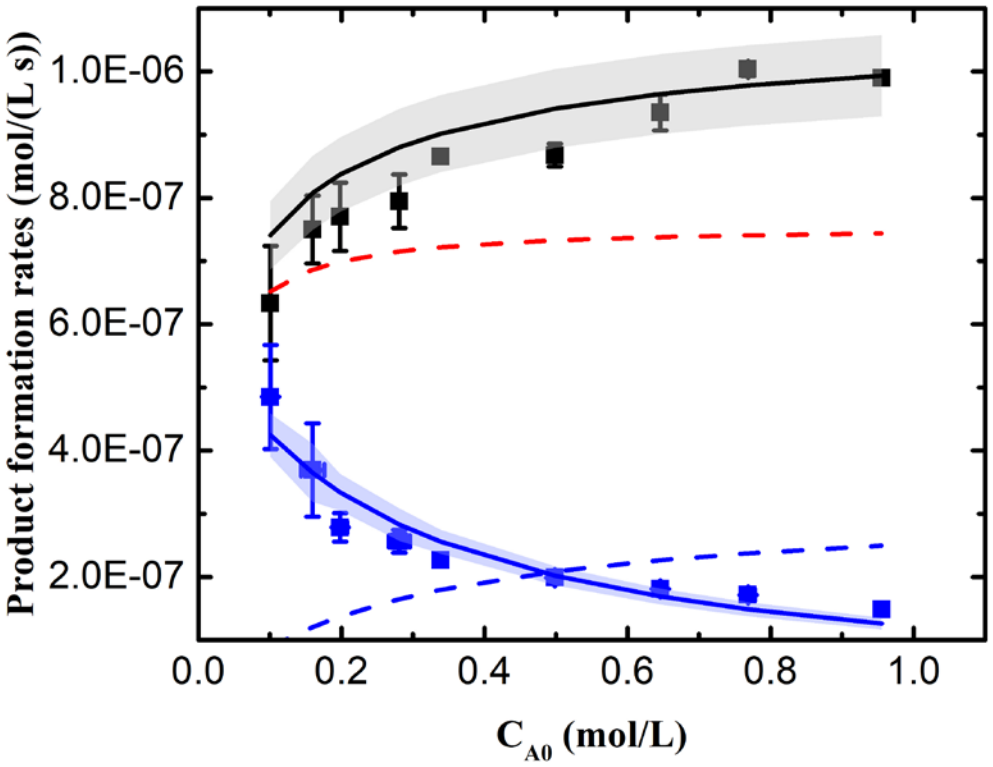

Figure 5-6 Initial rates of alkylation (blue squares) and etherification reactions (black squares) measured at different initial benzyl alcohol concentrations (C_{A0}) for catalyst SPP-2, and model prediction of alkylation reaction rates (eq. 5-1, blue solid line) and etherification reaction rates (eq. 5-3, black solid line) using the parameters given in Table 5-3. The shaded areas represent the error of the modeling parameters using 95% confidence intervals for the kinetic parameters. The blue and red dash lines represent the etherification rate contributions from external surface and micropores, respectively.

The formation rates of 1,3,5-trimethyl-2-benzylbenzene and benzyl ether were measured at different initial concentrations of benzyl alcohol (0.1 – 1.0 mol/L) over SPP-2 (see

Figure 5-6). For alkylation, a negative order dependence on benzyl alcohol concentration was observed within the investigated regime, while the etherification rates increased with increasing benzyl alcohol concentrations.

The kinetic dependency for alkylation reaction can be explained with the proposed mechanism shown in Scheme 5-1 (Narender *et al.*, 2006). In this mechanism, a benzyl alcohol (A) molecule initially adsorbs onto a Brønsted acid site and is protonated to form a carbonium ion (A'*). It may then react with a free or weakly adsorbed mesitylene (S) to form 1,3,5-trimethyl-2-benzylbenzene (P) as the rate-limiting step for alkylation reaction or may react with a second adsorbed benzyl alcohol to form benzyl ether (B) as the rate-limiting step for etherification reaction.

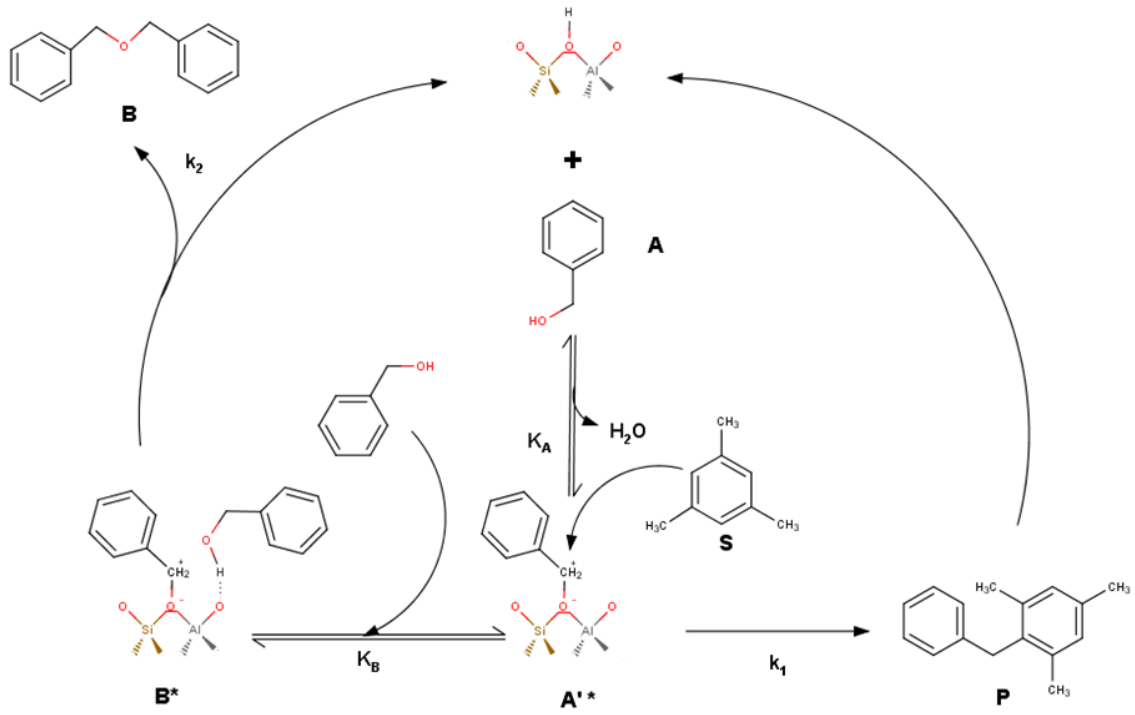

Scheme 5-1 Proposed mechanisms for benzyl alcohol etherification (left) and alkylation (right) reactions in liquid-phase on a zeolitic Brønsted acid site.

The kinetic rate expression for the alkylation reaction is shown in eq. 5-1 and can be derived from this mechanism by assuming 1) quasi-equilibrium is achieved for all adsorption steps and 2) the dominant surface species are the protonated benzyl alcohol (A'*) and the co-adsorbed benzyl alcohol (B*).

$$\frac{dC_P}{dt} = \frac{k_{1S}}{1 + K_B C_A} C_{H^+} f_{ext} \qquad 5\text{-}1$$

C_P and C_A denote the concentration of 1,3,5-trimethyl-2-benzylbenzene and benzyl alcohol, respectively. The kinetic parameter k_{1S} represents the effective rate constant associated with the alkylation step. Parameter K_B denotes the equilibrium constant for the

formation of co-adsorbed benzyl alcohol. C_{H^+} denotes the total Brønsted acid site concentration in the reactor ([mol H^+]/L) based on the amount of zeolite added and its Brønsted acid site content.

The kinetic rate expression for the etherification reaction on the external surface is shown in eq. 5-2.

$$\left(\frac{dC_B}{dt}\right)_{ext} = \frac{k_2 K_B C_A}{1+K_B C_A} C_{H^+} f_{ext} \qquad 5\text{-}2$$

C_B denotes the concentration of benzyl ether. The kinetic parameter k_2 represents the rate constant associated with the rate-limiting step for etherification on the external surface.

A detailed derivation of the alkylation and etherification rate expressions on the external surface could be found in 5.5.1.

The reaction rate for benzyl ether formed in the micropores is considered to be first-order with respect to the adsorbed benzyl alcohol concentration in micropores, as in our earlier study (X. Zhang *et al.*, 2012). Therefore, by summing up the external and micropore rate expressions, the overall kinetic rate expression for etherification reaction is shown in eq. 5-3.

$$\frac{dC_B}{dt} = \frac{k_2 K_B C_A}{1+K_B C_A} C_{H^+} f_{ext} + k_{2int} \overline{C_A} C_{H^+} (1-f_{ext}), \overline{C_A} = \frac{KC_A}{1+KC_A} \overline{C_A^{\max}} \qquad 5\text{-}3$$

The kinetic parameter k_{2int} represents the effective rate constant associated with the etherification reaction in micropores. $\overline{C_A}$ denotes the adsorbed concentration of benzyl

alcohol, determined by the Langmuir adsorption isotherm (X. Zhang *et al.*, 2012). The adsorption equilibrium constant K = 62 L/mol and the maximum adsorbed concentration of benzyl alcohol in the catalyst $\overline{C_A^{\max}}$ = 1.35 mol/L_{cat} were adopted from (X. Zhang *et al.*, 2012).

The four unknown parameters, k_{1S}, k_2, K_B, k_{2int}, in eqs. 5-1 and 5-3 were first estimated by assuming absence of diffusion limitations and fitting eqs. 5-1 and 5-3 to the time evolution of observed concentrations ($C_A(t)$, $C_B(t)$, $C_P(t)$) measured at different benzyl alcohol initial concentrations using the SPP-2 catalyst. The estimation results are given in Table 5-2.

Table 5-2 Estimated parameters of alkylation and etherification using data from SPP-2 only, and assuming absence of diffusion limitations.

Parameters	Estimated value
k_{1S} (/s)	0.002 $\pm$ 0.0001
k_2 (/s)	0.0026 $\pm$ 0.0002
K_B (L/mol)	2.7 $\pm$ 0.3
k_{2int} (L_{cat}/ (mol s))	0.0011 $\pm$ 0.00006

To include the effect of micropore diffusion as the microporous diffusion length increases, eq. 5-3 was modified to include the effectiveness factor and obtained eq. 5-4.

$$\frac{dC_B}{dt} = \frac{k_2 K_B C_A}{1+K_B C_A} C_{H^+} f_{ext} + \eta_m \left(k_{2int} \overline{C_A} C_{H^+} (1 - f_{ext}) \right),$$
$$\overline{C_A} = \frac{KC_A}{1+KC_A} \overline{C_A^{\max}}, \eta_m = \frac{\tanh(\phi)}{\phi}, \phi = x_p \sqrt{2k_{2int} C_{H^+,int} / D_{mA}} \qquad 5\text{-}4$$

The diffusivity (D_{mA}) represents the effective diffusion coefficient of benzyl alcohol in micropores. The effectiveness factor η_m is derived based on the first order etherification reaction in micropores, with Φ as the Thiele modulus and x_p as the characteristic diffusion length. $C_{H^+,int}$ denotes the moles of Brønsted acid sites inside the catalyst ([mol H^+]/L_{cat}), i.e., $C_{H^+,int} = BAS(1-f_{ext})\rho_{zeolite}$, with the Brønsted acid site density (BAS) and external acid site fraction (f_{ext}) given in Table 5-1 and zeolite density ($\rho_{zeolite}$) of 1,800 g/L_{cat}.

The fifth parameter, micropore diffusivity D_{mA}, was estimated by using diffusion limited data from large particles (i.e., conventional MFI zeolites with particle sizes of 0.2, 1.4 and 17 μm). Additional data sets were also collected to get a more accurate estimation of the external and internal etherification kinetic parameters (k_2 and k_{2int}) by adjusting the rate contributions from external surface and micropores using SPP zeolites with various external acid site fractions (i.e. SPP-4 and SPP-8 that have different layer thicknesses from SPP-2). The initial estimations of k_{1S}, k_2, K_B, k_{2int} obtained from the SPP-2 data (shown in Table 5-2) were then refined by fitting the time evolution of observed concentrations ($C_A(t)$, $C_B(t)$, $C_P(t)$) measured over MFI zeolites with different characteristic diffusion lengths under the same initial benzyl alcohol concentration of 0.17 mol/L. The four kinetic parameters, k_{1S}, k_2, K_B, k_{2int}, and micropore diffusivity D_{mA} obtained by the procedure are given in Table 5-3. The comparison between the modeling results and the measured rates are shown in Figure 5-6 (different initial concentrations of benzyl alcohol) and Figure 5-7 (catalysts with different characteristic diffusion lengths).

The parity plot with all experimental data used in the fitting indicates that the proposed kinetic model is capable of describing the measured concentrations (see Figure 5-8).

Table 5-3 Estimated parameters of alkylation and etherification over SPP and conventional MFI zeolites

Parameters	Estimated value
k_{1S} (/s)	0.0025 ± 0.0001
k_2 (/s)	0.0013 ± 0.00005
K_B (L/mol)	3.9 ± 0.1
k_{2int} (L_{cat}/ (mol s))	0.0014 ± 0.0001
D_{mA} (m^2/s)	(4.4 ± 1.2) x 10^{-20}

The derived model can also be used to dissect the overall etherification rate into its parts contributed by external surface and micropores. As shown in Figure 5-6, despite the 40% external acid site fraction of SPP-2, the overall etherification rate is dominated by the contribution from micropores under the investigated reaction conditions. The significantly higher etherification rates in micropores can be attributed to the high loading of benzyl alcohol in MFI micropores due to physisorption.

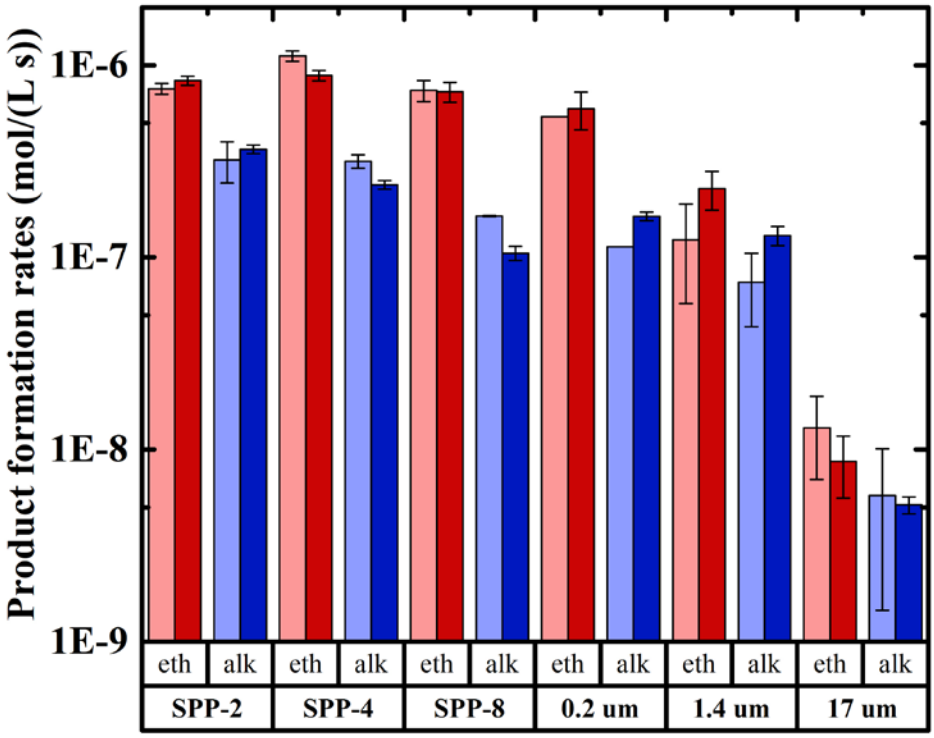

Figure 5-7 Initial rates of alkylation (light blue) and etherification (light red) measured over zeolites with different characteristic diffusion lengths, and corresponding modeling results of the alkylation (dark blue) and etherification rates (dark red) obtained using the parameters shown in Table 5-3. The error bars in the modeling results correspond to 95% confidence intervals for the parameters. The error bars in measured rates were determined by independent experiments. Note that in some cases the error bars are too small to be visible on the graph.

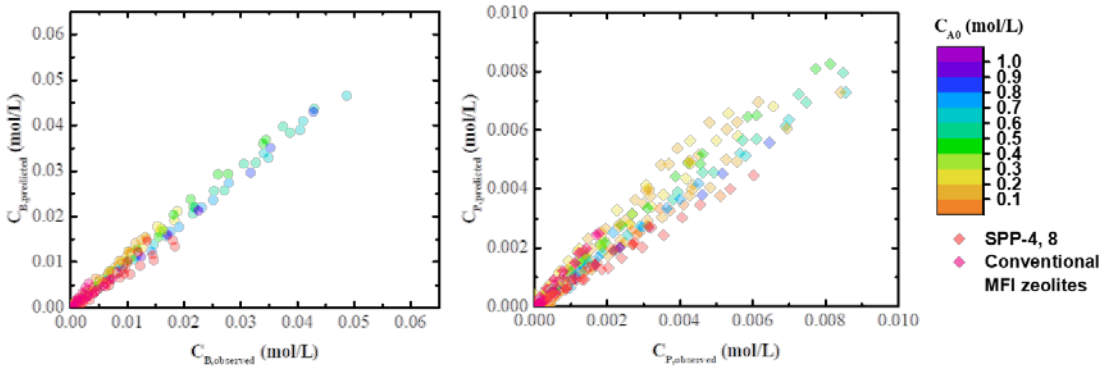

Figure 5-8 Parity plots with concentrations of benzyl ether (left) and 1,3,5-trimethyl-2-benzylbenzene (right) predicted by the mathematical model *vs* the experimental ones. The experiments using different initial benzyl alcohol concentrations are indicated by the color map to the right. The color codes for SPP with thicker layers and conventional MFI zeolites are also included with the symbols indicated to the right below the color-coded map.

5.3.3 Diffusion in SPP zeolites

The estimated diffusivity of benzyl alcohol in MFI micropores ($(4.4 \pm 1.2) \times 10^{-20}$ m^2/s) is close to the value reported in our earlier study (6.15×10^{-20} m^2/s) (X. Zhang *et al.*, 2012). The effectiveness factor that was calculated based on eq. 5-4 agrees well with the experimental data, as shown in Figure 5-5. For SPP zeolites with a set Si/Al ratio, considering that f_{ext} can be expressed as a function of x_p (as shown in Figure 5-3 and discussed in 5.3.1), the Thiele modulus of SPP zeolites is fully determined by x_p. Therefore, it can be concluded that SPP zeolites with Si/Al ratios larger than 75 and with layer thickness less than 20 nm (i.e., $x_p < 10$ nm, $\Phi < 1$) have effectiveness factors (for benzyl alcohol etherification at the conditions studied) close to 1, confirming that the etherification reaction rate measured in SPP-2, -4 and -8 is the intrinsic rate. The

effectiveness factor drops as the Thiele modulus increases, indicating that strong diffusion effects exist in all three conventional MFI zeolites.

The effectiveness factor for the reactions in SPP mesopores can also be calculated based on the estimated kinetic parameters and the diffusivity of benzyl alcohol in mesitylene. According to the analysis in 5.5.2, even for a diffusivity that is 5 orders of magnitude smaller than the reported diffusivity of benzyl alcohol in toluene (Chiu *et al.*, 2004), the effectiveness factor for mesopore reactions is close to 1. Therefore, the assumption of neglecting the mesopore transport effect on the reaction rates in SPP zeolites is also validated.

5.3.4 Selectivity

Selectivity is defined here as the etherification rate over alkylation rate. The expression of selectivity derived from eqs. 5-1 and 5-4 is given in eq. 5-5.

$$S_{B/P} \sim \left(\frac{k_2 K_B}{k_{1S}}\right) C_{A0} + \left(\frac{k_{2int}}{k_{1S}}\right)\left(\frac{KC_{A0}}{1+KC_{A0}}\overline{C_A^{\max}}\right)\left(1+K_B C_{A0}\right)\left(\frac{1}{f_{ext}}-1\right)\eta_m,$$
$$\eta_m = \frac{\tanh(\phi)}{\phi}, \phi = x_p\sqrt{2k_{2int}C_{H^+,int}/D_{mA}} \qquad 5\text{-}5$$

As shown in eq. 5-5, the contribution to the selectivity of benzyl ether consists of two parts: external surface and micropores. In this expression, only the external acid site fraction (f_{ext}) and the effectiveness factor (η_m) depend on the MFI particle size, shape and hierarchical structure, as shown in Figure 5-3 and Figure 5-5. Replacing all the kinetic parameters with the values in Table 5-3 and keeping the initial benzyl alcohol concentration at 0.17 mol/L, the selectivity expression could be rewritten as:

$$S_{B/P} \sim 0.36 + 1.21 \times \left(\frac{1}{f_{ext}} - 1 \right) \eta_m,$$
$$\eta_m = \frac{\tanh(\phi)}{\phi}, \phi = 14.8 \left(x_p / nm \right) \sqrt{C_{H^+,int}} \qquad 5\text{-}6$$

In Figure 5-9, the selectivity of SPP with different layer thicknesses and conventional MFI zeolites is plotted against the hierarchical-structure related term $\left(\frac{1}{f_{ext}} - 1 \right) \eta_m$ and compared with the model prediction based on eq. 5-6. In the reaction-controlled regime, for which the effectiveness factors are close to 1, the selectivity of SPP zeolites increases with the decrease of the external acid site fraction (i.e., by increasing the layer thickness). In the micropore diffusion-controlled regime (for MFI catalysts other than SPP), the effectiveness factor decreases as the characteristic diffusion length increases. Although the external active site fraction drops as the particles get larger and, consequently, along with it alkylation and external etherification rates drop, the internal etherification rate also drops due to the onset of diffusion limitations. Therefore, the selectivity in a conventional MFI zeolite (x_p > 10 nm) is determined by the competition between the increasing term $\left(\frac{1}{f_{ext}} - 1 \right)$ and the decreasing effectiveness factor, η_m. The maximum selectivity to benzyl ether is obtained in the reaction-controlled regime with catalyst that has a minimum external acid site fraction, i.e., a characteristic diffusion length of 10 nm for SPP zeolites.

At the reaction conditions used here and for any MFI zeolite with $\Phi < 1$ (i.e., η_m close to 1), with a measured selectivity of alkylation and etherification reaction at initial benzyl alcohol concentration around 0.17 mol/L, eq. 5-6 can be used to determine the external acid site fraction.

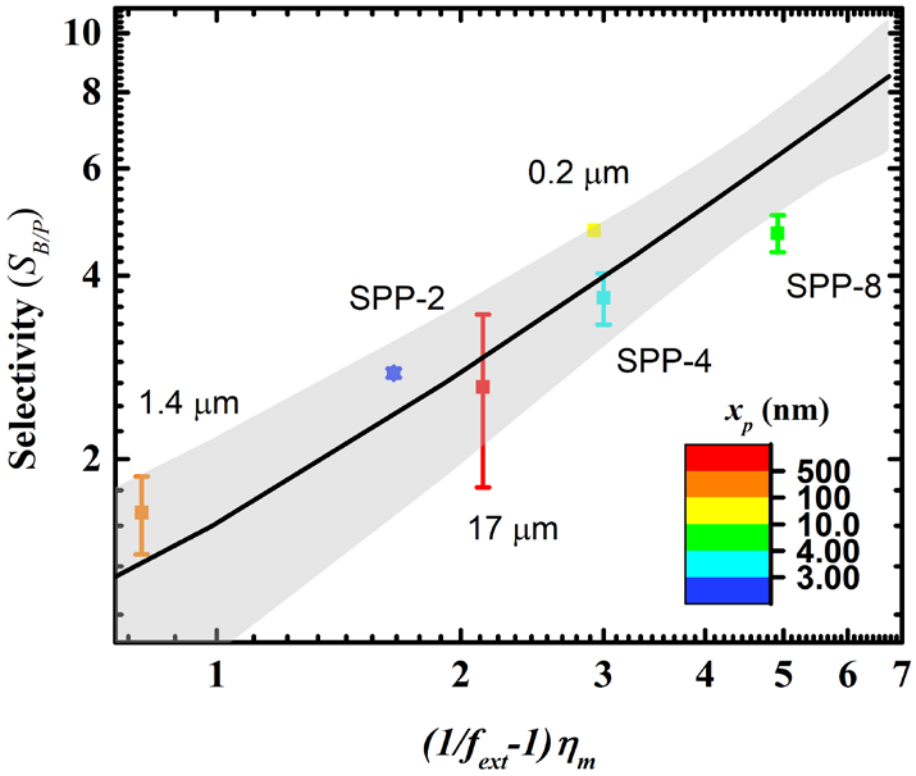

Figure 5-9 Selectivity as a function of the external acid site fraction (f_{ext}) and the effectiveness factor (η_m). The black line indicates the modeling results using eq. 5-6 (which is eq. 5-5 with the kinetic parameters reported in Table 5-3). The grey region represents the selectivity error of modeling corresponding to 95% confidence intervals for the parameters. Experimental data are shown as square points with error bars determined by independent experiments. The characteristic diffusion lengths are also indicated by the same color map as used in Figure 5-5.

5.3.5 Effect of external surface structure

Having determined by the above analysis the external rates of both alkylation and etherification reactions for MFI, we can further compare them with the corresponding rates for other catalysts. An important catalyst with external surface structure distinct from that of MFI is MWW (Leonowicz *et al.*, 1994; Corma, Martínez-Soria and Schnoeveld, 2000). MWW has a plate-like shape with its basal plane perpendicular to its *c*-axis. It is also a 10MR zeolite framework with parallel, uniform tubular pores normal to *c*-axis (running along its basal plane), but also contains characteristic 12MR semi-cups on its external (001) surface. The typical plate-like morphology of MCM-22 is shown in Figure 5-10.

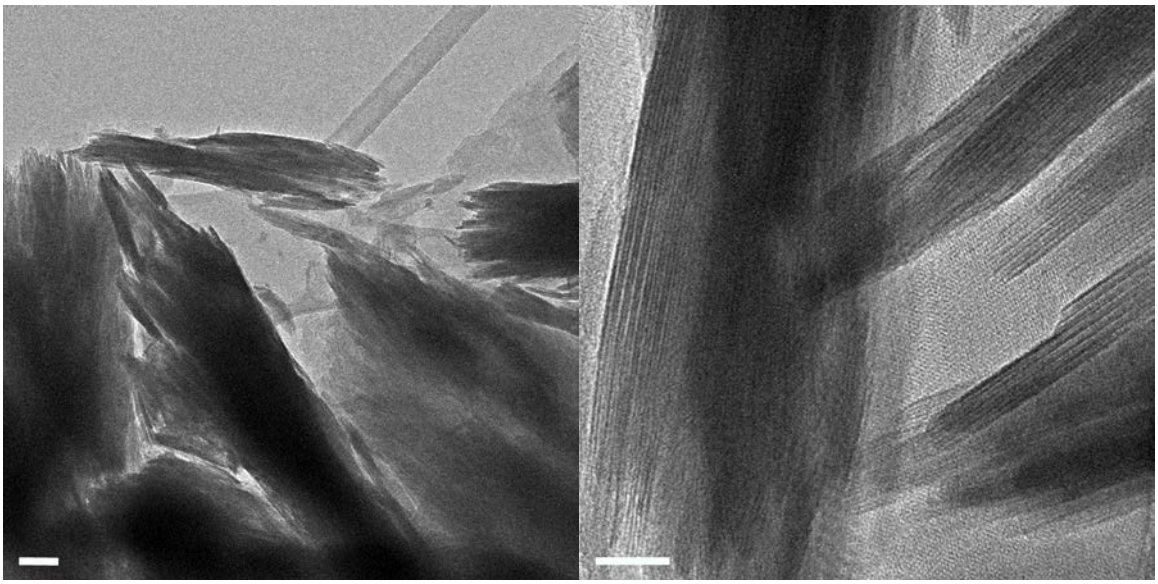

Figure 5-10 TEM images of MCM-22 at low magnification (left, scale bar 100 nm) and high magnification (right, scale bar 20 nm).

MCM-22 can also catalyze the alkylation and etherification reactions under the same reaction conditions. However, in the presence of an excess amount of dTBP, no product was detected suggesting only external catalytic activity. The Brønsted acid sites inside the micropores of MCM-22 do not contribute to alkylation and etherification reactions, as the pore opening (4.1 x 5.1 Å) is smaller than the kinetic diameter of benzyl alcohol (5.8 Å) and the characteristic diffusion length along the basal plane (*a*-axis) is >100nm.

By comparison to SPP, where etherification rate is dominated by the contribution from micropores, MCM-22, where only external surface contributes, is expected to be more selective to the alkylation product (i.e., smaller selectivity as defined in eq. 5-5). To confirm this prediction, the alkylation and etherification rates were measured over MCM-22 at different benzyl alcohol initial concentrations (0.02 – 0.8 mol/L). The alkylation and etherification reaction rates showed similar kinetic dependencies on the benzyl alcohol concentrations in MCM-22 as in SPP (see Figure 5-11). Thus, eqs. 5-1 and 5-2 that were used on SPP external surface were adopted to fit the experimental rates over MCM-22 and the estimation results of the external kinetic parameters — k_{1S}, k_2, K_B, — are given in Table 5-4. The selectivity over MCM-22 was found to be ~0.3 compared to ~3 in SPP (with initial benzyl alcohol concentration around 0.17 mol/L).

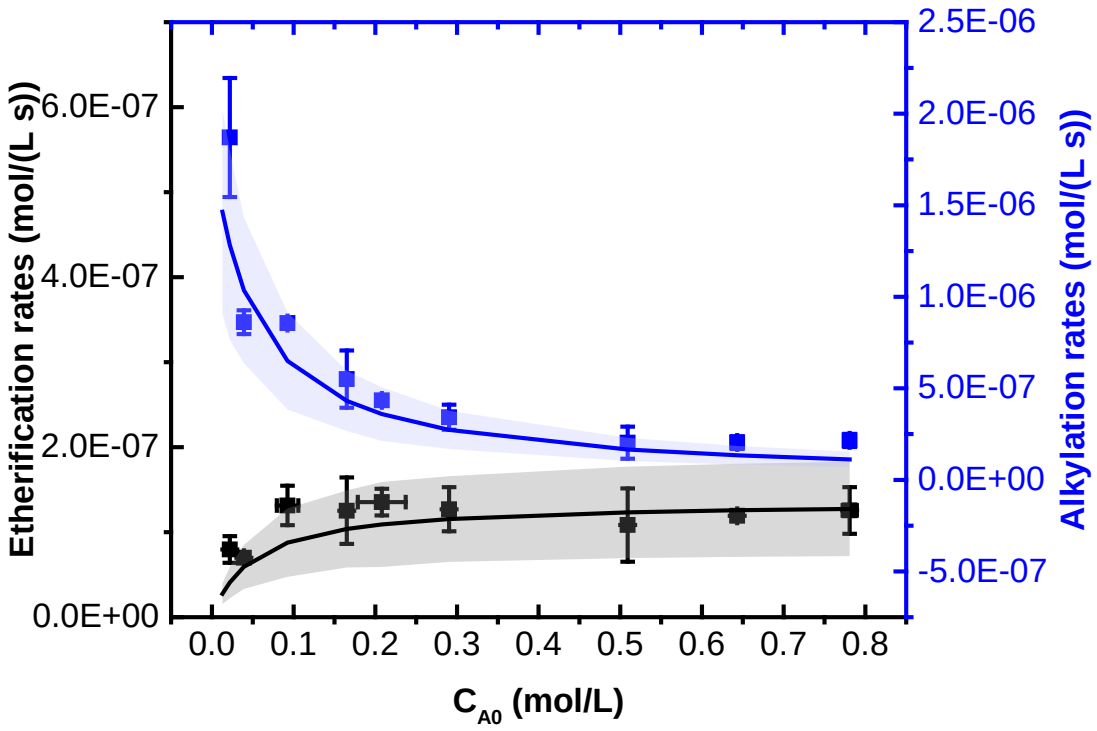

Figure 5-11 Initial rates of alkylation (blue squares) and etherification reactions (black squares) measured at different initial benzyl alcohol concentrations (C_{A0}) over MCM-22. The modeling results of alkylation reaction rates (blue solid line) and etherification reaction rates (black solid line) are also plotted as a function of initial benzyl alcohol concentrations using the parameters summarized in Table 5-4. The shaded areas represent the error of the modeling results, as a propagation of the 95% confidence intervals from the kinetic parameters.

A further comparison between the external kinetic parameters of MCM-22 and SPP is shown in Figure 5-12. An over 10 times higher alkylation rate constant and an over 5 times higher equilibrium constant for the formation co-adsorbed benzyl alcohol were found in MCM-22. In SPP zeolites, the external surface comprises of 10 MR open pore mouths of MFI (5.5 Å) and contains a high fraction of surface Si-OH; while in MCM-22, the external surface is covered by 12 MR semi-cups of MWW (7.1 Å) and contains

relatively few Si-OH (i.e., it is more zeolite-like). Given the relatively large size of 1,3,5-trimethyl-2-benzylbenzene and benzyl alcohol, the 12 MR cups on MCM-22 surface may better accommodate and stabilize the bulky transition state of alkylation reaction and the co-adsorbed benzyl alcohol, leading to the increased alkylation rate constant and equilibrium constant as estimated from measured rates. Similar catalytic performances in MWW zeolites were also observed in ethylbenzene and cumene production (Corma, Martínez-Soria and Schnoeveld, 2000; Perego and Ingallina, 2002).

Table 5-4 Estimated parameters of alkylation and etherification over MCM-22

Parameters	Estimated value
k_{1S} (/s)	0.034 ± 0.008
k_2 (/s)	0.0025 ± 0.0001
K_B (L/mol)	20 ± 6

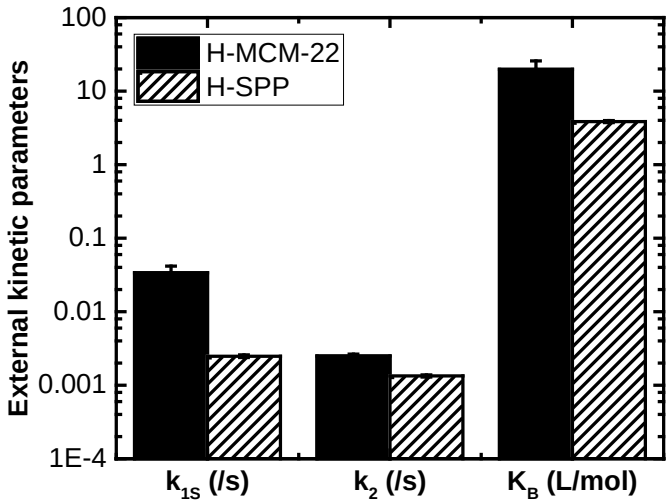

Figure 5-12 Comparison of alkylation and etherification reaction rate parameters for MCM-22 vs SPP. k_{1S}: effective alkylation rate constant; k_2: external etherification rate constant; K_B: external equilibrium constant for the formation of co-adsorbed benzyl alcohol. (For numerical values see Table 5-3 and Table 5-4)

5.4 Conclusions

Benzyl alcohol etherification reaction in SPP follows different kinetics on its external surface and in micropores. The overall etherification rate of SPP is dominated by the rate contribution in MFI micropores. Selectivity of etherification over alkylation was found to increase with the SPP layer thickness in the absence of micropore diffusion resistance. Maximum selectivity to benzyl ether can be found at the characteristic diffusion length of 10 nm, which provides the lowest external acid fraction while still ensuring the absence of diffusion limitations. Mesopore resistance was found not to play a role in the present study.

MCM-22 was shown to be a more selective catalyst to alkylation reaction, possibly due to its inaccessible active sites in the micropores. Higher alkylation reactivity was also found in MCM-22 external surface, showing over 10 times higher alkylation rate constant compared to that in SPP external surface. The cause of the increased alkylation rate constant (as well as the increased equilibrium constant for the formation co-adsorbed benzyl alcohol) can be attributed to the surface topological difference between MFI and MWW frameworks.

5.5 Supplementary information

5.5.1 Derivation of rate expressions for alkylation and etherification reactions over SPP external surface and MCM-22

According to the proposed mechanism, the following elementary steps for alkylation and etherification are proposed (symbols are the same as in Scheme 5-1, and * represents external Brønsted acid site).

$$A + * \underset{}{\overset{K_A}{\rightleftharpoons}} A'* + H_2O$$

$$A + A'* \underset{}{\overset{K_B}{\rightleftharpoons}} B*$$

$$B* \xrightarrow{k_2} B + *$$

$$A'* + S \xrightarrow{k_1} P + *$$

Assuming quasi-equilibrium for the adsorption of the first (K_A) and the second benzyl alcohol (K_B), the formation rate of benzyl ether is proportional to the concentration of co-adsorbed benzyl alcohol (C_{B*}) and the alkylation rate is proportional to the concentration of protonated benzyl alcohol ($C_{A'*}$). The concentration of mesitylene (C_S) is considered constant during the investigated time frame due to its large excess. Therefore, the effective alkylation rate constant (k_{1S}) is a product of the intrinsic alkylation rate constant (k_1) and mesitylene concentration (C_S):

$$\frac{dC_B}{dt} = k_2 C_{B*} \qquad 5\text{-}7$$

$$\frac{dC_P}{dt} = \left(k_1 C_S\right) C_{A'*} = k_{1S} C_{A'*} \qquad 5\text{-}8$$

The concentrations of co-adsorbed benzyl alcohol and protonated benzyl alcohol can be written in terms of benzyl alcohol concentration (C_A) and external Brønsted acid site concentration (C_*) using the equilibrium constants below:

$$K_A = \frac{C_{A'*}}{C_A C_*}; K_B = \frac{C_{B*}}{C_A C_{A'*}} \quad 5\text{-}9$$

According to the external Brønsted acid site balance:

$$C_{H^+,ext} = C_* + C_{B*} + C_{A'*} \quad 5\text{-}10$$

From 5-10 and 5-9, we obtain:

$$C_* = \frac{1}{1 + K_A C_A + K_B K_A C_A^{\ 2}} C_{H^+,ext} \quad 5\text{-}11$$

5-7 and 5-8 then become:

$$\frac{dC_B}{dt} = \frac{k_2 K_B K_A C_A^{\ 2}}{1 + K_A C_A + K_B K_A C_A^{\ 2}} C_{H^+,ext} \quad 5\text{-}12$$

$$\frac{dC_P}{dt} = \frac{k_{1S} K_A C_A}{1 + K_A C_A + K_B K_A C_A^{\ 2}} C_{H^+,ext} \quad 5\text{-}13$$

Further assuming that C_* can be neglected by comparing to C_{B*} and C_{A*} (i.e., $1 + K_A C_A + K_B K_A C_A^{\ 2} \approx K_A C_A + K_B K_A C_A^{\ 2}$) at high benzyl alcohol initial concentrations (0.1 ~ 1.0 mol/L), we obtain:

$$\frac{dC_B}{dt} = \frac{k_2 K_B C_A}{1 + K_B C_A} C_{H^+,ext} \quad 5\text{-}14$$

$$\frac{dC_P}{dt} = \frac{k_{1S}}{1 + K_B C_A} C_{H^+,ext} \quad 5\text{-}15$$

5-14 and 5-15 are used as the rate expressions for alkylation and etherification reactions (eqs. 5-2 and 5-1, respectively) over the external surfaces of SPP and MCM-22.

We use this simplification throughout the manuscript. To validate the above simplification of the rate expressions, the K_A over SPP zeolites was determined by fitting

the alkylation and etherification rates with low benzyl alcohol initial concentrations (< 0.1 mol/L) using the non-simplified eqs. 5-12 and 5-13, as the external rate expressions. With the parameters k_{1S}, k_2, K_B, k_{2int} fixed to the values summarized in Table 5-3 (determined using the simplified expressions), K_A is estimated to be 50 $\pm$ 15 L/mol. The comparison between the measured rates and modeling results based on the full external rate expressions from eqs. 5-12 and 5-13 are shown in Figure 5-13. For concentrations that are larger than 0.1 the full (Figure 5-13) and simplified (Figure 5-6) models are in good agreement. Therefore, according to the estimated value of K_A, the Brønsted acid site concentration can be neglected at the investigated initial concentration range of 0.1 to 1.0 mol/L.

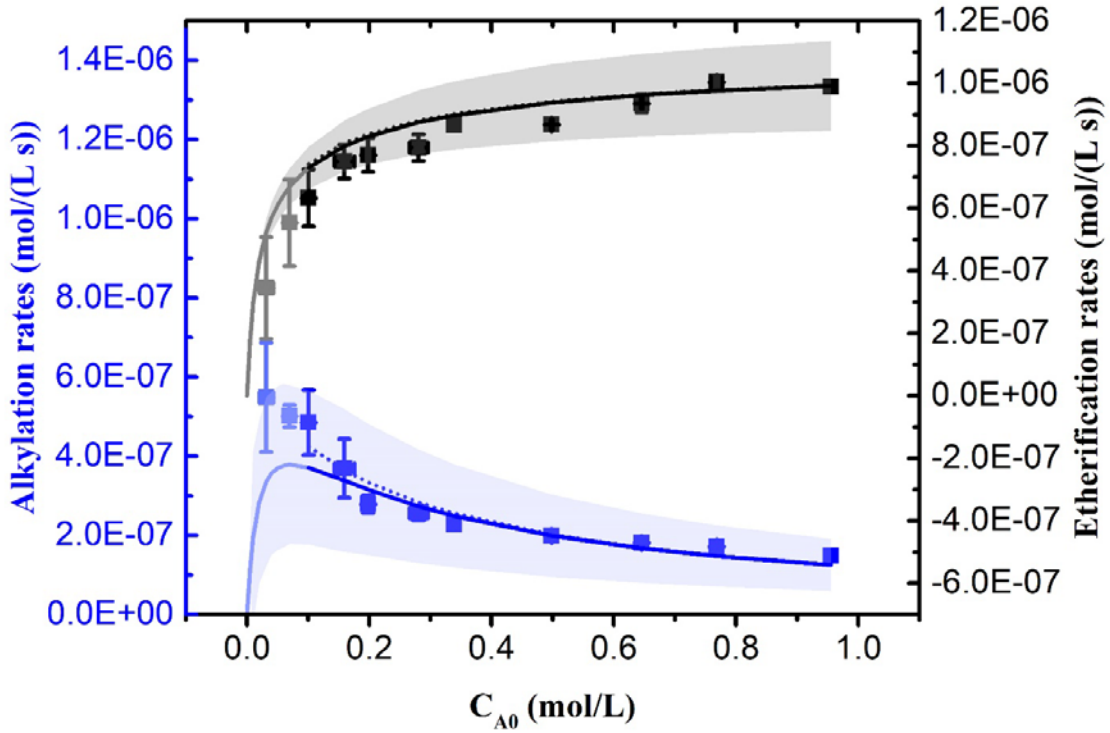

Figure 5-13 Initial rates of alkylation (dark and light blue: light blue are data not included in Figure 5-6) and etherification (black and grey: grey are data not included in Figure 5-6) reactions measured at different initial benzyl alcohol concentrations (C_{A0}) for catalyst SPP-2. Model predictions based on the full external rate expressions in eqs. 5-12 and 5-13 (solid lines) are compared with those based on the simplified rate expressions in eqs. 5-14 and 5-15 (dot lines, the same as shown in Figure 5-6). The shaded areas represent the error of the modeling results, as a propagation of the 95% confidence intervals from the kinetic parameters (including K_A).

5.5.2 Evaluation of mesopore resistance in SPP

When considering the mesopore diffusion, the characteristic diffusion length is the particle radius of SPP zeolites. Depending on synthesis time and conditions, SPP particle diameter could vary from 50 nm to over 400 nm. In this study, we fitted the kinetic parameters to the experimental data based on the assumption that no mesopore resistance

exists. Here, we will validate our assumption by calculating the required mesopore diffusivity of benzyl alcohol for the mesopore effectiveness factor to be ~1, and then compare it with the reported diffusivity of benzyl alcohol in toluene.

The material balance of benzyl alcohol (A) using Fick's Law for mesopore transport in the SPP sphere particle (particle radius R_p) is:

$$D_A^e\left(\frac{d^2C_A}{dR^2}+\frac{2}{R}\frac{dC_A}{dR}\right)=-r_A \qquad 5\text{-}16$$

in which $D_A^e=\frac{\varepsilon_p}{\tau}D_A, -r_A=r_P+2r_B=f\left(C_A\right)$

with boundary conditions: 5-17

$$\begin{cases} C_A=C_{AS} \text{ at } R=R_P \\ \dfrac{dC_A}{dR}=0 \text{ at } R=0 \end{cases}$$

r_A represents the consumption rate of benzyl alcohol, while r_P and r_B represent the alkylation and etherification rates, respectively. D_A^e represents the effective diffusion coefficient of benzyl alcohol in SPP particles. C_{AS} represents the concentration of benzyl alcohol on the particle surface. According to eqs. 5-1, 5-3, r_P and r_B are functions of C_A and 5-16, 5-17 could be made dimensionless:

$$\left(\frac{d^2\varphi}{d\omega^2}+\frac{2}{\omega}\frac{d\varphi}{d\omega}\right)=\phi^2F\left(\varphi\right) \qquad 5\text{-}18$$

in which $\varphi=\frac{C_A}{C_{AS}}, \omega=\frac{R}{R_P}, \phi^2=\left(\frac{R_P^2}{D_A^e}\right)\frac{f\left(C_{AS}\right)}{C_{AS}}, F\left(\varphi\right)=\frac{f\left(\varphi C_{AS}\right)}{f\left(C_{AS}\right)},$

with boundary conditions:

$$\begin{cases} \varphi=1 \text{ at } \omega=1 \\ \dfrac{d\varphi}{d\omega}=0 \text{ at } \omega=0 \end{cases} \qquad 5\text{-}19$$

With the estimated kinetic parameters (see Table 5-3), we could solve 5-18 numerically at t = 0 using the largest particle size of SPP (R_p = 200 nm). The effectiveness factor could then be calculated based on the concentration profile we obtained from 5-18.

$$\eta_A(t) \sim \eta_A(t=0) = \frac{3}{R_P} \frac{\left(D_A^e \frac{C_{AS}}{R_P} \right) \frac{d\varphi}{d\omega} |_{\omega=1}}{f\left(C_{AS}\right)} \qquad 5\text{-}20$$

For effective diffusivity around 6 x 10^{-15} m^2/s, we obtained effectiveness factor η_A ~ 0.9999. In a typical SPP structure, the mesopore volume fraction ε_p is assumed to be 0.4 based on the mesopore volume determined by Ar adsorption isotherm. Assuming tortuosity τ ~ 1, the minimum requirement of the benzyl alcohol diffusivity in mesitylene (D_A) is 1.5 x 10^{-14} m^2/s to assure that mesopore diffusion resistance does not affect the reaction rates (η_A ~ 1). The diffusivity of benzyl alcohol in toluene is reported to be around 3 x 10^{-9} m^2/s (Chiu *et al.*, 2004), which is larger by 5 orders of magnitudes. Therefore, our assumption that the effect of mesopore resistance on the measured alkylation and etherification reaction rates can be neglected in SPP zeolites is valid.

5.5.3 Alkylation and etherification reaction in presence of dTBP

One dTBP can irreversibly adsorb to one Brønsted acid site (Góra-Marek, Tarach and Choi, 2014). Given its large size (kinetic diameter ~ 7.9Å), dTBP could be used to selectively poison the external Brønsted acid sites of SPP (micropore diameter ~ 5.5Å). In theory, the reduction of the external Brønsted acid sites should lead to an equal portion of reduction in alkylation rate. To validate this assumption, experiments of alkylation and etherification were carried out in the presence of different amounts of dTBP. According

to the experimental data, the alkylation rate dropped by 80%, when the amount of dTBP was close to 20% of the external Brønsted acid site number, and it was fully suppressed when the amount of dTBP was increased up to 50% of the external Brønsted acid site number (see Figure 5-14). Therefore, the dTBP poisoning did not follow the expected stoichiometric ratio. It is likely that the adsorbed dTBP on the external Brønsted acid site also impeded the accessibility of its nearby Brønsted acid sites. When dTBP was used to selectively poison the external Brønsted acid sites, the etherification rate constant for the reaction inside MFI micropores might be underestimated due to the inaccessibility of the Brønsted acid sites near the adsorbed bulky dTBP molecules.

As discussed in section 5.3.2, the etherification reaction rates measured in the experiments include the contributions from both external and internal Brønsted acid sites. The reaction kinetics are different because of the adsorption and confinement effect in micropores. Therefore, the overall etherification rate change did not have a direct correlation with the change in Brønsted acid site numbers.

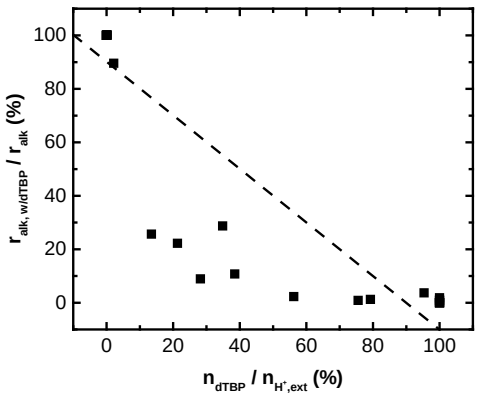

Figure 5-14 The fractions of the remaining alkylation rate after dTBP poisoning as a function of the fractions of poisoned proton sites on the external surface.

Chapter 6 Future work and concluding remarks

Although the concept of hierarchically organizing the porosity has been employed at an industrial level since 1980s, applications of hierarchical zeolites are still far from mature (Bellussi, Carati and Millini, 2010). Significant room remains for further developments.

In this dissertation, a specific example of hierarchical zeolites, SPP zeolite, was studied. A highly flexible structure was achieved through one-step direct synthesis by controlling synthetic conditions and compositions. Specifically, the diffusion lengths of microporous domains (i.e., half of the layer thickness in SPP zeolites) could be adjusted by controlling the hydrothermal temperature or using a secondary SDA, while the diffusion length of particles (i.e., particle size) and mesopore size distributions could be changed by tuning the water and ethanol ratio before hydrothermal step.

The structure—activity relationship based on such a model hierarchical zeolite was further explored. Using two liquid-phase model reactions in the presence of bulky reactants and products, the key structural attribute to selectivity was determined to be the diffusion length of microporous domains. When the target reaction is self-etherification, which includes molecules that could enter 10MR micropores, an optimum of layer thickness was found at the balance of the accessible active site density and the effectiveness of reactions in micropores. When the desired reaction is a surface reaction in the presence of bulky reactants or products (i.e., alkylation or de-etherification), both accessible active site density (which is inversely proportional to the layer thickness in SPP zeolites) and surface topology are important in terms of the selectivity and

productivity. The model reactions are also proved not to be diffusion controlled in SPP zeolites when the layer thickness is less than 6 nm.

Future research efforts regarding SPP zeolites could be put in the following directions:

- Functionalization of SPP zeolites

SPP zeolites have 6 times more surface silanol groups than MWW (Liu *et al.*, 2014). High density of surface silanol group makes SPP zeolites more hydrophilic and also hydrothermally less stabled compared to zeolites with less surface silanol group. However, the rich surface silanol group also provides more opportunities for functionalization with various organosilanes. Therefore, further research could be directed to the functionalization of SPP zeolites in the hope of improving the stability by reducing silanol groups as well as introducing new properties for potential applications.

- Applications in chemical and fine chemical productions

Most catalysts applied in industrial process (such as catalytic cracking, hydrocracking, *etc*.) are synthesized without using any template. The high cost of SDAs (even for the commercialized SDAs with simple structures) is still a large hindrance for the practical applications of the hierarchical zeolites that are synthesized through “bottom-up” or “constructive” methods. However, hierarchical zeolites synthesized with templates often show well-defined mesopore structures, which could be beneficial considering the connectivity and the acidity on the mesopore surface. Therefore, further research with respect to industrial applications of SPP zeolites could be focused on chemical, fine

chemicals and biomass transformation (Martínez and Corma, 2011; Perego *et al.*, 2017), where products have high-added values.

- Active sites distribution

In SPP zeolites, aluminum is assumed to be randomly distributed in the framework as discussed in section 5.3.1. Therefore, the external Brønsted acid site fraction is directly related to the layer thickness. When benzyl ether is the desired product, a completely selective catalyst would be possible if the aluminum sites could be deliberately placed in the micropores only. An inactive external mesopore surface could suppress all side-reactions over mesopore surface (e.g. alkylation) while still having the reduced diffusion resistance in micropores. One promising strategy that could significantly reduce external surface activity is to introduce aluminum through the defects that created from pure silica SPP framework using post-treatments. Further studies could be carried out in this direction to understand the stability, incorporation efficiency and acidity of the aluminum sites.

Furthermore, SPP zeolites are more stable compared to other amorphous mesoporous materials (such as SBA-15, MCM-41, *etc*.) due to the presence of crystalline framework. Therefore, except for directly incorporating heterogeneous atoms into the framework, the pillared structure of SPP with nanosheets down to one unit cell thick could also serves as a stable scaffold for a better dispersion of active sites.

It is our sincere hope that the studies in this dissertation would provide some fundamental insights into the catalytic behavior of SPP zeolites and other hierarchical zeolites with

similar structures. More practical applications could be found with the benefit of the highly flexible structure in SPP zeolites.

Bibliography

Abate, S. *et al.* (2016) 'Disruptive catalysis by zeolites', *Catalysis Science & Technology*. Royal Society of Chemistry, 6, pp. 2485–2501. doi: 10.1039/C5CY02184G.

Abdelrahman, O. A. *et al.* (2017) 'Simple quantification of zeolite acid site density by reactive gas chromatography', *Catalysis Science & Technology*. Royal Society of Chemistry, 7(17), pp. 3831–3841. doi: 10.1039/C7CY01068K.

Awala, H. *et al.* (2015) 'Template-free nanosized faujasite-type zeolites', *Nature Materials*, 14(4), pp. 447–451. doi: 10.1038/nmat4173.

Ban, T., Oishi, S. and Ohya, Y. (2014) 'Influence of Si species on intergrowth and anisotropic crystal growth of silicalite-1', *Journal of Porous Materials*, 21(3), pp. 337–344. doi: 10.1007/s10934-013-9779-y.

Bellussi, G., Carati, A. and Millini, R. (2010) 'Industrial Potential of Zeolites', in Cejka, J., Corma, A., and Zones, S. (eds) *Zeolites and Catalysis*. Weinheim, Germany: Wiley-VCH Verlag GmbH & Co. KGaA, pp. 449–491. doi: 10.1002/9783527630295.ch16.

Bergmann, A., Fritz, G. and Glatter, O. (2000) 'Solving the generalized indirect Fourier transformation (GIFT) by Boltzmann simplex simulated annealing (BSSA)', *Journal of Applied Crystallography*. International Union of Crystallography, 33(5), pp. 1212–1216. doi: 10.1107/S0021889800008372.

Burton, A. W. *et al.* (2010) 'Preparation and characterization of SSZ-54: A family of MTT/TON intergrowth materials', *Microporous and Mesoporous Materials*. Elsevier Inc., 132(1–2), pp. 54–59. doi: 10.1016/j.micromeso.2009.10.023.

Čejka, J. *et al.* (2012) 'Zeolite-based materials for novel catalytic applications: Opportunities, perspectives and open problems', *Catalysis Today*, 179(1), pp. 2–15. doi: 10.1016/j.cattod.2011.10.006.

Chaikittisilp, W. *et al.* (2013) 'Formation of Hierarchically Organized Zeolites by Sequential Intergrowth', *Angewandte Chemie International Edition*. WILEY-VCH Verlag, 52(12), pp. 3355–3359. doi: 10.1002/anie.201209638.

Chal, R. *et al.* (2011) 'Overview and Industrial Assessment of Synthesis Strategies towards Zeolites with Mesopores', *ChemCatChem*, 3(1), pp. 67–81. doi: 10.1002/cctc.201000158.

Chen, H. *et al.* (2011) 'Hydrothermal Synthesis of Zeolites with Three-Dimensionally Ordered Mesoporous-Imprinted Structure', *Journal of the American Chemical Society*, 133(32), pp. 12390–12393. doi: 10.1021/ja2046815.

Chen, L. H. *et al.* (2012) 'Hierarchically structured zeolites: synthesis, mass transport properties and applications', *Journal of Materials Chemistry*, 22(34), pp. 17381–17403.

Chiu, J. J. *et al.* (2004) 'Friedel–Crafts alkylation properties of aluminosilica SBA-15 meso/macroporous monoliths and mesoporous powders', *Journal of Catalysis*, 221(2), pp. 400–412. doi: 10.1016/j.jcat.2003.09.005.

Choi, M. *et al.* (2006) 'Amphiphilic organosilane-directed synthesis of crystalline zeolite with tunable mesoporosity', *Nature Materials*, 5(9), pp. 718–723. doi: 10.1038/nmat1705.

Choi, M. *et al.* (2009) 'Stable single-unit-cell nanosheets of zeolite MFI as active and

long-lived catalysts', *Nature*, 461(7261), pp. 246–249. doi: 10.1038/nature08288.

Christensen, C. H. *et al.* (2003) 'Catalytic Benzene Alkylation over Mesoporous Zeolite Single Crystals: Improving Activity and Selectivity with a New Family of Porous Materials', *Journal of the American Chemical Society*, 125(44), pp. 13370–13371. doi: 10.1021/ja037063c.

Chu, N., Yang, J., *et al.* (2010) 'A feasible way to enhance effectively the catalytic performance of methane dehydroaromatization', *Catalysis Communications*. Elsevier B.V., 11(6), pp. 513–517. doi: 10.1016/j.catcom.2009.12.004.

Chu, N., Wang, J., *et al.* (2010) 'Nestlike Hollow Hierarchical MCM-22 Microspheres: Synthesis and Exceptional Catalytic Properties', *Chemistry of Materials*, 22(9), pp. 2757–2763. doi: 10.1021/cm903645p.

Corma, A. (1997) 'From Microporous to Mesoporous Molecular Sieve Materials and Their Use in Catalysis', *Chemical Reviews*, 97(6), pp. 2373–2420. doi: 10.1021/cr960406n.

Corma, A., Fornés, V., *et al.* (1998) '2,6-Di-Tert-Butyl-Pyridine as a Probe Molecule to Measure External Acidity of Zeolites', *Journal of Catalysis*, 179(2), pp. 451–458. doi: 10.1006/jcat.1998.2233.

Corma, A., Fornes, V., *et al.* (1998) 'Delaminated zeolite precursors as selective acidic catalysts', *Nature*. Macmillan Magazines Ltd., 396(6709), pp. 353–356. doi: 10.1038/24592.

Corma, A. *et al.* (2006) 'High-throughput synthesis and catalytic properties of a

molecular sieve with 18- and 10-member rings', *Nature*, 443(7113), pp. 842–845. doi: 10.1038/nature05238.

Corma, A., Martínez-Soria, V. and Schnoeveld, E. (2000) 'Alkylation of Benzene with Short-Chain Olefins over MCM-22 Zeolite: Catalytic Behaviour and Kinetic Mechanism', *Journal of Catalysis*. Academic Press, 192(1), pp. 163–173. doi: 10.1006/jcat.2000.2849.

Davis, M. E. (2002) 'Ordered porous materials for emerging applications', *Nature*, 417(6891), pp. 813–821. doi: 10.1038/nature00785.

Davis, M. E. and Lobo, R. F. (1992) 'Zeolite and Molecular Sieve Synthesis', *Chemistry of Materials*, 4(4), pp. 756–768. doi: 10.1021/cm00022a005.

Davis, T. M. *et al.* (2006) 'Mechanistic principles of nanoparticle evolution to zeolite crystals', *Nature Materials*, 5(5), pp. 400–408. doi: 10.1038/nmat1636.

Emeis, C. A. (1993) 'Determination of Integrated Molar Extinction Coefficients for Infrared Absorption Bands of Pyridine Adsorbed on Solid Acid Catalysts', *Journal of Catalysis*, 141(2), pp. 347–354. doi: 10.1006/jcat.1993.1145.

Ennaert, T. *et al.* (2016) 'The importance of pretreatment and feedstock purity in the reductive splitting of (ligno)cellulose by metal supported USY zeolite', *Green Chemistry*. Royal Society of Chemistry, 18(7), pp. 2095–2105. doi: 10.1039/C5GC02346G.

Fan, W. *et al.* (2008) 'Hierarchical nanofabrication of microporous crystals with ordered mesoporosity', *Nature Materials*, 7(12), pp. 984–991. doi: 10.1038/nmat2302.

Feng, H. *et al.* (2010) 'Solid-state transformation of hollow silica microspheres into

hierarchical ZSM-5 having tunable mesopores', *Catalysis Communications*. Elsevier B.V., 11(8), pp. 700–704. doi: 10.1016/j.catcom.2010.01.024.

Francesconi, M. S. *et al.* (2005) 'MFI/MEL intergrowth and its effect on n-decane cracking', *Catalysis Today*, 107–108, pp. 809–815. doi: 10.1016/j.cattod.2005.07.013.

Gamliel, D. P. *et al.* (2018) 'Nickel impregnated mesoporous USY zeolites for hydrodeoxygenation of anisole', *Microporous and Mesoporous Materials*. Elsevier, 261(August 2017), pp. 18–28. doi: 10.1016/j.micromeso.2017.10.027.

Garcia-Martinez, J. *et al.* (2014) 'Evidence of Intracrystalline Mesostructured Porosity in Zeolites by Advanced Gas Sorption, Electron Tomography and Rotation Electron Diffraction', *ChemCatChem*. WILEY-VCH Verlag, 6(11), pp. 3110–3115. doi: 10.1002/cctc.201402499.

García-Martínez, J. *et al.* (2012) 'Mesostructured zeolite Y—high hydrothermal stability and superior FCC catalytic performance', *Catalysis Science & Technology*, 2(5), p. 987. doi: 10.1039/c2cy00309k.

González, G. *et al.* (2007) 'New zeolite topologies based on intergrowths of FAU/EMT systems', *Microporous and Mesoporous Materials*, 101(1–2 SPEC. ISS.), pp. 30–42. doi: 10.1016/j.micromeso.2006.11.008.

Góra-Marek, K., Tarach, K. and Choi, M. (2014) '2,6-Di-tert-butylpyridine Sorption Approach to Quantify the External Acidity in Hierarchical Zeolites', *The Journal of Physical Chemistry C*. American Chemical Society, 118(23), pp. 12266–12274. doi: 10.1021/jp501928k.

Grand, J. *et al.* (2017) 'One-pot synthesis of silanol-free nanosized MFI zeolite', *Nature Materials*, 16(10), pp. 1010–1015. doi: 10.1038/nmat4941.

Guo, D. *et al.* (2015) 'USY zeolites with tunable mesoporosity designed by controlling framework Fe content and their catalytic cracking properties', *Microporous and Mesoporous Materials*. Elsevier Ltd, 211, pp. 192–199. doi: 10.1016/j.micromeso.2015.02.004.

Harris, J. W. *et al.* (2016) 'Titration and quantification of open and closed Lewis acid sites in Sn-Beta zeolites that catalyze glucose isomerization', *Journal of Catalysis*. Elsevier Inc., 335, pp. 141–154. doi: 10.1016/j.jcat.2015.12.024.

Hartmann, M., Machoke, A. G. and Schwieger, W. (2016) 'Catalytic test reactions for the evaluation of hierarchical zeolites', *Chemical Society Reviews*. Royal Society of Chemistry, 45(12), pp. 3313–3330. doi: 10.1039/C5CS00935A.

Hay, D. G., Jaeger, H. and Wilshier, K. G. (1990) 'Systematic intergrowth in crystals of ZSM-5 zeolite', *Zeolites*, 10(6), pp. 571–576. doi: 10.1016/S0144-2449(05)80314-8.

Hemmann, F. *et al.* (2015) 'Quantification of acidic sites of nanoscopic hydroxylated magnesium fluorides by FTIR and 15N MAS NMR spectroscopy', *RSC Advances*, 5(109), pp. 89659–89668. doi: 10.1039/c5ra15116c.

Holm, M. S. *et al.* (2011) 'Catalysis with hierarchical zeolites', *Catalysis Today*, 168(1), pp. 3–16. doi: 10.1016/j.cattod.2011.01.007.

Hu, S. *et al.* (2012) 'Selective formation of propylene from methanol over high-silica nanosheets of MFI zeolite', *Applied Catalysis A: General*, 445–446, pp. 215–220. doi:

10.1016/j.apcata.2012.08.032.

Inayat, A. *et al.* (2012) ‘Assemblies of Mesoporous FAU-Type Zeolite Nanosheets’, *Angewandte Chemie International Edition*. WILEY-VCH Verlag, 51(8), pp. 1962–1965. doi: 10.1002/anie.201105738.

Jablonski, G. A., Sand, L. B. and Gard, J. A. (1986) ‘Synthesis and identification of ZSM-5 ZSM-11 pentasil intergrowth structures’, *Zeolites*, 6(5), pp. 396–402. doi: 10.1016/0144-2449(86)90069-2.

Jacobs, P. A., Dusselier, M. and Sels, B. F. (2014) ‘Will zeolite-based catalysis be as relevant in future biorefineries as in crude oil refineries?’, *Angewandte Chemie - International Edition*, 53(33), pp. 8621–8626. doi: 10.1002/anie.201400922.

Jeong, H. K. *et al.* (2002) ‘Oriented molecular sieve membranes by heteroepitaxial growth’, *Journal of the American Chemical Society*, 124(44), pp. 12966–12968. doi: 10.1021/ja020947w.

Karwacki, L. *et al.* (2009) ‘Morphology-dependent zeolite intergrowth structures leading to distinct internal and outer-surface molecular diffusion barriers’, *Nature Materials*. Nature Publishing Group, 8(12), pp. 959–965. doi: 10.1038/nmat2530.

Keller, T. C. *et al.* (2015) ‘Design of hierarchical zeolite catalysts for the manufacture of polyurethane intermediates’, *ACS Catalysis*, 5(2), pp. 734–743. doi: 10.1021/cs5017694.

Khaleel, M. *et al.* (2016) ‘Combining Pre- and Post-Nucleation Trajectories for the Synthesis of High FAU-Content Faujasite Nanocrystals from Organic-Free Sols’, *Chemistry of Materials*, 28(12), pp. 4204–4213. doi: 10.1021/acs.chemmater.6b00588.

Kim, J., Choi, M. and Ryoo, R. (2010) ‘Effect of mesoporosity against the deactivation of MFI zeolite catalyst during the methanol-to-hydrocarbon conversion process’, *Journal of Catalysis*. Elsevier Inc., 269(1), pp. 219–228. doi: 10.1016/j.jcat.2009.11.009.

Kim, J., Park, W. and Ryoo, R. (2011) ‘Surfactant-Directed Zeolite Nanosheets: A High-Performance Catalyst for Gas-Phase Beckmann Rearrangement’, *ACS Catalysis*. American Chemical Society, 1(4), pp. 337–341. doi: 10.1021/cs100160g.

Koekkoek, A. J. J. *et al.* (2013) ‘Catalytic performance of sheet-like Fe/ZSM-5 zeolites for the selective oxidation of benzene with nitrous oxide’, *Journal of Catalysis*, 299, pp. 81–89. doi: 10.1016/j.jcat.2012.12.002.

Konno, H. *et al.* (2014) ‘Kinetics of the catalytic cracking of naphtha over ZSM-5 zeolite: effect of reduced crystal size on the reaction of naphthenes’, *Catal. Sci. Technol.* Royal Society of Chemistry, 4(12), pp. 4265–4273. doi: 10.1039/C4CY00733F.

Kumar, S. *et al.* (2008) ‘A Structural Resolution Cryo-TEM Study of the Early Stages of MFI Growth’, *Journal of the American Chemical Society*. American Chemical Society, 130(51), pp. 17284–17286. doi: 10.1021/ja8063167.

Lee, P.-S. *et al.* (2011) ‘Sub-40 nm Zeolite Suspensions via Disassembly of Three-Dimensionally Ordered Mesoporous-Imprinted Silicalite-1’, *Journal of the American Chemical Society*, 133(3), pp. 493–502. doi: 10.1021/ja107942n.

Leng, K. *et al.* (2013) ‘Enhancement of catalytic performance in the benzylation of benzene with benzyl alcohol over hierarchical mordenite’, *Journal of Catalysis*. Elsevier Inc., 306, pp. 100–108. doi: 10.1016/j.jcat.2013.06.004.

Leonowicz, M. E. *et al.* (1994) 'MCM-22: A Molecular Sieve with Two Independent Multidimensional Channel Systems', *Science*, 264(5167), pp. 1910–1913. doi: 10.1126/science.264.5167.1910.

Li, J., Corma, A. and Yu, J. (2015) 'Synthesis of new zeolite structures', *Chemical Society Reviews*. Royal Society of Chemistry, 44(20), pp. 7112–7127. doi: 10.1039/C5CS00023H.

Li, K., Valla, J. and Garcia-Martinez, J. (2014a) 'Realizing the commercial potential of hierarchical zeolites: New opportunities in catalytic cracking', *ChemCatChem*, pp. 46–66. doi: 10.1002/cctc.201300345.

Li, K., Valla, J. and Garcia-Martinez, J. (2014b) 'Realizing the Commercial Potential of Hierarchical Zeolites: New Opportunities in Catalytic Cracking', *ChemCatChem*, 6(1), pp. 46–66. doi: 10.1002/cctc.201300345.

Li, X. F., Prins, R. and van Bokhoven, J. A. (2009) 'Synthesis and characterization of mesoporous mordenite', *Journal of Catalysis*. Elsevier Inc., 262(2), pp. 257–265. doi: 10.1016/j.jcat.2009.01.001.

Li, Z. *et al.* (2005) 'Pure-silica-zeolite MEL low-k films from nanoparticle suspensions', *Journal of Physical Chemistry B*, 109(18), pp. 8652–8658. doi: 10.1021/jp0441893.

Liang, D. *et al.* (2007) 'TEM Observation of Aggregation Steps in Room-Temperature Silicalite-1 Zeolite Formation', *The Journal of Physical Chemistry C*, 111(39), pp. 14283–14285. doi: 10.1021/jp074960k.

Lillerud, K. P. and Raeder, J. H. (1986) 'On the synthesis of erionite—offretite

intergrowth zeolites', *Zeolites*, 6(6), pp. 474–483. doi: 10.1016/0144-2449(86)90032-1.

Liu, D. *et al.* (2011) 'Catalytic behavior of Brønsted acid sites in MWW and MFI zeolites with dual meso- and microporosity', *ACS Catalysis*. American Chemical Society, 1(1), pp. 7–17. doi: 10.1021/cs100042r.

Liu, D. *et al.* (2014) 'Activity and selectivity differences of external Brønsted acid sites of single-unit-cell thick and conventional MFI and MWW zeolites', *Microporous and Mesoporous Materials*, 200(0), pp. 287–290. doi: 10.1016/j.micromeso.2014.06.029.

Lopez-Orozco, S. *et al.* (2011) 'Zeolitic materials with hierarchical porous structures', *Advanced Materials*. WILEY-VCH Verlag, 23(22–23), pp. 2602–2615. doi: 10.1002/adma.201100462.

Maheshwari, S. *et al.* (2008) 'Layer Structure Preservation during Swelling, Pillaring, and Exfoliation of a Zeolite Precursor', *Journal of the American Chemical Society*. American Chemical Society, 130(4), pp. 1507–1516. doi: 10.1021/ja077711i.

Martínez, C. and Corma, A. (2011) 'Inorganic molecular sieves: Preparation, modification and industrial application in catalytic processes', *Coordination Chemistry Reviews*, 255(13–14), pp. 1558–1580. doi: 10.1016/j.ccr.2011.03.014.

MEI, C. *et al.* (2008) 'Selective production of propylene from methanol: Mesoporosity development in high silica HZSM-5', *Journal of Catalysis*, 258(1), pp. 243–249. doi: 10.1016/j.jcat.2008.06.019.

Milina, M. *et al.* (2014) 'Mesopore quality determines the lifetime of hierarchically structured zeolite catalysts', *Nature Communications*, 5(1), p. 3922. doi:

10.1038/ncomms4922.

Millward, G. R., Ramdas, S. and Thomas, J. M. (1985) ‘On the Direct Imaging of Offretite, Cancrinite, Chabazite and other Related ABC-6 Zeolites and their Intergrowths’, *Proceedings of the Royal Society A: Mathematical, Physical and Engineering Sciences*, 399(1816), pp. 57–71. doi: 10.1098/rspa.1985.0047.

Mintova, S. *et al.* (1999) ‘Mechanism of Zeolite A Nanocrystal Growth from Colloids at Room Temperature’, *Science*, 283(5404), pp. 958–960. doi: 10.1126/science.283.5404.958.

Moliner, M., Martínez, C. and Corma, A. (2015) ‘Multipore zeolites: Synthesis and catalytic applications’, *Angewandte Chemie - International Edition*, 54(12), pp. 3560–3579. doi: 10.1002/anie.201406344.

Moller, K. and Bein, T. (2013) ‘Mesoporosity - a new dimension for zeolites’, *Chemical Society Reviews*. The Royal Society of Chemistry, 42(9), pp. 3689–3707. doi: 10.1039/c3cs35488a.

Morterra, C., Magnacca, G. and Bolis, V. (2001) ‘On the critical use of molar absorption coefficients for adsorbed species: the methanol/silica system’, *Catalysis Today*, 70(1–3), pp. 43–58. doi: 10.1016/S0920-5861(01)00406-0.

Na, K. *et al.* (2011) ‘Directing Zeolite Structures into Hierarchically Nanoporous Architectures’, *Science*, 333(6040), pp. 328–332.

Narender, N. *et al.* (2006) ‘Liquid phase benzylation of benzene and toluene with benzyl alcohol over modified zeolites’, *Catalysis Communications*, 7(8), pp. 583–588. doi:

10.1016/j.catcom.2006.01.013.

Nesterenko, N. S. *et al.* (2006) 'The use of the consecutive adsorption of pyridine bases and carbon monoxide in the IR spectroscopic study of the accessibility of acid sites in microporous/mesoporous materials', *Kinetics and Catalysis*. Nauka/Interperiodica, 47(1), pp. 40–48. doi: 10.1134/S0023158406010071.

Ngoye, F. *et al.* (2014) 'Mitigating coking during methylcyclohexane transformation on HZSM-5 zeolites with additional porosity', *Journal of Catalysis*. Elsevier Inc., 320(1), pp. 118–126. doi: 10.1016/j.jcat.2014.10.001.

Ogura, M. *et al.* (2001) 'Alkali-treatment technique — new method for modification of structural and acid-catalytic properties of ZSM-5 zeolites', *Applied Catalysis A: General*, 219(1–2), pp. 33–43. doi: 10.1016/S0926-860X(01)00645-7.

Ohsuna, T. *et al.* (1997) 'Electron microscopic study of intergrowth of MFL and MEL: Crystal faults B-MEL', *Journal of Physical Chemistry B*, 101(48), pp. 9881–9885. doi: 10.1021/jp971448y.

Okubo, T. *et al.* (2001) 'Heteroepitaxial growth of a zeolite', *Angewandte Chemie - International Edition*. WILEY-VCH Verlag GmbH, 40(6), pp. 1069–1071. doi: 10.1002/1521-3773(20010316)40:6<1069::AID-ANIE10690>3.0.CO;2-W.

Olson, D. and Bisio, A. (1984) 'Proceedings of the Sixth International Zeolite Conference : Reno, USA 10-15 July 1983', in Olson, D. and Bisio, A. (eds). Guildford, Surrey, UK: Butterworths, p. x,1007p.

Parlett, C. M. a, Wilson, K. and Lee, A. F. (2013) 'Hierarchical porous materials:

catalytic applications.', *Chemical Society reviews*, 42(9), pp. 3876–93. doi: 10.1039/c2cs35378d.

Perego, C. *et al.* (2017) 'Zeolite Materials for Biomass Conversion to Biofuel', *Energy & Fuels*, 31(8), pp. 7721–7733. doi: 10.1021/acs.energyfuels.7b01057.

Perego, C. and Ingallina, P. (2002) 'Recent advances in the industrial alkylation of aromatics: new catalysts and new processes', *Catalysis Today*, 73(1–2), pp. 3–22. doi: 10.1016/S0920-5861(01)00511-9.

Perego, C. and Millini, R. (2013) 'Porous materials in catalysis: challenges for mesoporous materials.', *Chemical Society reviews*, 42(9), pp. 3956–76. doi: 10.1039/c2cs35244c.

Perez-Ramirez, J. *et al.* (2009) 'Zeolite Catalysts with Tunable Hierarchy Factor by Pore-Growth Moderators', *Advanced Functional Materials*, 19(24), pp. 3972–3979. doi: 10.1002/adfm.200901394.

Pérez-Ramírez, J. *et al.* (2008) 'Hierarchical zeolites: enhanced utilisation of microporous crystals in catalysis by advances in materials design', *Chemical Society Reviews*, 37(11), p. 2530. doi: 10.1039/b809030k.

Pérez-Ramírez, J. *et al.* (2011) 'Expanding the Horizons of Hierarchical Zeolites: Beyond Laboratory Curiosity towards Industrial Realization', *ChemCatChem*. WILEY-VCH Verlag, 3(11), pp. 1731–1734. doi: 10.1002/cctc.201100264.

Prasomsri, T. *et al.* (2015) 'Mesostructured zeolites: bridging the gap between zeolites and MCM-41', *Chemical Communications*. Royal Society of Chemistry, 51(43), pp.

8900–8911. doi: 10.1039/C4CC10391B.

Ramasamy, K. K. *et al.* (2014) ‘Conversion of ethanol to hydrocarbons on hierarchical HZSM-5 zeolites’, *Catalysis Today*. Elsevier B.V., 238, pp. 103–110. doi: 10.1016/j.cattod.2014.01.037.

Ravikovitch, P. I. and Neimark, A. V. (2001) ‘Characterization of nanoporous materials from adsorption and desorption isotherms’, *Colloids and Surfaces A: Physicochemical and Engineering Aspects*, 187–188, pp. 11–21. doi: 10.1016/S0927-7757(01)00614-8.

Ren, L. *et al.* (2015) ‘Self-Pillared, Single-Unit-Cell Sn-MFI Zeolite Nanosheets and Their Use for Glucose and Lactose Isomerization’, *Angewandte Chemie International Edition*, 54(37), pp. 10848–10851. doi: 10.1002/anie.201505334.

Revealed, I. *et al.* (2010) ‘Oriented aggregation: Formation and transformation of mesocrystal’, *Journal of the American Chemical Society*, 132(7), pp. 2163–2165. doi: 10.1021/ja909769a.

Roth, W. J. and Dorset, D. L. (2011) ‘Expanded view of zeolite structures and their variability based on layered nature of 3-D frameworks’, *Microporous and Mesoporous Materials*. Elsevier Inc., 142(1), pp. 32–36. doi: 10.1016/j.micromeso.2010.11.007.

Schwieger, W. *et al.* (2016) ‘Hierarchy concepts: classification and preparation strategies for zeolite containing materials with hierarchical porosity’, *Chemical Society Reviews*. Royal Society of Chemistry, 45(12), pp. 3353–3376. doi: 10.1039/C5CS00599J.

Selli, E. and Forni, L. (1999) ‘Comparison between the surface acidity of solid catalysts determined by TPD and FTIR analysis of pre-adsorbed pyridine’, *Microporous and*

Mesoporous Materials, 31(1–2), pp. 129–140. doi: http://dx.doi.org/10.1016/S1387-1811(99)00063-3.

Serrano, D. P. *et al.* (2011) 'Synthesis of hierarchical ZSM-5 by silanization and alkoxylation of protozeolitic units', *Catalysis Today*. Elsevier B.V., 168(1), pp. 86–95. doi: 10.1016/j.cattod.2010.12.040.

Shen, X. *et al.* (2018) 'A Hierarchical MFI Zeolite with a Two-Dimensional Square Mesostructure', *Angewandte Chemie International Edition*, 57(3), pp. 724–728. doi: 10.1002/anie.201710748.

Sholl, D. S. and Lively, R. P. (2015) 'Defects in Metal–Organic Frameworks: Challenge or Opportunity?', *The Journal of Physical Chemistry Letters*, 6(17), pp. 3437–3444. doi: 10.1021/acs.jpclett.5b01135.

Sławiński, W. A. *et al.* (2014) 'Intergrowth structure modelling in silicoaluminophosphate SAPO-18/34 family', *Microporous and Mesoporous Materials*, 195, pp. 311–318. doi: 10.1016/j.micromeso.2014.04.024.

Smeets, S. *et al.* (2014) 'High-Silica Zeolite SSZ-61 with Dumbbell-Shaped Extra-Large-Pore Channels', *Angewandte Chemie International Edition*, 53(39), pp. 10398–10402. doi: 10.1002/anie.201405658.

Smith, R. L. *et al.* (2015) 'Nanoporous Intergrowths: How Crystal Growth Dictates Phase Composition and Hierarchical Structure in the CHA/AEI System', *Chemistry of Materials*, 27(12), pp. 4205–4215. doi: 10.1021/cm504284x.

Stöcker, M. (2008) 'Biofuels and biomass-to-liquid fuels in the biorefinery: Catalytic

conversion of lignocellulosic biomass using porous materials', *Angewandte Chemie - International Edition*, 47(48), pp. 9200–9211. doi: 10.1002/anie.200801476.

Sun, J. *et al.* (2009) 'The ITQ-37 mesoporous chiral zeolite', *Nature*, 458(7242), pp. 1154–1157. doi: 10.1038/nature07957.

Sun, Q. *et al.* (2014) 'Organosilane surfactant-directed synthesis of hierarchical porous SAPO-34 catalysts with excellent MTO performance', *Chemical Communications*, 50(49), p. 6502. doi: 10.1039/c4cc02050b.

Sun, Y. and Prins, R. (2008) 'Friedel-Crafts alkylations over hierarchical zeolite catalysts', *Applied Catalysis A: General*, 336(1–2), pp. 11–16. doi: 10.1016/j.apcata.2007.08.015.

Swindlehurst, G. R. *et al.* (2015) 'Nucleation, Growth, and Robust Synthesis of SPP Zeolite: Effect of Ethanol, Sodium, and Potassium', *Topics in Catalysis*, 58(7–9), pp. 545–558. doi: 10.1007/s11244-015-0396-7.

Tao, Y. *et al.* (2005) 'Comparative Study on Pore Structures of Mesoporous ZSM-5 from Resorcinol-Formaldehyde Aerogel and Carbon Aerogel Templating', *The Journal of Physical Chemistry B*, 109(1), pp. 194–199. doi: 10.1021/jp0464167.

Thomas, J. M. *et al.* (2013) 'Some turning points in the chemical electron microscopic study of heterogeneous catalysts', *ChemCatChem*, 5(9), pp. 2560–2579. doi: 10.1002/cctc.201200883.

Tosheva, L. and Valtchev, V. P. (2005) 'Nanozeolites: Synthesis, crystallization mechanism, and applications', *Chemistry of Materials*, 17(10), pp. 2494–2513. doi:

10.1021/cm047908z.

Treacy, M. M. J. *et al.* (1996) ‘Intergrowth Segregation in FAU-EMT Zeolite Materials’, *Proceedings of the Royal Society A: Mathematical, Physical and Engineering Sciences*, 452(April), pp. 813–840. doi: 10.1098/rspa.1996.0041.

Tsapatsis, M. (2014) ‘2-dimensional zeolites’, *Aiche Journal*, p. n/a-n/a. doi: 10.1002/aic.14462.

Valtchev, V. *et al.* (2013) ‘Tailored crystalline microporous materials by post-synthesis modification.’, *Chemical Society reviews*. The Royal Society of Chemistry, 42(1), pp. 263–90. doi: 10.1039/c2cs35196j.

Valtchev, V. and Tosheva, L. (2013) ‘Porous nanosized particles: Preparation, properties, and applications’, *Chemical Reviews*, 113(8), pp. 6734–6760. doi: 10.1021/cr300439k.

Vernimmen, J., Meynen, V. and Cool, P. (2011) ‘Synthesis and catalytic applications of combined zeolitic/mesoporous materials’, *Beilstein Journal of Nanotechnology*, 2, pp. 785–801. doi: 10.3762/bjnano.2.87.

Wang, J. *et al.* (2007) ‘Single-template synthesis of zeolite ZSM-5 composites with tunable mesoporosity’, *Chemical Communications*. The Royal Society of Chemistry, (44), p. 4653. doi: 10.1039/b708822a.

Wang, J. *et al.* (2009) ‘TUD-C: A tunable, hierarchically structured mesoporous zeolite composite’, *Microporous and Mesoporous Materials*. Elsevier Inc., 120(1–2), pp. 19–28. doi: 10.1016/j.micromeso.2008.08.060.

Wang, L. *et al.* (2017) ‘Fractal MTW Zeolite Crystals: Hidden Dimensions in

Nanoporous Materials', *Angewandte Chemie International Edition*, 201704499, pp. 11764–11768. doi: 10.1002/anie.201704499.

Wang, Q. *et al.* (2014) 'Synthesis of mesoporous ZSM-5 catalysts using different mesogenous templates and their application in methanol conversion for enhanced catalyst lifespan', *RSC Advances*, 4(41), pp. 21479–21491. doi: 10.1039/c4ra02695k.

Wang, Y. *et al.* (2015) 'Effect of post treatment on the local structure of hierarchical Beta prepared by desilication and the catalytic performance in Friedel–Crafts alkylation', *Microporous and Mesoporous Materials*. Elsevier Inc., 206(C), pp. 42–51. doi: 10.1016/j.micromeso.2014.12.017.

Wang, Y. X. *et al.* (2005) 'Synthesis and Crystal Structure of Zeolite RUB-41 Obtained as Calcination Product of a Layered Precursor: a Systematic Approach to a New Synthesis Route', *Chemistry of Materials*, 17(1), pp. 43–49. doi: 10.1021/cm048677z.

Wang, Z., Yu, J. and Xu, R. (2012) 'Needs and trends in rational synthesis of zeolitic materials', *Chemical Society Reviews*. The Royal Society of Chemistry, 41(5), pp. 1729–1741. doi: 10.1039/c1cs15150a.

Willhammar, T. *et al.* (2012) 'Structure and catalytic properties of the most complex intergrown zeolite ITQ-39 determined by electron crystallography', *Nature Chemistry*, 4(3), pp. 188–194. doi: 10.1038/nchem.1253.

Wu, Y. *et al.* (2016) 'Quantification of external surface and pore mouth acid sites in unit-cell thick pillared MFI and pillared MWW zeolites', *Microporous and Mesoporous Materials*. Elsevier Ltd, 241, pp. 43–51. doi: 10.1016/j.micromeso.2016.12.004.

Xu, D. *et al.* (2014) ‘On the synthesis and adsorption properties of single-unit-cell hierarchical zeolites made by rotational intergrowths’, *Advanced Functional Materials*, 24(2), pp. 201–208. doi: 10.1002/adfm.201301975.

Yao, J., Huang, Y. and Wang, H. (2010) ‘Controlling zeolite structures and morphologies using polymer networks’, *Journal of Materials Chemistry*, 20(44), p. 9827. doi: 10.1039/c0jm01003k.

Yin, C. *et al.* (2015) ‘Synthesis of hierarchical porous silicalite-1 and its catalytic performance in Beckmann rearrangement’, *Microporous and Mesoporous Materials*. Elsevier Inc., 202(C), pp. 133–137. doi: 10.1016/j.micromeso.2014.08.047.

York, R. L. *et al.* (2011) ‘Dead zones in porous catalysts: Concentration profiles and efficiency factors’, *Catalysis Today*, 160(1), pp. 204–212. doi: 10.1016/j.cattod.2010.06.022.

Zhang, L. *et al.* (2012) ‘Organic template-free synthesis of ZSM-5/ZSM-11 co-crystalline zeolite’, *Microporous and Mesoporous Materials*. Elsevier Inc., 147(1), pp. 117–126. doi: 10.1016/j.micromeso.2011.05.033.

Zhang, L. *et al.* (2015) ‘F-assisted synthesis of a hierarchical ZSM-5 zeolite for methanol to propylene reaction: a b-oriented thinner dimensional morphology’, *RSC Advances*. Royal Society of Chemistry, 5(75), pp. 61354–61363. doi: 10.1039/C5RA09561A.

Zhang, X. *et al.* (2012) ‘Synthesis of Self-Pillared Zeolite Nanosheets by Repetitive Branching’, *Science*, 336(6089), pp. 1684–1687. doi: 10.1126/science.1221111.

Zhao, D. *et al.* (2017a) ‘Synthesis of AEI/CHA intergrowth zeolites by dual templates

and their catalytic performance for dimethyl ether to olefins', *Chemical Engineering Journal*. Elsevier B.V., 323, pp. 295–303. doi: 10.1016/j.cej.2017.04.109.

Zhao, D. *et al.* (2017b) 'Synthesis of SAPO-18/34 intergrowth zeolites and their enhanced stability for dimethyl ether to olefins', *RSC Advances*. Royal Society of Chemistry, 7(2), pp. 939–946. doi: 10.1039/c6ra25080g.